Lifetime measurements of the 2_1^+ states in even-even platinum isotopes with $A = 180\text{-}186$

Rikako Kono

A thesis submitted for the degree of

Master of Philosophy

The Australian National University

Research School of Physics

31 October 2025

Disclaimer

This thesis presents the research undertaken from November 2023 to October 2025 in the Department of Nuclear Physics, Research School of Physics, College of Science and Medicine, Australian National University, Canberra, Australia.

To the best of my knowledge, and unless otherwise stated in the customary manner, the content of this thesis is my own original work, and has not been submitted in whole or in part for a degree at any university.

河野 理夏子

Rikako Kono
31 October 2025

Acknowledgements

Looking back, the two years of my MPhil feel brief in time yet rich in experience. They taught me far more than I ever expected, not only about physics but also about myself and the people who supported me along the way.

First and foremost, my deepest gratitude goes to my primary supervisor, Prof. Greg Lane, whose guidance, patience and countless discussions shaped both this thesis and my own growth. I have lost count of how many times I (and everyone else) tried to equip you with a GPS so we could find you more easily, but your enthusiasm and friendliness were always easy to locate. I do regret not visiting your house, especially since we have been neighbours all along.

I am also grateful to the rest of my supervisory panel, Prof. Andrew Stuchbery, Dr. AJ Mitchell and Dr. Kaitlin Cook. Andrew consistently found the bright side of every situation, which helped me move forward whenever I felt stuck. AJ somehow kept the entire Structure group running smoothly and noticed things long before the rest of us did. Kaitlin gave me precise and thoughtful advice every time, offering exactly the guidance I needed. I feel genuinely lucky to have had such a supportive and attentive panel watching over every corner of this project.

To all the technical staff, nothing would have been possible without you all keeping the accelerator running. In particular, I owe special thanks to Mr. Thomas Tunningley, who greatly helped with one of my projects on designing the passive shields.

I feel truly privileged to have studied in this laboratory. My sincere thanks also go to the ANU for the award of the scholarship that supported me throughout my studies.

To all NPAA students, thank you for sharing your time and company through countless small chats that made my lunch breaks longer and infinitely more enjoyable. Your stories were always entertaining, and thanks to you, my movie knowledge has probably doubled.

I would also like to thank my family, relatives, and friends. Even though most of you would roll your eyes the moment I started talking about physics, you still listened, sometimes laughing, sometimes puzzled, but always patient and supportive. And I am afraid you will have to keep putting up with me a little longer yet.

Finally, to everyone who has been part of my physics journey since 2019, from my undergraduate days to this very moment, thank you. This thesis marks the end of my life in physics, but the curiosity and insights you have instilled in me will stay with me as I move on to new adventures.

Abstract

The neutron-deficient even-mass platinum isotopes have long been of interest for their transitional shapes and the emergence of shape coexistence. The more neutron-rich $^{190-198}$Pt isotopes have weakly deformed, oblate structures in their ground states and show some evidence of triaxiality. In contrast, the lighter mid-shell isotopes $^{178-186}$Pt exhibit prolate ground states and clear evidence of shape coexistence, with ^{188}Pt as a transition point between two regions. These platinum isotopes present a notably complex evolution of shapes and shape coexistence that would benefit from further investigation.

The lifetimes of 2_1^+ states and the $B(E2; 2_1^+ \rightarrow 0_1^+)$ reduced transition strengths are valuable to give insight into the magnitude of the nuclear deformations and their shape. However, there are significant discrepancies in 2_1^+ lifetimes for the shape-coexistence region, $^{180-186}$Pt, from the Evaluated Nuclear Structure Data File (ENSDF) database and more recent measurements using methods such as the recoil distance method (RDM) and the Generalised Centroid Difference (GCD) method.

To address this puzzle, we performed direct-timing lifetime measurements of the 2_1^+ states in $^{180-186}$Pt using exponential-convoluted Gaussian fitting and GCD methods applied to γ-fast timing data taken with LaBr$_3$(Ce) detectors at the Australian Heavy Ion Accelerator Facility (HIAF) in August and September 2023. The 2_1^+ lifetimes obtained from both the convolution and GCD methods are in agreement, yielding results of 533(26) ps, 561(14) ps, 479(6) ps and 350(4) ps for $^{180-186}$Pt, respectively. The measurements for ^{180}Pt and ^{186}Pt in the present study are consistent with ENSDF, and those for ^{182}Pt align with a recent result. However, a discrepancy is observed between our measurement and the ENSDF data for ^{184}Pt, suggesting to revisit the lifetime measurement for this isotope.

Our experimental values were then compared to the results obtained from an empirical multi-band-mixing model to clarify the underlying shape assignments. The calculation considering shape coexistence reproduced the experimental $B(E2; 2_1^+ \rightarrow 0_1^+)$ values well, thereby further emphasising the presence of shape coexistence in these regions.

A new passive-shielding array for LaBr$_3$ detectors for future lifetime measurements has been designed, built and incorporated into the CAESAR gamma-ray detector array. The first test experiments with the new shields were performed in October 2025, and the results are currently being analysed.

Contents

List of Figures

List of Tables

Chapter 1

Introduction

Atomic nuclei consist of neutrons and protons, termed nucleons, forming a complex quantum-mechanical many-body system. Their identity and stability hinge on the number of protons (Z) and neutrons (N) they contain. This defines categories like isotopes, which have the same number of protons but differ in their number of neutrons. While their chemical properties are nearly identical, they exhibit different nuclear properties, such as shapes, energies and lifetimes. Understanding the structure and behaviour of nuclei is a central objective in nuclear physics.

This thesis examines neutron-deficient even-mass platinum isotopes, known for their unique and complex nuclear structures such as shape coexistence and a ground-state shape transition across isotopes. Shape coexistence is a nuclear shape phenomenon where different shapes exist in the same nuclei at similar excitation energies.

1.1 The neutron-deficient even-mass Pt isotopes

Platinum isotopes with $Z = 78$ are located between the oblate-shaped mercury ($Z = 80$) isotopes, which are two protons below the $Z = 82$ magic number, and the well-deformed prolate nuclei in the rare-earth region below $Z = 71$. Neutron-deficient even-mass platinum isotopes have long been studied for their transitional shapes and the emergence of shape coexistence (see Sec. 2.5). The $^{190-198}$Pt isotopes have weakly deformed, oblate structures for their ground states and show some evidence of triaxiality [1]. In contrast, starting from ^{188}Pt as a transitional point, the mid-shell isotopes $^{178-186}$Pt exhibit prolate ground states and clear evidence of shape coexistence [2].

These characteristics are apparent in the energy-level systematics of even-even platinum nuclei, as shown in Fig. 1.1. The figure demonstrates a sudden drop in the excited states for A = 178-186, linked to a prolate intruder configuration and shape coexistence. A more detailed discussion of this feature is provided in Sec. 2.5. As will be discussed in Sec. 2.3, lifetimes of 2_1^+ states enable deduction of the reduced tran-

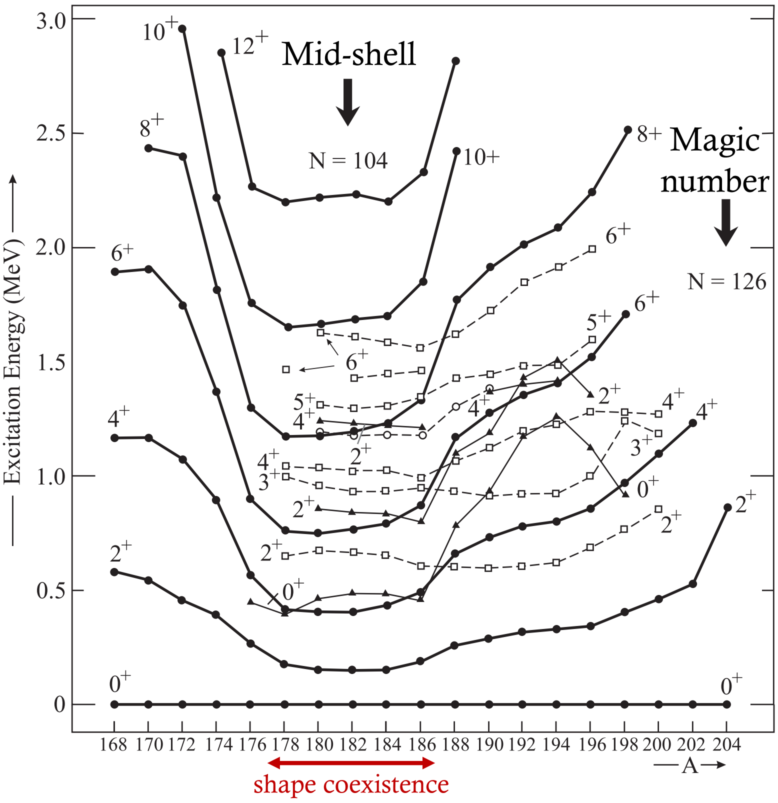

Figure 1.1: Energy-level systematics of even-mass Pt nuclei. Filled circles are states associated with the ground-state bands, while filled triangles are an excited band of different shape. Open squares are a gamma band, possibly built on different shapes in different mass regions, but interpreted as being built on the well-deformed band in the mid-shell region, as will be described in Sec. 2.6.4. A notable feature is the sudden drop in the excitation energy of the ground-state band members in the $^{178-186}$Pt region, indicating the existence of shape coexistence. Figure taken from Ref. [3].

sition probabilities for the $2_1^+ \rightarrow 0_1^+$ transitions, providing insights into the nuclear collectivity and shape. However, there are significant discrepancies in the measured 2_1^+ lifetimes for the A = 180-186 nuclei from the Evaluated Nuclear Structure Data File (ENSDF) database and more recent measurements. The reported lifetimes in ENSDF [4–7] used several techniques, namely the recoil-distance method (RDM) and $e^+ - \gamma$ method. More recent measurements [8–10] used both RDM and direct $\gamma - \gamma$ timing methods, the latter via exponential-convoluted Gaussian fitting and the Generalised Centroid Difference (GCD) methods (see Chapter 3 for details on lifetime measurement methods). These results are shown in Fig. 1.2, along with $^{188-198}$Pt values from ENSDF and a previous ANU PhD student's work [11,12], and are summarised in Tab. 1.1. As observed, while $^{190-198}$Pt follow a smooth trend, discrepancies are evident for $^{180-182}$Pt, highlighting the need to remeasure these lifetime values. The deviation for ^{188}Pt is also noted but not covered in this thesis.

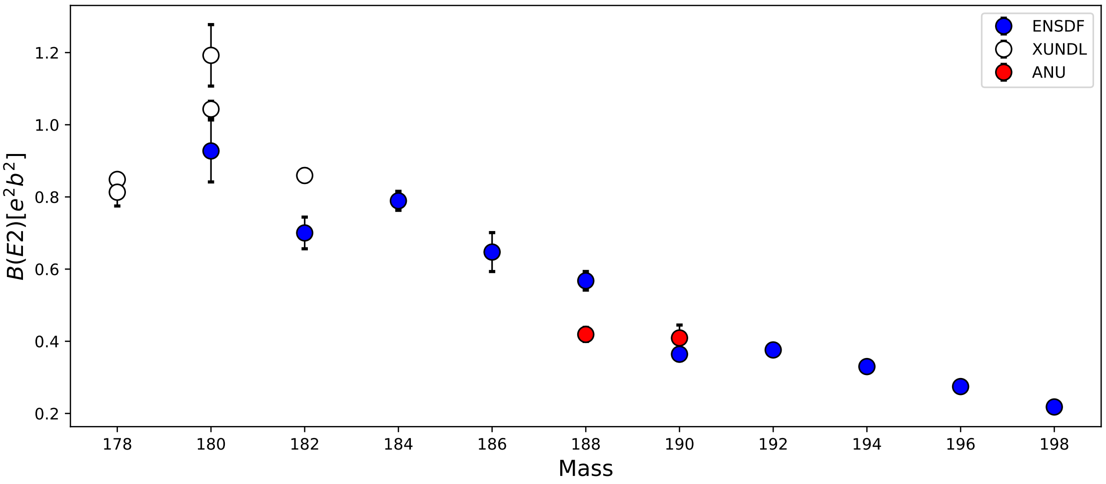

Figure 1.2: Values of the reduced transition strengths $B(E2; 2_1^+ \rightarrow 0_1^+)$ for the even-even platinum nuclei derived using the data from ENSDF [4–7, 13–19], more recent measurements (XUNDL) [8–10] and previous ANU measurements in $^{188-190}$Pt [11, 12].

Table 1.1: Lifetime values of platinum 2_1^+ states from ENSDF [4–7] and recent measurements [8–10], including derived values for the Grodzins product and reduced transition strengths.

Mass (A)	Ref.	Year	Method	Meanlife [ps]	Grodzins prod. [e^2b^2 keV]	B(E2) [e^2b^2]	B(E2) [W.u.]
180	[8]	2020	RDM	480(10)	0.84(2)	1.04(2)	172.8(36)
	[9]	2018	Convolution	420(20)	0.96(5)	1.19(6)	197.5(94)
	[9]	2018	GCD	420(30)	0.96(7)	1.19(9)	197.5(141)
	[4]		ENSDF (RDM)	540(50)	0.74(7)	0.93(9)	153.6(142)
182	[10]	2021	GCD	563(12)	0.70(1)	0.86(2)	140.3(30)
	[5]		ENSDF (RDM)	691(43)	0.57(4)	0.70(4)	114.3(72)
184	[6]		ENSDF ($e^+ - \gamma$)	519(17)	0.68(2)	0.79(3)	127.0(42)
186	[7]		ENSDF ($e^+ - \gamma$, RDM)	346(29)	0.66(6)	0.65(5)	102.6(86)

There is an empirical relationship regarding the reduced transition strengths, called the Grodzins product, as also summarised in Tab. 1.1 and shown in Fig. 1.3. The Grodzins product [20] is the empirical observation that the 2_1^+ excitation energy $E(2_1^+)$ and the reduced transition strength $B(E2; 0_1^+ \rightarrow 2_1^+)$ in even-even nuclei vary smoothly. Various studies have attempted to refine the Grodzins relation across

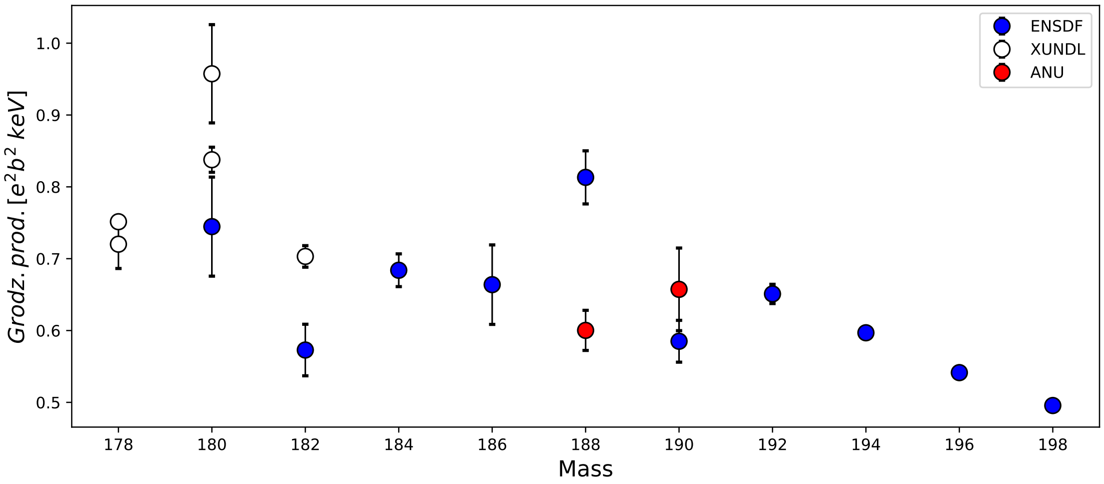

Figure 1.3: Values of the Grodzins product for the even-even platinum nuclei derived using the data from ENSDF [4–7, 13–19], more recent measurements (XUNDL) [8–10] and previous ANU measurements in $^{188-190}$Pt [11, 12].

different mass regions [21, 22]. Nevertheless, the general rule can be expressed in the following way[1]:

$$B(E2; 2_1^+ \rightarrow 0_1^+) \cdot E_{2_1^+} \cdot A^{2/3} \cdot Z^{-2} = const. \tag{1.1}$$

In addition to the transition strengths of B(E2), it can also be used as a guideline to discuss the feasibility of the obtained values. As shown in Fig. 1.3, discrepancies are also evident for $^{180-182}$Pt.

1.2 Thesis outline

This thesis reports the results of lifetime measurements for the 2_1^+ state in the $^{180-186}$Pt isotopes. The theoretical background relevant to this study is covered in Chapter 2. This is followed by a discussion of the lifetime measurement methods in Chapter 3 and the experimental setup in Chapter 4. Subsequently, the lifetime measurement results and detailed analysis procedures are presented in Chapter 5. These results are then compared to theoretical calculations in Chapter 6. Lastly, Chapter 7 describes the development of a new experimental setup for future lifetime measurements.

---

[1] The majority of studies typically use the transition probability $B(E2; 0_1^+ \rightarrow 2_1^+)$. However, employing $B(E2; 2_1^+ \rightarrow 0_1^+)$ is also appropriate given the relationship $B(E2; 0_1^+ \rightarrow 2_1^+) = 5B(E2; 2_1^+ \rightarrow 0_1^+)$.

Chapter 2

Theoretical background

This chapter first outlines the fundamentals of nuclear physics relevant to the study (Sec. 2.1-2.4), followed by a discussion of shape coexistence (Sec. 2.5) and the calculation methods for the multiple-band-mixing calculations used in this work to study shape evolution in the platinum isotopes of interest (Sec. 2.6).

2.1 Gamma decay

When the nucleus is excited, it may transition to a lower energy level or the ground state by emitting γ-ray photons, transmitting electromagnetic (EM) radiation, whose energy E_γ is equal to the difference in energy between the initial and final states, disregarding the minimal recoil kinetic energy [23]

$$E_\gamma = E_i - E_f. \tag{2.1}$$

In a γ-ray transition from an initial state of spin I_i to a final state of spin I_f, the photon carries the total angular momentum L described by [23]

$$\overrightarrow{L} = \overrightarrow{I_i} - \overrightarrow{I_f}, \tag{2.2}$$

which leads to the selection rule that limits the transition by emission of a single 2^L-pole photon as [23]

$$|I_i - I_f| \leq L \leq I_i + I_f. \tag{2.3}$$

In such transitions, the parity changes for electromagnetic radiation, EL and ML, are given by [23]

$$\pi(EL) = (-1)^L \qquad \pi(ML) = (-1)^{L+1}. \tag{2.4}$$

According to the equation above, electric and magnetic transitions of the same multipole order have opposite sign of parities, depending on whether the emitted γ ray is electric or magnetic. For a special case, the $0^+ \to 0^+$ γ transition is not allowed because photons with zero angular momentum do not exist. Such transitions, however, may occur through internal conversion or other exotic electromagnetic decay modes.

Weisskopf estimates provide an approximation of the single-particle transition rate, and enable us to generally predict which multipole is most likely to be emitted [23]. The EL transition rate is estimated to be

$$T_{\gamma,\, Weisskopf}(EL) \simeq \frac{8\pi(L+1)}{L[(2L+1)!!]^2} \frac{e^2}{4\pi\epsilon_0 \hbar c} \left(\frac{E_\gamma}{\hbar c}\right)^{2L+1} \left(\frac{3}{L+3}\right)^2 cR^{2L}. \tag{2.5}$$

With the nuclear radius given by $R = R_0 A^{1/3}$ where $R_0 \simeq 1.2$ [fm] and A is a mass number, we can approximate the lower electric multipole orders to be [23]

$$\begin{aligned} T_{\gamma,\, Weisskopf}(E1) &= 1.0 \times 10^{14} A^{2/3} E_\gamma^3 \\ T_{\gamma,\, Weisskopf}(E2) &= 7.3 \times 10^{7} A^{4/3} E_\gamma^5 \\ T_{\gamma,\, Weisskopf}(E3) &= 3.4 \times 10 A^{2} E_\gamma^7 \\ T_{\gamma,\, Weisskopf}(E4) &= 1.1 \times 10^{-5} A^{8/3} E_\gamma^9, \end{aligned} \tag{2.6}$$

where T_γ is in s^{-1} and E_γ is in MeV. On the other hand, the ML transition probability is [23]

$$\begin{aligned} T_{\gamma,\, Weisskopf}(ML) \simeq \frac{8\pi(L+1)}{L[(2L+1)!!]^2} &\left(\mu_p - \frac{1}{L+1}\right)^2 \left(\frac{\hbar}{m_p c}\right)^2 \left(\frac{e^2}{4\pi\epsilon_0 \hbar c}\right) \\ &\times \left(\frac{E_\gamma}{\hbar c}\right)^{2L+1} \left(\frac{3}{L+2}\right)^2 cR^{2L-2}, \end{aligned} \tag{2.7}$$

where μ_p is the proton magnetic moment and m_p is the proton mass. Replacing $[\mu_p - 1/(L+1)]^2$ with 10, as is common practice, and $R = R_0 A^{1/3}$, provides the following transition rate estimates for the lower magnetic multipole orders [23]

$$\begin{aligned} T_{\gamma,\, Weisskopf}(M1) &= 5.6 \times 10^{13} E_\gamma^3 \\ T_{\gamma,\, Weisskopf}(M2) &= 3.5 \times 10^{7} A^{2/3} E_\gamma^5 \\ T_{\gamma,\, Weisskopf}(M3) &= 1.6 \times 10 A^{4/3} E_\gamma^7 \\ T_{\gamma,\, Weisskopf}(M4) &= 4.5 \times 10^{-6} A^{2} E_\gamma^9, \end{aligned} \tag{2.8}$$

where T_γ is in s^{-1} and E_γ is in MeV. These estimations yield two simple observations: firstly, that lower multipolarities typically predominate, and secondly, that the probability of electric radiation is more than that of magnetic radiation by approximately two orders of magnitude in medium and heavy nuclei given the same multipole order.

2.2 Gamma-ray reduced transition probabilities

The reduced EL or ML transition probability, also known as the reduced transition strength, provides a quantitative indication of the transition strength between two nuclear states that reflects the nuclear structure alone, after factoring out the strong E_γ and angular momentum dependence of T_γ. It is calculated as follows [24]:

$$B(EL) = 4.57 \times 10^{-22} \frac{L[(2L+1)!!]^2}{8\pi(L+1)} \left(\frac{\hbar c}{E_\gamma}\right)^{2L+1} T_{\gamma,exp}(EL)\ [e^2 fm^{2L}] \tag{2.9}$$

$$B(ML) = 4.15 \times 10^{-20} \frac{L[(2L+1)!!]^2}{8\pi(L+1)} \left(\frac{\hbar c}{E_\gamma}\right)^{2L+1} T_{\gamma,exp}(ML)\ [\mu_N^2 fm^{2L-2}] \tag{2.10}$$

These T_γ values differ from those in Eq. 2.5 and 2.7; they are the observed values. The B(E2) reduced transition probabilities of interest in this study can be deduced from the measured lifetimes τ [ps] by rewriting the equation above as [25]

$$B(E2) = \frac{1}{\tau(1+\alpha)1.22 \times 10 E_\gamma^5}\ [e^2 b^2], \tag{2.11}$$

where α is the total internal conversion coefficient.

In the same way as in Sec. 2.1, when considering *Weisskopf estimates*, we can estimate the EL reduced transition probabilities $[e^2 fm^{2L}]$ for the lower multipole orders to be [24]

$$\begin{aligned} B_{Weisskopf}(E1) &= 6.4 \times 10^{-2} A^{2/3} \\ B_{Weisskopf}(E2) &= 5.9 \times 10^{-2} A^{4/3} \\ B_{Weisskopf}(E3) &= 5.9 \times 10^{-2} A^{2} \\ B_{Weisskopf}(E4) &= 6.3 \times 10^{-2} A^{8/3}, \end{aligned} \tag{2.12}$$

and the ML reduced transition probabilities $[\mu_N^2 fm^{2L-2}]$ as

$$\begin{aligned} B_{Weisskopf}(M1) &= 1.8 \\ B_{Weisskopf}(M2) &= 1.7 A^{2/3} \\ B_{Weisskopf}(M3) &= 1.7 A^{4/3} \\ B_{Weisskopf}(M4) &= 1.7 A^{2}, \end{aligned} \tag{2.13}$$

which helps us to make general predictions for the rates of different multipolarities. Reduced transition probabilities are also frequently expressed in Weisskopf units [W.u.], and can be calculated as measured transition strengths relative to the corresponding Weisskopf estimate:

$$B_{\mathrm{W.u.}(E/ML)} = \frac{B_{exp.}(E/ML)}{B_{Weisskopf}(E/ML)} \tag{2.14}$$

These estimates help us to make general predictions for the rates of different multipolarities. When the observed $B(E2)$ value in W.u. significantly exceeds the *Weisskopf estimate*, it indicates the presence of many-nucleon collective structures since Weisskopf units serve as an estimate of a single-particle like nuclear transition.

2.3 Nuclear shape and deformation

The shape of an atomic nucleus is one of its most fundamental properties. Assuming a sharp surface, the nuclear surface $R(\theta, \phi)$ can be described in a general way using a linear combination of spherical harmonics $Y_{\lambda\mu}$ [26] as

$$R(\theta, \phi) = R_0 \left[1 + \sum_{\lambda\mu} \alpha_{\lambda\mu} Y_{\lambda\mu}(\theta, \phi) \right], \tag{2.15}$$

where R_0 is the average radius of the nucleus and the $\alpha_{\lambda\mu}$ coefficients are the amplitudes of the spherical harmonics. This study considers only quadrupole deformation $\lambda = 2$, and the five quadrupole deformation amplitudes $\alpha_{2\mu}$ can be written in terms of two intrinsic coordinates β_2 and γ that are defined as

$$\begin{cases} \alpha_{20} = \beta_2 \cos\gamma \\ \alpha_{21} = \alpha_{2-1} = 0 \\ \alpha_{22} = \alpha_{2-2} = \frac{1}{\sqrt{2}} \beta_2 \sin\gamma. \end{cases} \tag{2.16}$$

In this coordinate system, the quadrupole deformation parameter β_2 is greater than zero and is the magnitude of the deformation along the major axis while $0 \leq \gamma \leq \frac{\pi}{3}$ represents the degree of symmetry to this axis. Nuclear shapes depend on β_2 and γ: they are spherical when $\beta_2 = 0$, prolate when $\gamma = 0$, oblate when $\gamma = \frac{\pi}{3}$ and triaxial when $0 < \gamma < \frac{\pi}{3}$ (see Fig. 2.1). A triaxial shape has unequal axis lengths, unlike axially symmetric shapes where two axes are equal. The key quantities for a deformed quadrupole nucleus are its moment of inertia $\mathcal{J}$ and the intrinsic quadrupole moment Q_0, and both can be expressed in terms of β_2 for axially symmetric nuclei.

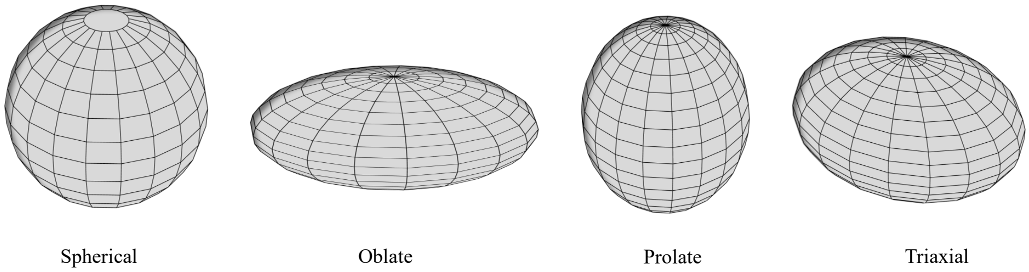

Figure 2.1: Illustration of spherical ($\beta_2 = 0$), oblate ($\gamma = \frac{\pi}{3}$), prolate ($\gamma = 0$) and triaxial ($\gamma = \frac{\pi}{6}$) nuclear shapes. The symmetry axis for both oblate and prolate shapes is by convention taken to be along the z-axis. Figure taken from Ref. [12].

Considering that the rigid body moment of inertia is $2/5\, Mr^2$, they can be described as [27]

$$\mathcal{J} = \frac{2}{5} AMR_0^2(1 + 0.31\beta_2), \tag{2.17}$$

$$Q_0 = \frac{3}{\sqrt{5\pi}} ZR_0^2\beta_2(1 + 0.16\beta_2). \tag{2.18}$$

A large moment of inertia and electric quadrupole moment are signs of stable nuclear deformation. Experimentally, the parameter β_2 can be deduced from the reduced transition probability by [27][1]

$$B(E2; 0_1^+ \to 2_1^+) = \frac{5}{16\pi} e^2 Q_0^2, \tag{2.19}$$

$$\therefore \beta_2 = \frac{4\pi}{3ZR_0^2} \left[\frac{B(E2; 0_1^+ \to 2_1^+)}{e^2} \right]^{1/2} \tag{2.20}$$

Therefore, the experimental values of the E2 reduced transition strength are crucial in the context of research on nuclear shapes.

2.4 Collective excitations

When the motion of individual nucleons is ignored, the nucleus can be simply described by the liquid-drop model. This model considers that nucleons move coherently as a drop of nuclear fluid. This approach works well for some aspects of nuclear behaviour and describes several modes of nuclear excitation, such as those that can

---

[1] This is model dependent, however it provides a good measure of deformation once β_2 is large enough.

be viewed classically as vibrations and rotations.

2.4.1 Rotational behaviour

Deformed nuclei exhibit collective rotational motion due to their spatial orientation, allowing rotation around an axis perpendicular to their major axis of deformation. For an axially symmetric rotor, the excitation energy is given by [27]

$$E(I) = E(0) + \frac{\hbar^2}{2\mathcal{J}}[I(I+1) - K^2], \tag{2.21}$$

where $E(0)$ is the bandhead energy, $\mathcal{J}$ is the nuclear moment of inertia and K represents the z' projection of the total angular momentum $\overrightarrow{I}$, as shown in Fig. 2.2. It is evident from the equation that nuclei exhibiting greater deformation with larger moments of inertia have smaller energy gaps between their states.

2.4.2 Vibrational behaviour

While rotational motion is possible only for deformed nuclei, any nuclei can be excited through vibrational modes. This is where the shape of the nucleus oscillates around an equilibrium shape. In the spherical case, the average shape is spherical, but the instantaneous shape is not, as shown in Fig. 2.3. Vibrations can be charac-

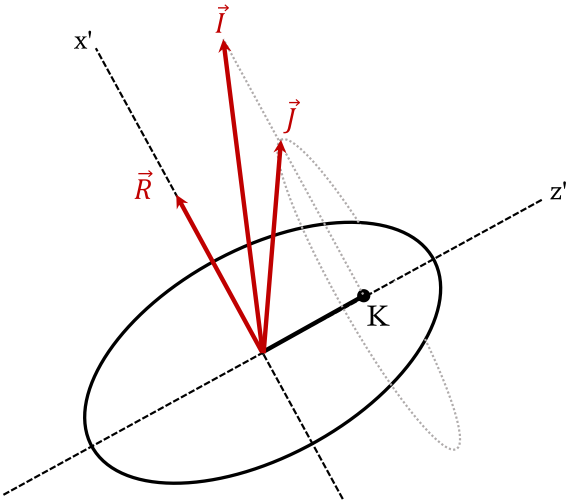

Figure 2.2: Schematic illustration of the rotational motion of a deformed nucleus around an axis perpendicular to its symmetry axis. The total angular momentum $\overrightarrow{I}$ is the sum of the rotational angular momentum $\overrightarrow{R}$ and the intrinsic angular momentum $\overrightarrow{J}$. The quantum number K is the projection of the total angular momentum $\overrightarrow{I}$ onto the z' axis in the nuclear frame (x', y', z').

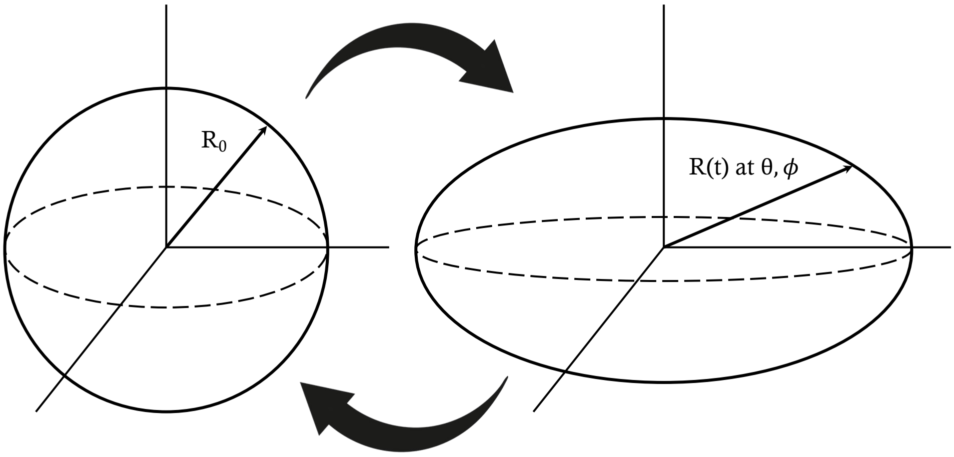

Figure 2.3: Schematic illustration of vibrational motion, where the nuclear surface oscillates around a spherical equilibrium shape. R_0 is the average radius.

terised by extending Eq. 2.15 to incorporate a time-dependent deformation [23]

$$R(\theta, \phi, t) = R_0 \left[1 + \sum_{\lambda\mu} \alpha_{\lambda\mu}(t) Y_{\lambda\mu}(\theta, \phi) \right] , \tag{2.22}$$

where $\alpha_{\lambda\mu}(t)$ are the instantaneous amplitudes. In spherical nuclei, specifically at lower excitation energies, the only collective vibrations commonly observed are the quadrupole $\lambda = 2$ and octupole $\lambda = 3$, illustrated in Fig. 2.4 [23].

Vibrations in deformed nuclei occur when the $\alpha_{\lambda\mu}$ values oscillate around non-zero values, i.e. the equilibrium shape is deformed. Two vibrational modes are possible: β or γ mode. In β vibrations ($K = 0$), the shape oscillates along the major axis, altering the magnitude of the deformation but retaining axial symmetry

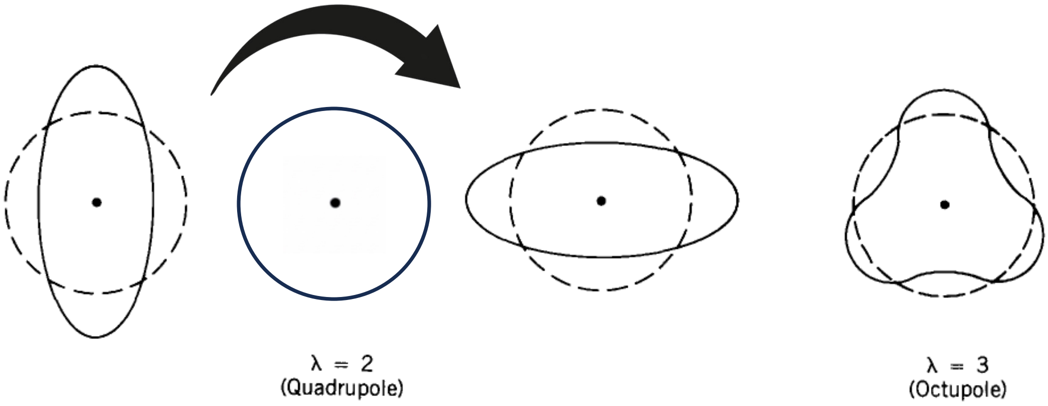

Figure 2.4: The two lowest vibrational modes of a nucleus are depicted. Dashed lines indicate the spherical equilibrium shape, while solid lines represent an instantaneous view of the vibrating surface. Figure taken from Ref. [23].

at all times. In contrast, γ vibrations ($K = 2$) involve oscillations perpendicular to the symmetry axis, causing transient triaxial deformations. These two vibration modes proposed by Bohr and Mottelson [26] are contentious, particularly regarding beta vibrations and shape coexistence, a lively topic in the field.

2.5 Shape Coexistence

Shape coexistence is a phenomenon where differently deformed nuclear shapes exist at similar excitation energies. This phenomenon was first discovered in ^{16}O [28], where the 0^+ ground state corresponds to ^{16}O having a doubly-closed shell and a spherical shape. Above the ground state, the first excited 0^+ state at 6.06 MeV is the bandhead of a rotational band having a deformed structure, as shown in Fig. 2.5. Since then, shape coexistence has been acknowledged to occur across all of the nuclear landscape, as a common feature rather than being a localised phenomenon [2].

Neutron-deficient mercury isotopes, which are adjacent to the platinum isotopes studied here, are also classic examples of shape coexistence. Figure 2.6 depicts the level schemes for ^{184,186,188}Hg, highlighting two distinct rotational bands. As previously mentioned in Sec. 2.4.1, the energy spacing in these bands reflects the magnitude of the deformation, with smaller energy gaps indicating more deformed shapes. Thus, one band originates from a weakly deformed oblate ground state and the other from a more deformed prolate state [29]. As mentioned in Sec. 1.1, a notable characteristic of shape coexistence is the parabolic trend of the excitation

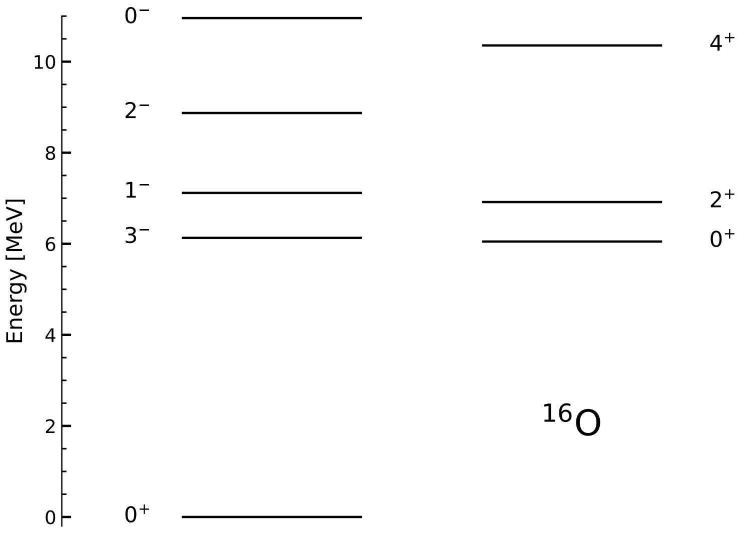

Figure 2.5: Energy level scheme of ^{16}O. A spherical ground state 0_1^+ coexists with a rotational band built upon a deformed excited state 0_2^+.

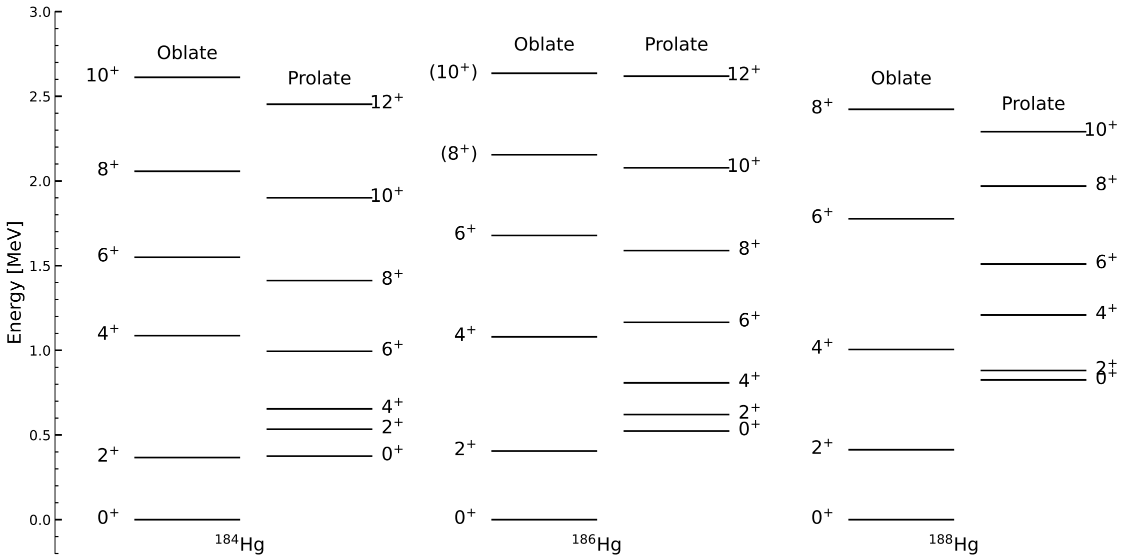

Figure 2.6: Level schemes for the neutron-deficient isotopes ^{184,186,188}Hg, showing the classic case of shape coexistence with two distinct rotational bands observed in each isotope.

energies of the deformed intruder band states, minimising near the neutron mid-shell. This can also be observed in the neutron-deficient mercury isotopes, as shown in Fig. 2.7.

A shell-model description has explained this energy behaviour through the intruder band originating from multiple particle-hole (mp-nh) excitations of protons across large shell gaps [2,30]. The energy cost for these excitations is compensated by a significant energy gain arising from the residual nucleon-nucleon interaction that causes deformation (described below as ΔE_Q). This interaction is maximised when the number of valence nucleons is large, so the excitation energies of the deformed intruder band typically reach a minimum around the mid-shell. The equation below [30] provides the energy of intruder bands in even-even nuclei as

$$E_{intr} = 2(\epsilon_{j_\pi} - \epsilon_{j'_\pi}) - \Delta E_{pair} + \Delta E_M + \Delta E_Q, \tag{2.23}$$

where j_π represents the regular orbital, j'_π is the intruder orbital and $2(\epsilon_{j_\pi} - \epsilon_{j'_\pi})$ indicates the energy required to excite a proton pair across the shell gap. ΔE_{pair} denotes the extra pairing correlation energy arising from the interactions between the particle and the hole pairs as

$$\Delta E_{pair} = 2S_p(Z,N) - S_{2p}(Z,N), \tag{2.24}$$

where S_p and S_{2p} correspond to the proton and two-proton separation energies.

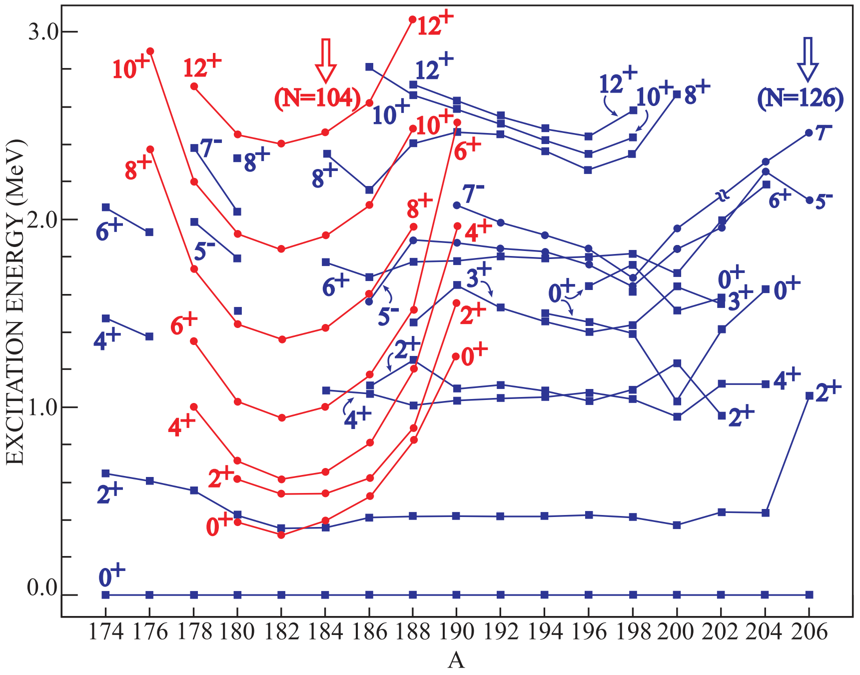

Figure 2.7: Energy-level systematics for the Hg nuclei. The red lines correspond to prolate structures and the blue lines to oblate structures. Figure taken from Ref. [3].

The typical monopole effect of the shell-model ΔE_M corresponds to the balance in binding energy when two protons are taken from a shell J'_π and put back in the shell J_π, and can be expressed as

$$\Delta E_M = 2 \sum_{J_\nu} (2J_\nu + 1) v^2_{J_\nu} (\bar{E}(J_\pi J_\nu) - \bar{E}(J'_\pi J_\nu)), \tag{2.25}$$

where $v^2_{J_\nu}$ represents the occupation probabilities, and $\bar{E}(J_\pi J_\nu)$ are the average matrix elements for proton-neutron interactions. This quantity depends on the neutron number and can be attractive or repulsive. The final term ΔE_Q is the energy gain due to the proton-neutron quadrupole interaction. This force changes spherically symmetric proton-proton or neutron-neutron pairs (with angular momentum $I^\pi = 0^+$) into pairs with $I^\pi = 2^+$. This effect, known as core polarisation, drives quadrupole deformation, and the energy gain is largest when the number of valence nucleons is at a maximum. Figure 2.8 shows a schematic plot of these effects against neutron number N between the two closed neutron shells, showing that the overall energy minimises around the mid-shell.

To investigate shape coexistence through experimental data, it should be noted that the observed experimental states are mixed rather than pure, comprising quantum mechanical admixtures of various deformed/spherical configurations. While lower-excited states of lighter mercury isotopes are described by two bands, prolate

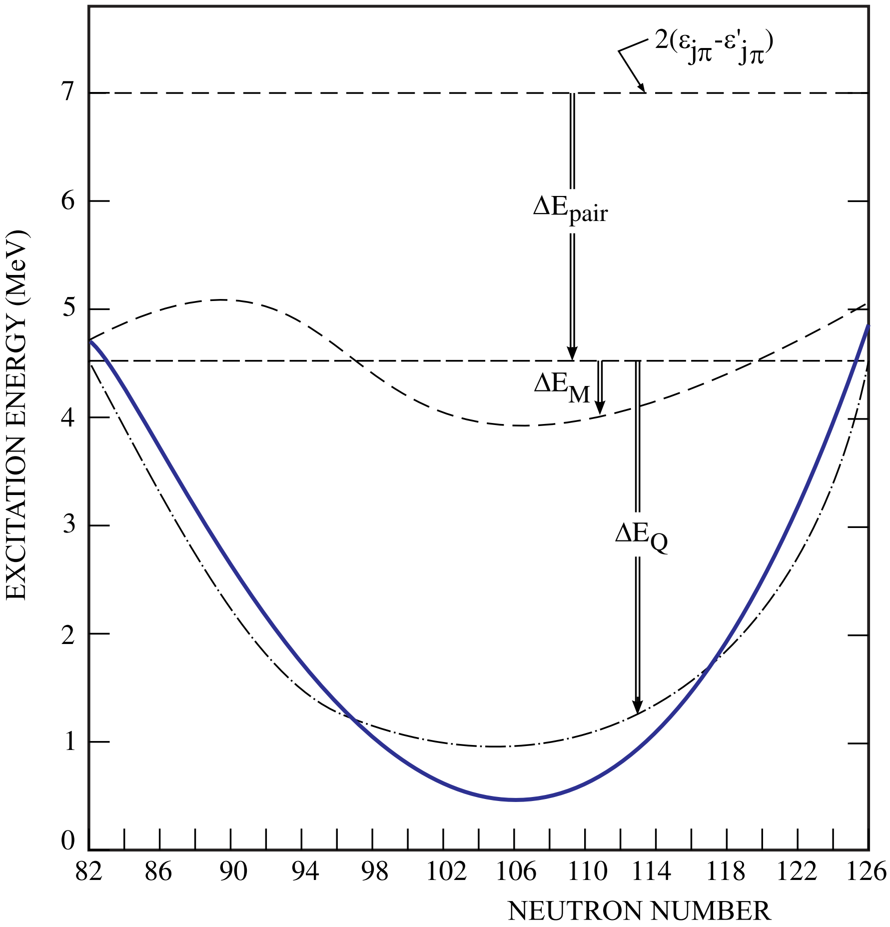

Figure 2.8: A schematic plot of the different components contributing to the energy of an intruder band E_{intr} (blue line, from Eq. 2.23) as a function of neutron number. The blue line shows the total of these different effects. Figure taken from Ref. [2].

and oblate, the lighter platinum isotopes examined in this thesis exhibit greater complexity, featuring three bands, including an additional prolate band. To address this, multiple-band-mixing calculations were performed, as explained in the following section.

2.6 Band-mixing model

To interpret the complex structure of shape coexistence in the lighter platinum isotopes where three different bands are mixed, this work employed a phenomenological band-mixing model [31, 32]. The central assumption is that the nuclear band structure can be described by spin-independent mixing between several unperturbed (unmixed) rotational bands; this simplified model structure allows for a clear interpretation of how the mixing between different bands evolves. The mixing probabilities were obtained through fitting the known energy levels by mixing the states that arise from the Variable Moment of Inertia (VMI) model [33] of the bands. Subsequently, mixing amplitudes of each state are used to predict additional observables, including B(E2) strengths and γ-ray branching ratios.

Numerous studies have applied the band-mixing model to lighter platinum isotopes and neighbouring nuclei. A simple two-band mixing model considering the oblate and prolate bands was applied to reproduce the observed energies in $^{172-184}$Os, $^{174-188}$Pt, $^{180-188}$Hg and $^{186-188}$Pb [29, 34–38]. Furthermore, a three-band mixing approach was carried out in ^{170}Os [39] and $^{176-182}$Pt [32, 40]. With more expanded experimental data now available after previous studies in the lighter platinum region, this work presents a two-band mixing interpretation for ^{178}Pt and a three-band mixing calculation for $^{180-186}$Pt, marking the first application for $^{184-186}$ Pt.

2.6.1 The VMI model

The VMI model [33] defines the unperturbed state energies $E_n(I)$ at spin I in a rotational band n of a nucleus. The state energies are determined by three parameters: moment of inertia at zero spin ($\mathfrak{I}_0^n$), a “softness” parameter (C^n) and a band-head energy (E_0^n). The specific state energy is given by:

$$E_n(I,\, \mathfrak{I}_0^n,\, C^n,\, E_0^n) = E_0^n + \frac{I(I+1)}{2\mathfrak{I}_I^n} + \frac{1}{2}C^n(\mathfrak{I}_I^n - \mathfrak{I}_0^n)^2. \tag{2.26}$$

The moment of inertia for a given spin, $\mathfrak{I}_I$, is determined for each state by the equilibrium condition that the energy is at a minimum with respect to the moment of inertia:

$$\frac{\partial E(\mathfrak{I}_I^n)}{\partial \mathfrak{I}_I^n} = 0. \tag{2.27}$$

To describe more complex structures, such as excited bands with non-zero K and/or bands experiencing particle alignment, i_x, the rotational term $I(I+1)$ is replaced by the core angular momentum $R(R+1)$. A widely used approximation to determine R is given by [41]:

$$R \approx \sqrt{\left(I + \frac{1}{2}\right)^2 - (K^n)^2} - i_x^n - \frac{1}{2}. \tag{2.28}$$

The different bands can exhibit different values for C^n, $\mathfrak{I}_0^n$, K^n, i_x^n and E_0^n. This allows the modelling of coexisting bands resulting from differing deformations and with different alignments and/or K-values.

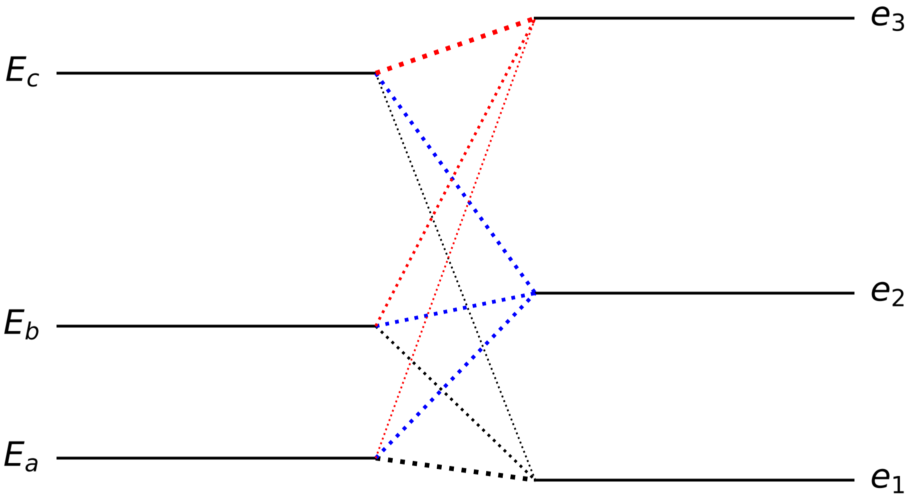

Figure 2.9: Example level scheme showing three states of the same spin within the a , b and c bands, mixing to create three observed states with energies e_1, e_2 and e_3. The thicknesses of the dotted lines indicates the mixing amplitudes.

2.6.2 Mixing between unperturbed bands

The perturbed (=observed) energies are calculated by assuming a spin-independent interaction between states within the unperturbed bands that have the same spin. Consider the level scheme depicted in Fig. 2.9, where the unperturbed states, all with the same spin, are denoted as E_a, E_b and E_c, and are mixed to generate the perturbed energies e_1, e_2 and e_3. Given spin-independent interactions, V_{ab}, V_{ac} and V_{bc}, between the bands, the perturbed energies, e_i, can be determined from the eigenvalues of matrix equation shown in Eq. 2.29, where (A^i_a, A^i_b, A^i_b) represent the associated eigenvectors that describe the wavefunction components of the unperturbed bands in the observed mixed states.

$$\begin{pmatrix} E_a(I) & V_{ab} & V_{ac} \\ V_{ab} & E_b(I) & V_{bc} \\ V_{ac} & V_{bc} & E_c(I) \end{pmatrix} \begin{pmatrix} A^i_a \\ A^i_b \\ A^i_c \end{pmatrix} = e_i \begin{pmatrix} A^i_a \\ A^i_b \\ A^i_c \end{pmatrix} \qquad i = 1, 2, 3 \tag{2.29}$$

Therefore, by fitting the observed energy states with the modelled values e_1, e_2 and e_3, all parameters used for the fitting can be derived.

2.6.3 Calculating transition strengths

With the band-mixing models providing the mixing amplitudes A_n for each spin state, the E2 transition strengths from an initial state i to final state f can be calculated using

$$B(E2; I_i \to I_f) = \left[\sum_{n_1, n_2} A^i_{n_1} A^f_{n_2} \langle n_1 \,|\, E2 \,|\, n_2 \rangle \right]^2 \qquad (n_1,\, n_2 \in \{a,\, b\,, c\}). \tag{2.30}$$

In this expression, the matrix elements are expressed in terms of the intrinsic quadrupole moment matrix elements

$$\langle n_1 | E2 | n_2 \rangle = \sqrt{\frac{5}{16\pi}} \langle I_{n_1}\, K^{n_1}\, 2\, \Delta K \,|\, I_{n_2}\, K^{n_2} \rangle e \langle n_1 \,|\, Q_0 \,|\, n_2 \rangle, \tag{2.31}$$

where K^{n_1} and K^{n_2} denote the K-values corresponding to the n_1 and n_2 bands, respectively, and $\Delta K = K^{n_1} - K^{n_2}$. Regarding the quadrupole moments $\langle n_1 \,|\, Q_0 \,|\, n_2 \rangle$, the off-diagonal matrix elements ($n_1 \neq n_2$) are set to zero for simplicity, and the diagonal elements, for which ΔK is zero, can be calculated using the empirical relation [33]

$$\langle n \,|\, Q_0 \,|\, n \rangle \approx k \sqrt{\mathfrak{I}^n_{02}} = k \sqrt{(\mathfrak{I}^n_0 + \mathfrak{I}^n_2)/2} \qquad k = 45\,[\text{eb}][\text{keV}^{1/2}], \tag{2.32}$$

where the constant $k = 45$ [eb][keV$^{1/2}$] is a parameter that was fitted to reproduce the quadrupole moments in $^{168-172}$W [39]. Although the absolute B(E2) transition strengths are proportional to k^2, the branching ratios, i.e. the ratio of B(E2) transition strengths, are unaffected by k. Hence, k was included in the mixing calculation fits, along with the energies (see Sec. 6).

It is necessary to consider whether the signs of the quadrupole moments for prolate and oblate deformations are the same or opposite. The previous study of two-band mixing in $^{184-188}$Hg [42] and ^{183}Hg [41] concluded that assuming these quadrupole moments have the same sign well reproduces the experimental B(E2) ratios. We also evaluated this in ^{178}Pt using the simple two-band mixing, as will be discussed in Sec. 6.1.

2.6.4 Band-mixing model in $^{178-186}$Pt

The platinum isotopes from$A = 178-186$ show experimental evidence of two distinct rotational bands, the more deformed prolate band (labelled d band) and the less deformed oblate band (labelled g band), along with, in some cases, more bands, see e.g. Refs. [43–47]. In principle, each platinum isotope may have two K=2 γ-vibrational bands associated with the g band and d band, respectively. As shown in the previous study of two-band mixing [34], the d band consistently has the lowest excitation energy in $^{180-186}$Pt; therefore, we assume that the γ band built on the d band has more impact on the mixing. Previous studies also suggested the existence of the β band [44, 45], however, in this study only the γ band built in the d band is used due to insufficient experimental data to characterise additional bands. To avoid the necessity of addressing the s band [32], which carries aligned angular momentum i_x (see Eq. 2.28), the data chosen for fitting were limited to states with $I \leq 12\hbar$, keeping the analysis sufficiently below the expected s-band crossing [32, 44].

In conclusion, this study includes d , g and γ bands built on the d band, for band-mixing calculations, with $K = 0$ for the d and g bands, $K = 2$ for the γ band and $i_x = 0$ for all. Thus, nine fitting parameters are required, C^n, $\mathfrak{I}_0^n$, E_0^n of each band, and three interaction parameters. A technical challenge faced here is the limited number of observed non-yrast states[2], which makes it difficult to determine independent inertial parameters for all three bands. Therefore, the inertia parameters, $\mathfrak{I}_0$ and C, of the γ band are constrained using two approaches: the *common way* and the *fixed way*. In the common way, the inertial parameters are common to both the d band and γ band, as in Ref. [32]. On the other hand, the fixed way predetermines the γ band parameters using the yrast odd-spin energy states. This assumes that these states are pure members of the γ band, similar to the application used in Ref. [40], due to the absence of mixing as the d and g bands do not have odd-spin states.

Three-band mixing calculations with d and g bands and a γ band built on the d band, were previously performed for the platinum isotopes of the mid-shell region, using both the common way [32] and the fixed way [40]. These calculation results for ^{180}Pt are shown in Figs. 2.10 and 2.11 and use the previously published fitted parameters. The figures also show experimental energy values, which include measurements obtained subsequent to the aforementioned studies, such as the non-yrast 6^+ state. The poor fits indicate that the prior calculations fail to account for the recent experimental data. A similar situation is observed with other platinum isotopes, underscoring the necessity to re-perform the mixing calculations within this platinum region.

---

[2] Here, *yrast* denotes the lowest-energy state for a given angular momentum I; *non-yrast* refers to excited states with the same I above the yrast line.

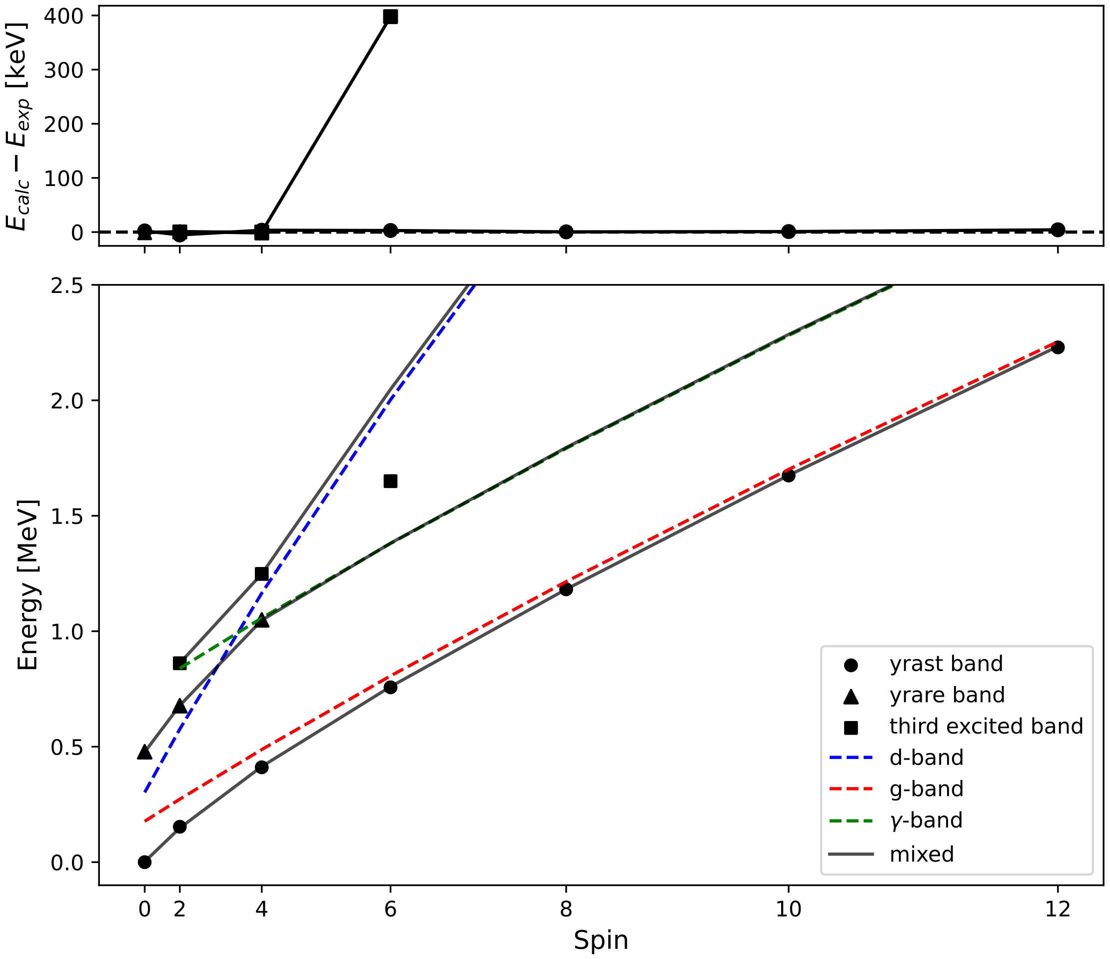

Figure 2.10: Three-band mixing for ^{180}Pt using the common way and using fitted parameters from the previous study [32], showing deviations that are now observed with the recently measured non-yrast 6^+ state.

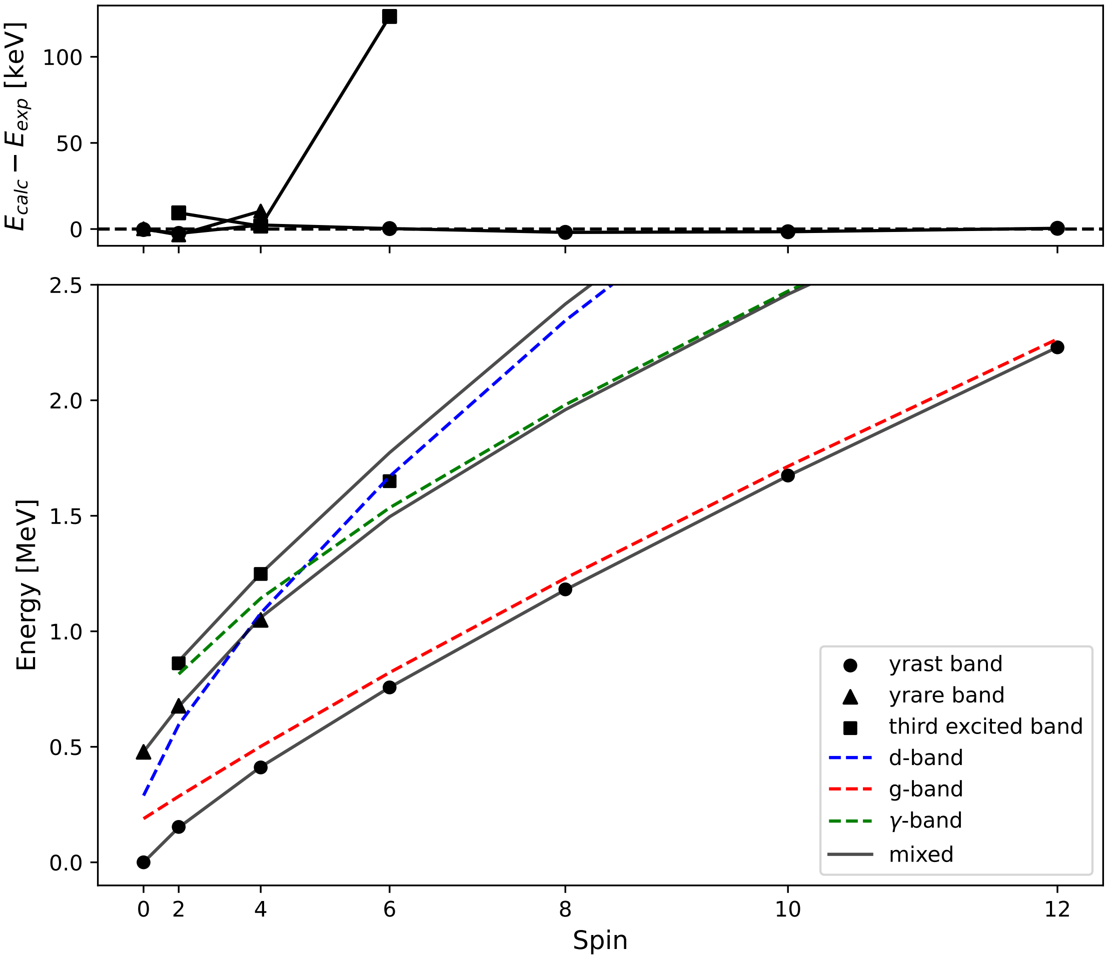

Figure 2.11: Three-band mixing for ^{180}Pt using the fixed way and using fitted parameters from the previous study [40], showing deviations that are now observed with the recently measured non-yrast 6^+ state.

Chapter 3

Lifetime measurement methods

Since the Pt isotopes of interest exhibit long-lived isomers at higher excitation energy (8^- state in ^{184,186}Pt [46,47] and an isomer indication in ^{180}Pt [44]) that feed into the lower-excitation shorter-lived states of interest, it has been challenging to measure accurate lifetimes of the 2_1^+ states in these Pt isotopes, particularly by the recoil-distance method (RDM). The RDM determines a lifetime by varying the distance between the target and stopper and comparing the fraction of γ rays emitted in flight (Doppler-shifted) to those emitted after stopping, with the basic assumption that the nuclear state of interest is populated promptly by the reaction [48]; for a recent review of the RDM, see Ref. [49]. However, delayed feeding from long-lived isomers adds slow, time-shifted decay components that cannot always be separated from the sought decay of promptly populated states.

On the other hand, the gamma-gamma fast timing method [50] can isolate the lifetime of the state of interest and makes a direct measurement of the lifetime possible. In these direct-timing measurements, the lifetime of a level of interest can be obtained by measuring the time difference between two γ rays, one feeding the state (E_{feed}) and one decaying from it (E_{decay}). For our study of $^{180-186}$Pt, Fig. 3.1 shows the specific transitions that were used to determine the lifetimes of the 2_1^+ states. This fast-timing technique relies on the relative time difference between the

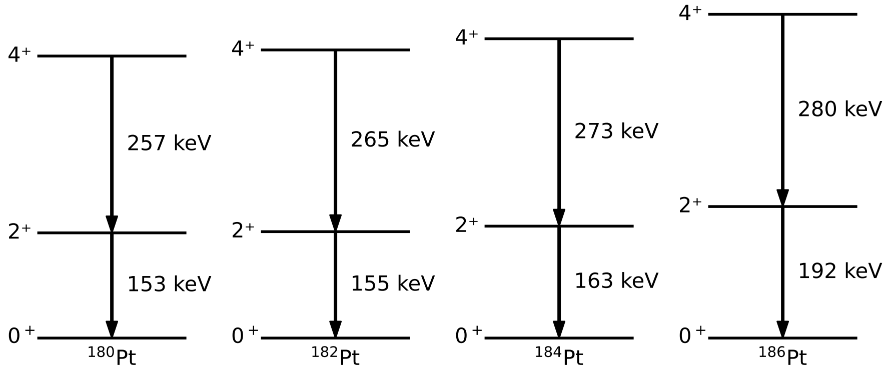

Figure 3.1: Feeding $4_1^+ \rightarrow 2_1^+$ γ-ray energies, E_{feed}, and decaying $2_1^+ \rightarrow 0_1^+$ energies, E_{decay}, in $^{180-186}$Pt, that were used to determine the lifetimes of the 2_1^+ states.

feeding and decaying γ rays, so it does not depend on the start time of feeding; consequently, it is not affected by the delayed population of long-lived isomers. The following sections elaborate on the analysis methods and characteristics of this direct-timing measurement technique.

3.1 Time-walk characterisation

The detection time of a γ ray can be affected by several factors such as the length of the signal cable and the shape of the detector's output pulse. For example, in the pulse shape, when two signals with different amplitudes arrive simultaneously and the same threshold is used to recognise them, the one with the higher amplitude has a steeper slope and reaches the threshold faster, while the lower amplitude signal does so more slowly. This causes a perceived time difference, known as time walk, even though both signals arrive at the same time.

Constant fraction discrimination (CFD) is an electronic method designed to provide amplitude-independent timing information, unaffected by factors such as scintillator material, photomultiplier tube (PMT) or setup geometry [50, 51]. Upon receiving the original input pulse, the CFD generates two pulses: one is delayed by the delay time t_d, while the other remains undelayed but is attenuated by a constant fraction $f \in [0, 1]$. Subtracting the undelayed pulse from the delayed pulse results in a bipolar pulse, and by choosing appropriate t_d and f, the baseline intersection occurs at the same point regardless of amplitude, as shown in Fig. 3.2.

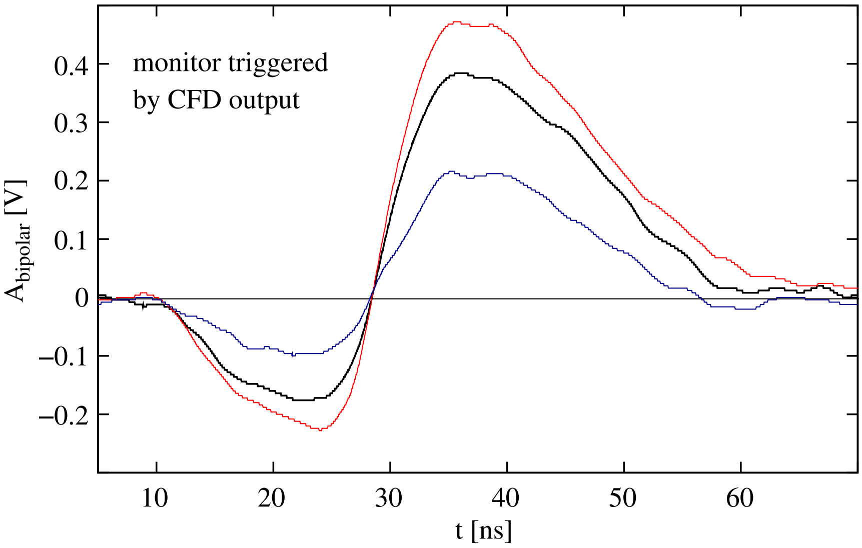

Figure 3.2: Bipolar pulses generated by a CFD with input pulses having different amplitudes. It can be seen that the position of the zero crossing at ~29 ns is independent of the original signal height. Figure taken and adapted from Ref. [51].

Although the CFD timing system is amplitude independent, the determination of the zero-crossing time remains amplitude dependent, introducing a time walk, ΔT_A, which occurs due to the charge sensitivity to the slope of the bipolar signal crossing the zero baseline, and the time required to register the crossing, as shown in Fig. 3.3. Considering a linear bipolar pulse over the time ΔT necessary to accumulate the charge q, the amplitude-dependent time-walk ΔT_A, defined as $t_1 - t_0$ or $t_2 - t_0$ in Fig. 3.3, can be expressed by

$$\begin{aligned} q &\propto \int_{t_0}^{t_1} \left.\frac{dA_{bipol.}}{dt}\right|_{t_0} (t - t_0) dt \\ \therefore q &\sim \left.\frac{dA_{bipol.}}{dt}\right|_{t_0} \frac{\Delta T_A^2}{2} \\ \therefore \Delta T_A &= \sqrt{\frac{2q}{\left.\frac{dA_{bipol.}}{dt}\right|_{t_0}}}. \end{aligned} \tag{3.1}$$

Given the CFD timing can be represented as

$$T_{CFD} = t_0 + \Delta T_A, \tag{3.2}$$

and there is a linear relationship between amplitude and energy [50, 51], the CFD time-walk characteristics are expected to be expressed by

$$T(E)_{CFD} = \frac{a}{\sqrt{E + b}} + c. \tag{3.3}$$

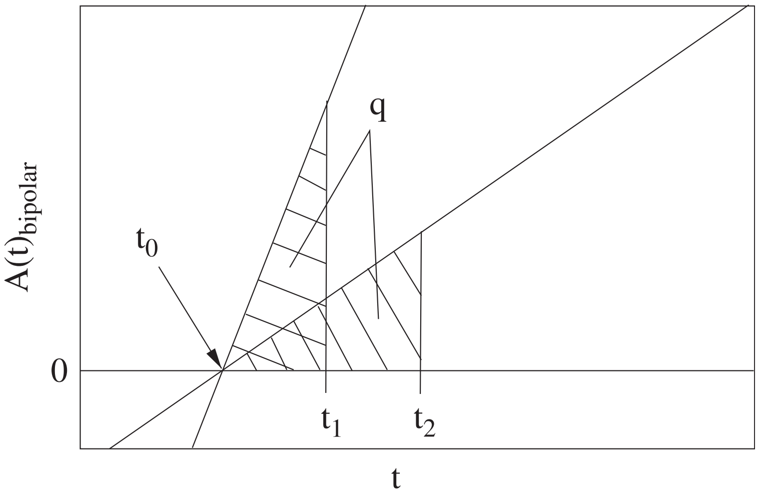

Figure 3.3: Amplitude-dependent slope of the bipolar signal at the zero-crossing time. This difference causes the accumulated charge q to be collected at varied times t_i, leading to a time-walk $\Delta T_A = t_i - t_0$. Figure taken from [52].

This relationship will be applied to the Generalised Centroid Difference (GCD) method for determine fast lifetimes that is explained in Sec. 3.3.3.

3.2 Background subtraction

In an ideal scenario without any background, the time-difference spectrum between E_{decay} and E_{feed} can readily determine lifetimes. However, actual measurements are often contaminated by background signals, such as Compton scattering from higher-energy transitions, which alter the “true” E_{decay}-E_{feed} time distribution, resulting in contamination in the “measured” distribution. The effect of background is depicted in Fig. 3.4, taken from the work of E.R. Gamba *et al.* on background subtraction [53]. The left illustrates the $\gamma - \gamma - \Delta T$ cube, where γ denotes the feeding/decaying γ-ray energies and ΔT is the time difference between them. The schematic figure on the right shows that Compton scattering events, such as Compton-E_{decay}, E_{feed}-Compton, and Compton-Compton events, occur beneath the true E_{decay}-E_{feed} peak. Let $p|p^t$ and $p|p^m$ represent the true and measured E_{decay}-E_{feed} time-difference distributions, respectively. Also, let $bg|p^m$, $p|bg^m$, and $bg|bg^m$ denote the measured time differences for Compton-E_{decay}, E_{feed}-Compton, and Compton-Compton events under the $p|p^t$ peak, respectively. Consequently, the true time-difference distribution $p|p^t$ can be described by

$$p|p^t = p|p^m - p|bg^t - bg|p^t - bg|bg^t. \tag{3.4}$$

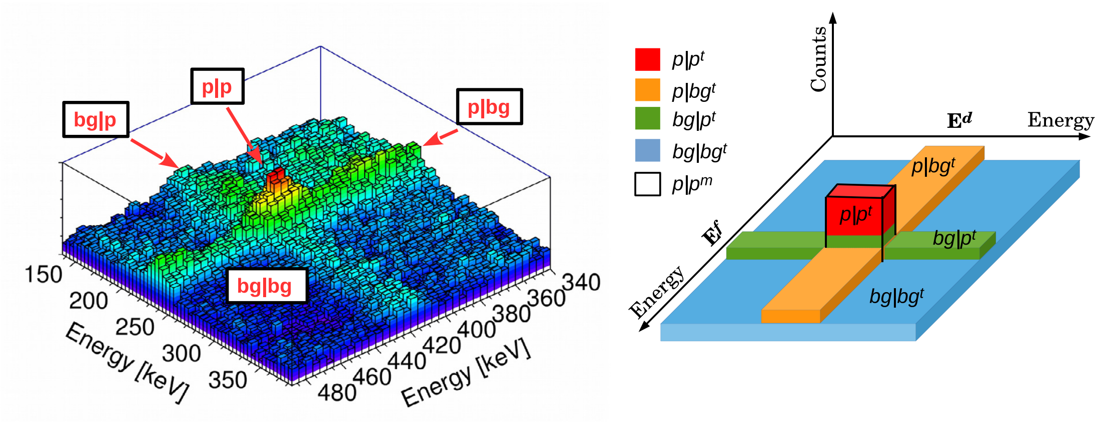

Figure 3.4: The experimental $\gamma - \gamma - \Delta T$ cube derived from ^{252}Cf source data, focusing on the $4^+ \to 2^+ \to 0^+$ cascade in ^{110}Ru (left), alongside a schematic of the background composition in this cube (right), showing the measured peak, $p|p^m$, consists of not only the true peak component, $p|p^t$, but also three background components, $bg|p^t$, $p|bg^t$, and $bg|bg^t$. Figure taken from Ref. [53].

To express the above equation solely with “measured” distributions, the following relationships are used.

$$\begin{aligned} p|bg^m &= p|bg^t + bg|bg^t, \\ bg|p^m &= bg|p^t + bg|bg^t, \\ bg|bg^m &= bg|bg^t. \end{aligned} \tag{3.5}$$

This leads to the rewritten equation:

$$p|p^t = p|p^m - p|bg^m - bg|p^m + bg|bg^m. \tag{3.6}$$

Note that the three background distributions are normalised with respect to the $p|p^m$ gate area. Since each background gate was sampled from various energy regions, we have to consider the energy-dependent time-walk characteristic as discussed in Sec. 3.1, which will be described in Sec. 5.3.

3.3 Analysis method

In the case where the lifetime τ is negligible and the detector has perfect time resolution, the time-difference distribution is a delta function. In reality, for a prompt decay, the resolution is non-zero and the distribution usually takes a Gaussian form; we call this the prompt response function. In real-life situations where τ is not negligible, both the Gaussian prompt response component and the decay slope appear in the time distribution. Also, when $E_{feed} \neq E_{decay}$, the time-walk effect must be considered.

3.3.1 The decay slope method

When the lifetime of a state significantly exceeds the time resolution of the detector, the Gaussian component and the decay slope become distinct enough, making it feasible to fit the spectrum, away from the prompt position, solely to the decay function given by

$$C(t) = C_0 \cdot e^{-\lambda t}. \tag{3.7}$$

This method is widely used in nuclear spectroscopy studies.

3.3.2 Exponential-convoluted gaussian fitting method

When the lifetime of a state is comparable to, or slightly longer than, the time resolution of the detector, the Gaussian component merges with the decay component, forming a curve that follows that of a Gaussian convoluted with an exponential function. This takes the analytical form

$$N(t) = A \ \exp\left(-\frac{1}{\tau}\left(t - t_0 - \frac{\sigma^2}{2\tau}\right)\right) \text{erfc}\left(-\frac{1}{\sqrt{2}\sigma}\left(t_0 + \frac{\sigma^2}{\tau} - t\right)\right), \qquad (3.8)$$

where t_0 is the time zero, σ is the width parameter corresponding to the time resolution, A is a constant reflecting the number of γ-ray coincidences observed, and erfc is the complementary error function, defined as $\text{erfc}(x) = \frac{2}{\sqrt{\pi}} \int_x^\infty e^{-t'^2} \, dt'$. By fitting the time-difference distribution to this function, we can determine the lifetime τ.

In this study, the convolution method was used, but to fit the data, the experimental forward and reversed spectra were summed together and this sum was fitted to a sum of two Gaussian-convoluted functions with a common lifetime parameter. The concept of how this was done is demonstrated in Fig. 3.5. Note that although the fit was done to the summed data, the final results and fits shown elsewhere in this thesis generally show only the forward spectrum alone, with a fitted curve based on Eq. 3.8.

3.3.3 Generalised Centroid Difference (GCD) method

The Generalised Centroid Difference (GCD) method is typically applied when the lifetime is comparable to, or shorter than, the time resolution of the detector, al-

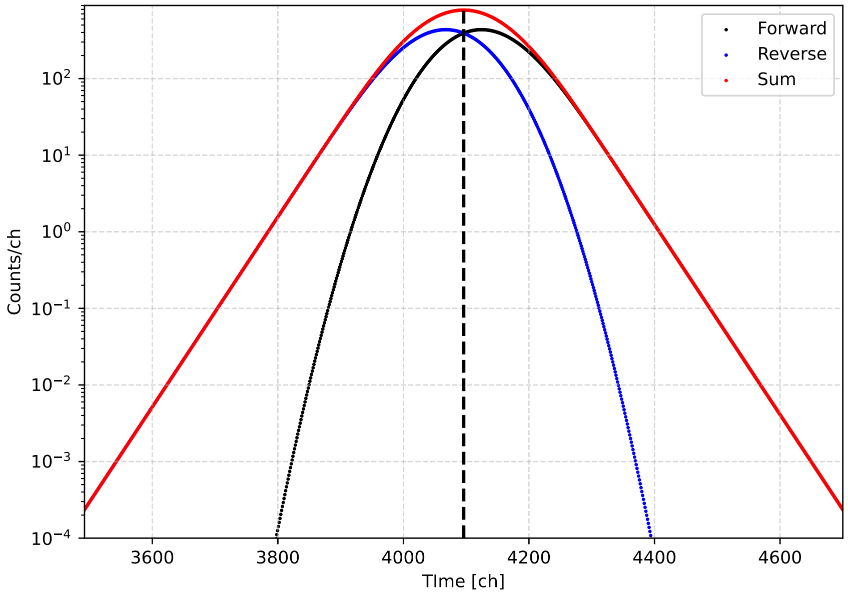

Figure 3.5: The sum (red) of forward (black) and reversed (blue) Gaussian convoluted with an exponential spectra.

though it is a general approach and can also be used in cases where the convolution method is also applicable. It relies on the fact that the centroid of the distribution is the average time to decay and hence corresponds to the state meanlife. This method, however, needs to account for the time-walk characteristic that was discussed earlier in Sec. 3.1.

Figure 3.6 illustrates the time-difference spectra for the forward ($E_{feed} \rightarrow E_{decay}$) and reverse ($E_{decay} \rightarrow E_{feed}$) cascades. The observed spectrum centres are labelled as C_{fwd} and C_{rev}, while $C^{\text{P}}_{\text{fwd}}$ and $C^{\text{P}}_{\text{rev}}$ denote the centres of the prompt response function. Note that as $C^{\text{P}}_{\text{fwd}}$ and $C^{\text{P}}_{\text{rev}}$ depend on the γ-ray energies and their order, they are not necessarily symmetric around time=0. Given ΔC as the difference between the spectrum centres of the measured forward and reverse cascades, we can express the relationship as

$$\begin{aligned} \Delta C &= 2\tau + (C^{\text{P}}_{\text{fwd}} - C^{\text{P}}_{\text{rev}}) \\ &= 2\tau + \text{PRD}_{E_{feed} \rightarrow E_{decay}}, \end{aligned} \tag{3.9}$$

where PRD stands for Prompt Response Difference, which must be independently calibrated. According to the time-walk discussion in Sec. 3.1 and Ref. [50, 51], the $\text{PRD}_{E_{feed} \rightarrow E_{decay}}$ for LaBr_3 detectors can be expressed through the following relationships:

$$\text{PRD}_{E_{feed} \rightarrow E_{decay}} = \text{PRD}_{E_{feed} \rightarrow E_{ref}} - \text{PRD}_{E_{ref} \rightarrow E_{decay}} \tag{3.10}$$

$$\text{PRD}_{E_{feed/decay} \rightarrow E_{ref}} = \frac{a}{\sqrt{E_{feed/decay} + b}} + cE_{feed/decay} + d \tag{3.11}$$

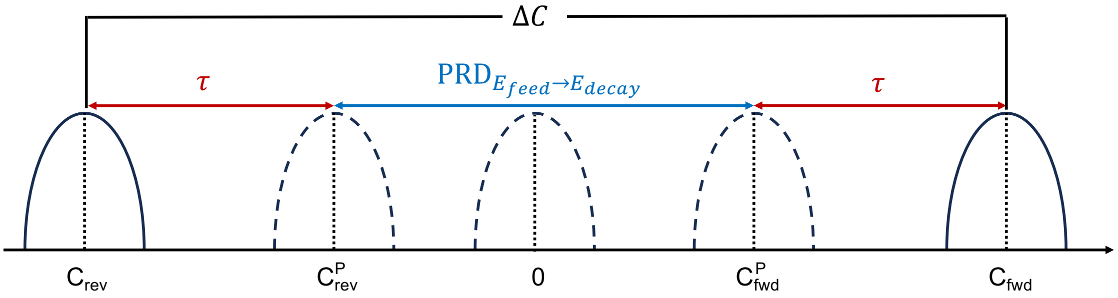

Figure 3.6: Conceptual explanation of the Generalised Centroid Difference (GCD) method. Two prompt response functions of the forward C_{fwd} and reversed C_{rev} spectra centre at $C^{\text{P}}_{\text{fwd}}$ and $C^{\text{P}}_{\text{rev}}$, depending on the energy values E_{feed} and E_{decay}, which are not necessarily symmetric with respect to $\Delta T = 0$.

$$\mathrm{PRD}_{E_{feed}\rightarrow E_{decay}} = -\mathrm{PRD}_{E_{decay}\rightarrow E_{feed}} \tag{3.12}$$

where the parameters a, b, c and d are fitted constants, and E_{ref} is a reference γ-ray energy. The linear term, $cE_{feed/decay}$, in Eq. 3.11 was included to account for a linear time walk, as in Ref. [50, 51]. Typically, a source with well-known lifetimes and multiple cascades, such as ^{152}Eu, is used to measure the PRD at various energies. The calibration is performed by fitting Eq. 3.11 to the data for various energies relative to a reference, such as the 344-keV γ ray, creating a 2D PRD curve. However, this typical approach treats some data with more credence than others and it has the offset parameter d due to its arbitrary alignment, so the ANU group has proposed a more straightforward approach by performing a fit to a 3D surface. By substituting Eq. 3.11 into Eq. 3.10, we obtain a single function for the PRD between any two energies:

$$PRD_{E_{feed}\rightarrow E_{decay}} = \frac{a}{\sqrt{E_{feed}+b}} + cE_{feed} - \frac{a}{\sqrt{E_{decay}+b}} - cE_{decay}. \tag{3.13}$$

This approach, previously performed by former ANU students [11, 12, 54], allows for a simultaneous fit, using all available calibration points, without the need to consider a reference energy. The implementation of this approach is demonstrated in Sec. 5.5.

The accurate determination of the centroids, C_{fwd} and C_{rev}, is also crucial. The centroid can be obtained using the centre of gravity method:

$$C = \frac{\Sigma_{i=a}^{i=b} c_i \cdot w_i}{\Sigma_{i=a}^{i=b} w_i}, \tag{3.14}$$

where w_i is the number of counts in channel c_i over the summation range $[a,\ b]$. We considered two approaches to determine the centroid. The first, termed the "physical" method, calculates the centroid from the net spectrum after performing background subtraction as shown in Eq. 3.6. The second, "mathematical" method, follows the procedure from Ref. [53]. It first calculates the centroids of all peak and background-gated spectra, $C^m_{p|p}$, $C^m_{bg|p}$, $C^m_{p|bg}$ and $C^m_{bg|bg}$, and then computes the centre of the background-subtracted spectrum $C^t_{p|p}$ as

$$C^t_{p|p} = \frac{n^m_{p|p}C^m_{p|p} - n^m_{p|bg}C^m_{p|bg} - n^m_{bg|p}C^m_{bg|p} + n^m_{bg|bg}C^m_{bg|bg}}{n^m_{p|p} - n^m_{p|bg} - n^m_{bg|p} + n^m_{bg|gb}}, \tag{3.15}$$

where $n^m_{p|p}$, $n^m_{p|bg}$, $n^m_{bg|p}$ and $n^m_{bg|bg}$ are the number of counts in each distribution that are normalised with respect to the $p|p^m$ gate area. Both methods are equivalent and should yield consistent results, as demonstrated through a simulation using

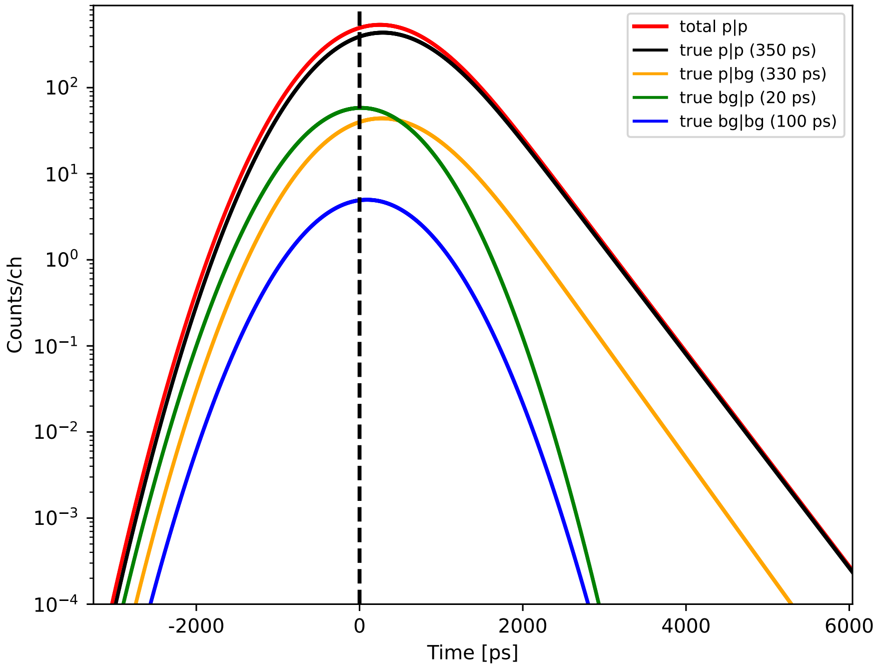

Figure 3.7: Theoretical investigation using time-difference spectra to compare centroid determination of $p|p^t$ with a 350 ps lifetime via "physical" and "mathematical" methods. Spectra with gates $p|p^t$, $p|bg^t$, $bg|p^t$ and $bg|bg^t$ are shown in black, orange, green and blue, respectively, and $p|p^m$, the sum of all gates, is red.

exponential-convoluted Gaussian curves, illustrated in Fig. 3.7. In this study, each gate, $p|p^t$, $p|bg^t$, $bg|p^t$ and $bg|bg^t$, is assumed to have arbitrary lifetimes of 350 ps, 330 ps, 20 ps and 100 ps, respectively. The centroid of the prompt peak is set to be at $\Delta T = 0$ ps. The "measured" spectra are then calculated using Eqs. 3.4-3.6. Consequently, the "physical" and "mathematical" methods both yield $C = 349.5$ ps, indicating agreement. Performing both methods serves as a check on the data analysis and can also give an indication of uncertainties in the data analysis procedures. An experimental comparison of the two approaches is presented in Sec. 5.5.

Chapter 4

Experimental details

In August and September 2023, our research group conducted direct-timing lifetime measurements of the 2_1^+ states in $^{180-186}$Pt using a combination of six Compton-suppressed LaBr$_3$(Ce) detectors alongside three Compton-suppressed HPGe (High Purity Germanium) detectors within the CAESAR array at the Australian National University Heavy Ion Accelerator Facility (ANU-HIAF). This experiment was performed prior to my arrival, but the data were only preliminarily analysed. The isotopes examined in this study were populated via heavy-ion fusion reactions, specifically ^{156}Gd(^{28,30}Si,4n)^{180,182}Pt and ^{172,174}Yb(^{16}O,4n)^{184,186}Pt. This chapter provides information regarding the experimental setup used in this study.

4.1 Heavy-ion fusion reactions

While there are many methods, such as Coulomb excitation, transfer reactions and neutron capture reactions, that can be used to produce excited nuclei, heavy-ion fusion reactions [55, 56] are the most widely used technique for populating high-spin states in neutron-deficient nuclei. The platinum isotopes for this study were produced via this method using beams from the 14UD Pelletron accelerator at the Australian National University Heavy Ion Accelerator Facility (ANU-HIAF). Beams of ^{28,30}Si or ^{16}O ions were impinged onto targets of ^{156}Gd or ^{172,174}Yb to produce ^{180,182}Pt and ^{184,186}Pt, respectively.

When an incident ion beam has sufficient energy to overcome the repulsive Coulomb barrier between two projectile and target nuclei, they can fuse together, creating a hot and spinning compound nucleus with high angular momentum and at high excitation energy where the level density is extremely high (Fig. 4.1). This hot compound nucleus cools by evaporating light particles, including neutrons, protons and alpha particles; for the neutron-rich systems studied here, neutron emission is favoured. The spin of the nucleus is initially aligned perpendicular to the direction of the beam axis, though this alignment is not a central aspect of the present analysis.

Toward the end of the cooling process, when the excitation energy drops below

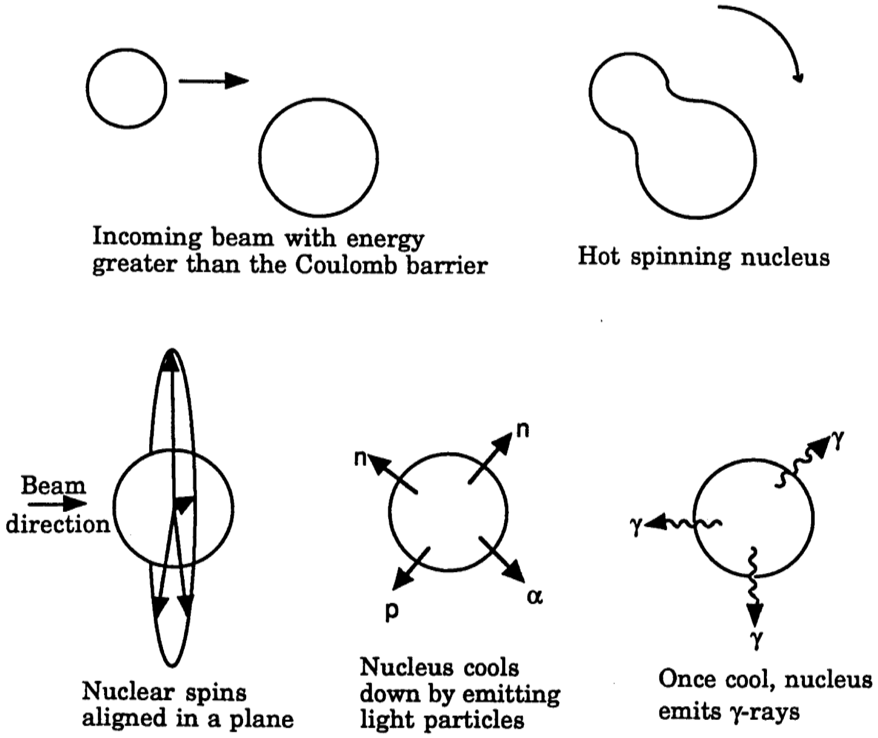

Figure 4.1: Schematic picture of a heavy-ion fusion reaction. Figure taken from Ref. [41].

the neutron binding energy (∼8 MeV), the residual nucleus becomes particle-bound. Thereafter, the nucleus de-excites primarily through γ-ray emission. At this stage, the nucleus is still excited well above the yrast states. The initial de-excitation proceeds through a series of statistical electric dipole (E1) transitions, which cools the nucleus and carries away little angular momentum. As the nucleus cools towards the yrast line, the nucleus then loses further energy and angular momentum by cascades of stretched E2 transitions as the population is channelled along rotational bands in the continuum. This process continues until the nucleus reaches a region of low level density along/near the yrast line, where it decays by the emission of discrete transitions between well separated states. Ultimately, the population is channelled into the ground-state band.

4.2 Cross section calculations

The statistical model program PACE2 [57] was used to calculate production cross sections for the heavy-ion fusion reactions used in this work. Beam energies are selected to achieve the maximum cross section of the nuclei of interest. The calculation results for ^{156}Gd(^{28,30}Si,4n)^{180,182}Pt and ^{172,174}Yb(^{16}O,4n)^{184,186}Pt reactions are shown in Figs. 4.2-4.5, with vertical dotted lines representing the chosen beam energies. Note that the beam loses energy in the target so the cross section is integrated to lower energies depending on the target thickness.

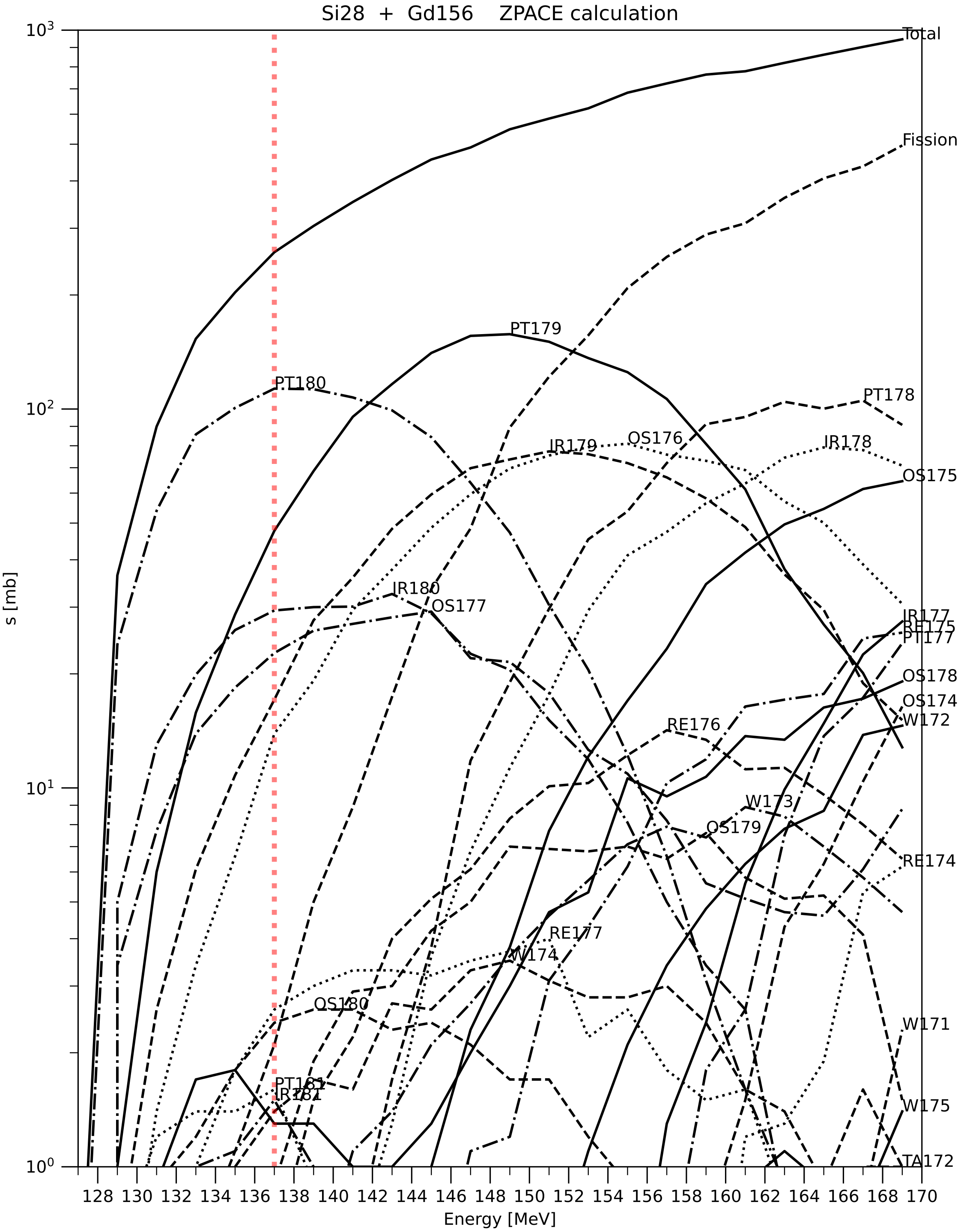

Figure 4.2: Cross section calculation for the ^{28}Si+^{156}Gd reaction chosen to make ^{180}Pt, using the statistical model program PACE2.

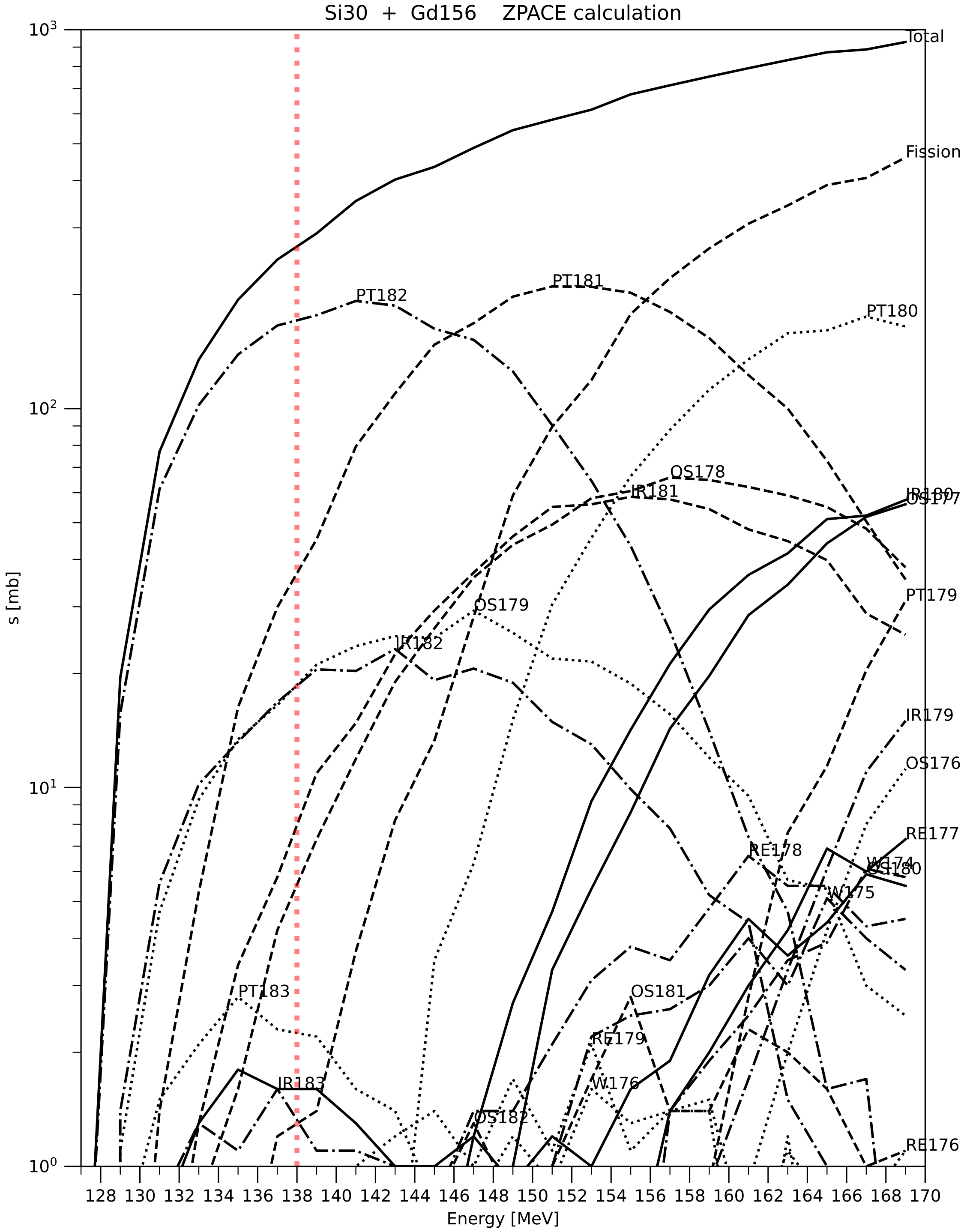

Figure 4.3: Cross section calculation for the ^{30}Si+^{156}Gd reaction chosen to make ^{182}Pt, using the statistical model program PACE2.

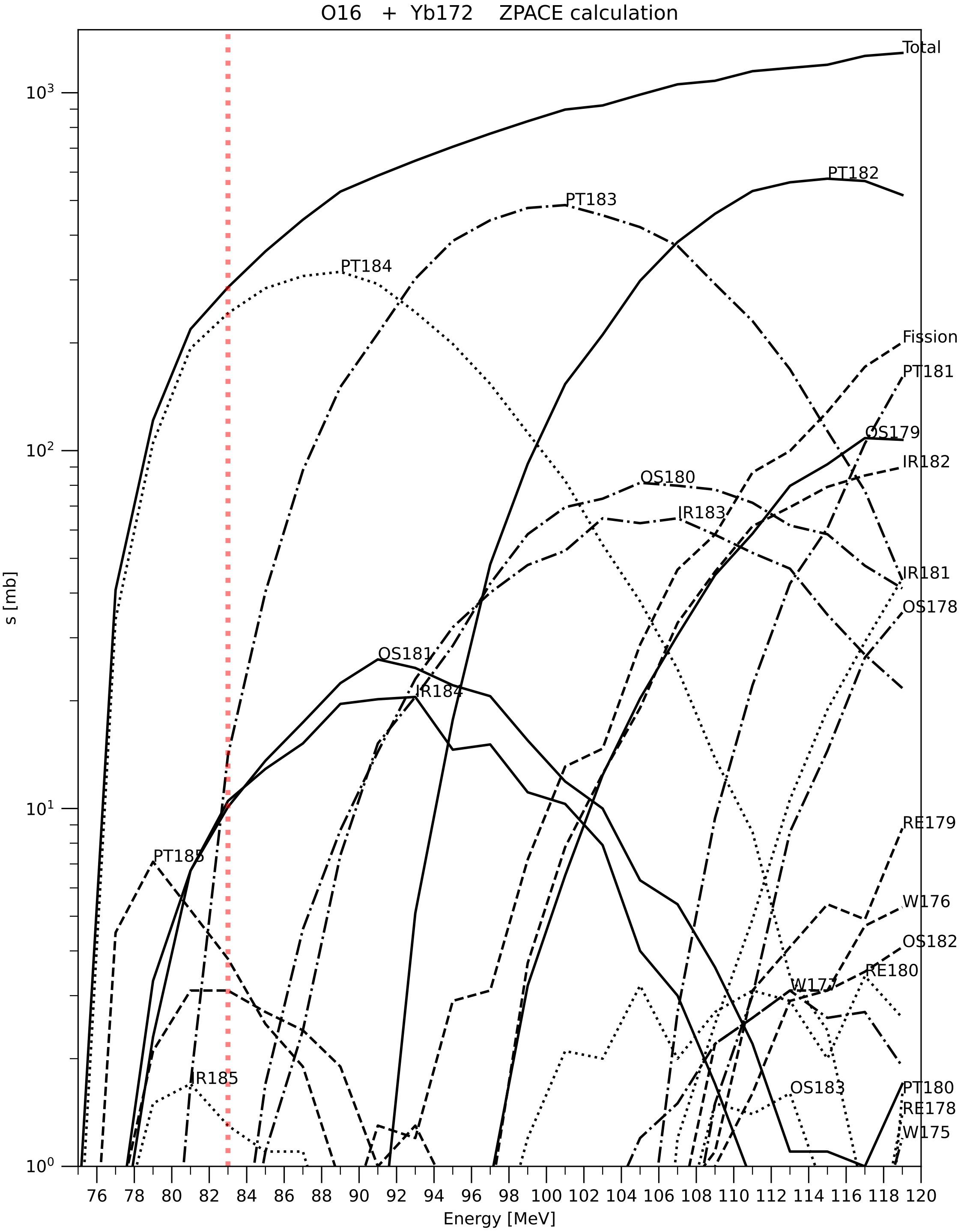

Figure 4.4: Cross section calculation for the ^{16}O+^{172}Yb reaction chosen to make ^{184}Pt, using the statistical model program PACE2.

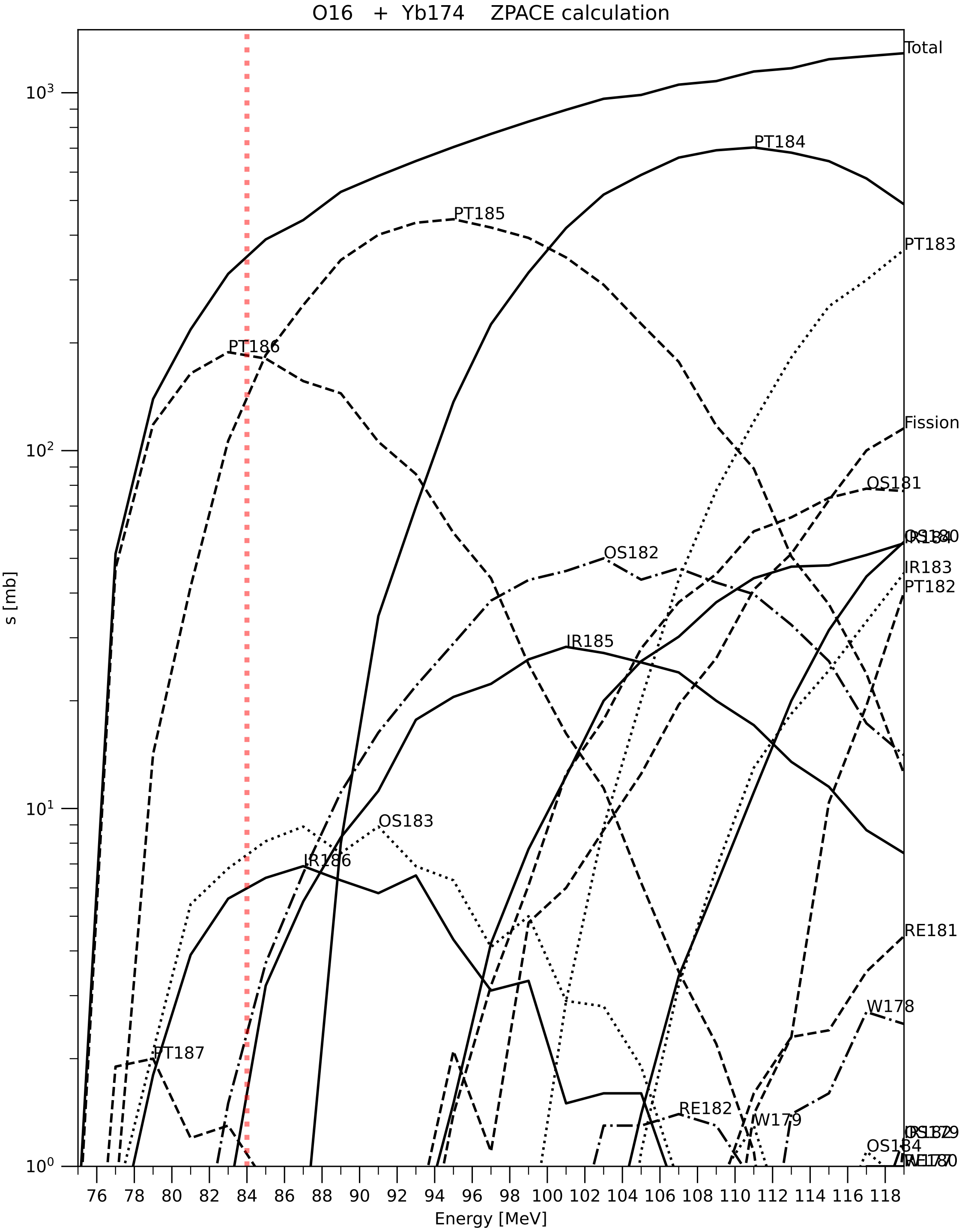

Figure 4.5: Cross section calculation for the ^{16}O+^{174}Yb reaction chosen to make ^{186}Pt, using the statistical model program PACE2.

4.3 The CAESAR γ-ray detector array

In this experiment, the CAESAR array, comprising six Compton-suppressed $LaBr_3$(Ce) detectors in conjunction with three Compton-suppressed HPGe detectors, was used. A schematic diagram of CAESAR is shown in Fig. 4.6. The $LaBr_3$(Ce) detectors offer a higher time resolution compared to HPGe detectors, approximately a few hundred picoseconds, although with a lower energy resolution than HPGe detectors, around 10 keV. In contrast, the HPGe detectors provide higher energy resolution, approximately 2 keV at 1.3 MeV, yet exhibit lower time resolution, in the range of approximately 10-20 ns. The combination of these detectors allows for precise measurements of both lifetimes and γ-ray energies.

4.3.1 $LaBr_3$(Ce) detectors

In scintillation detectors, the interaction with a γ-ray generates low-energy photons. $LaBr_3$(Ce) offers superior timing and energy resolution in comparison to NaI(Tl)

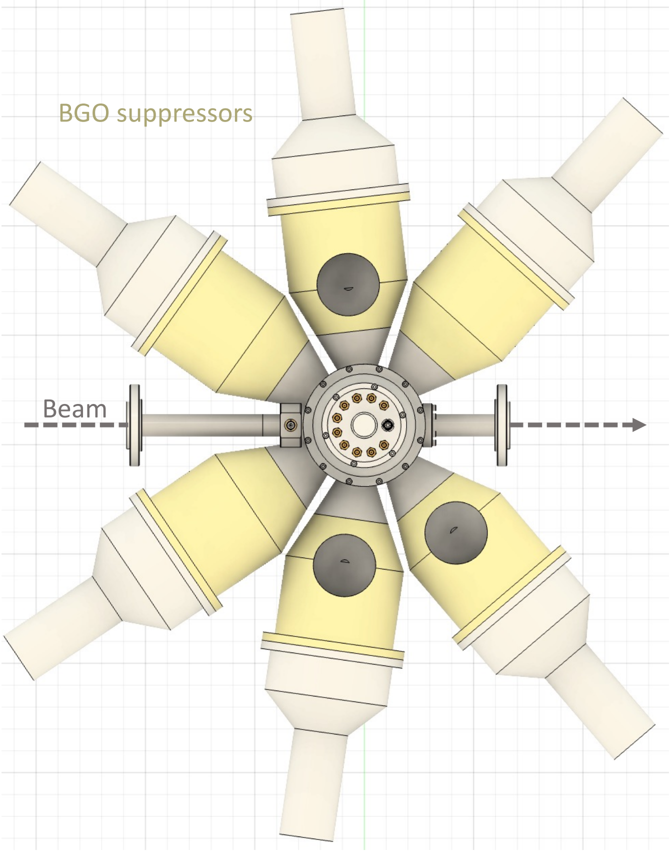

Figure 4.6: Schematic diagram of the CAESAR array with six Compton-suppressors where the $LaBr_3$ detectors were inserted. Three HPGe detectors, not pictured in the diagram, are positioned roughly in the horizontal plane along the beam axis, perpendicular to the page.

scintillating detectors thanks to its substantially higher light output, which is more than twice that of NaI(Tl), and the fact that the principal decay time for LaBr$_3$(Ce) is approximately 16 ns, which is more than ten times faster than NaI(Tl) [58]. The scintillation light thus generated is converted into a measurable electrical signal by a photomultiplier tube (PMT). Within the PMT, photons strike a photocathode, releasing electrons through the photoelectric effect, which are subsequently accelerated and amplified across a series of dynodes to yield a pulse. In this study, BrilLanCe380 LaBr$_3$(Ce) crystals with a diameter of 38 mm and a length of 51 mm, equipped with R2083 *Fast* PMTs, as depicted in Fig. 4.7, were employed [59].

4.3.2 HPGe detectors

The HPGe detector is a type of semiconductor detector that is widely used in gamma-ray spectroscopy for its excellent energy resolution, approximately 0.15% at 1.33 MeV [60]. As radiation passes through the semiconductor, it generates electron-hole pairs that are subsequently collected by an applied electric field. The

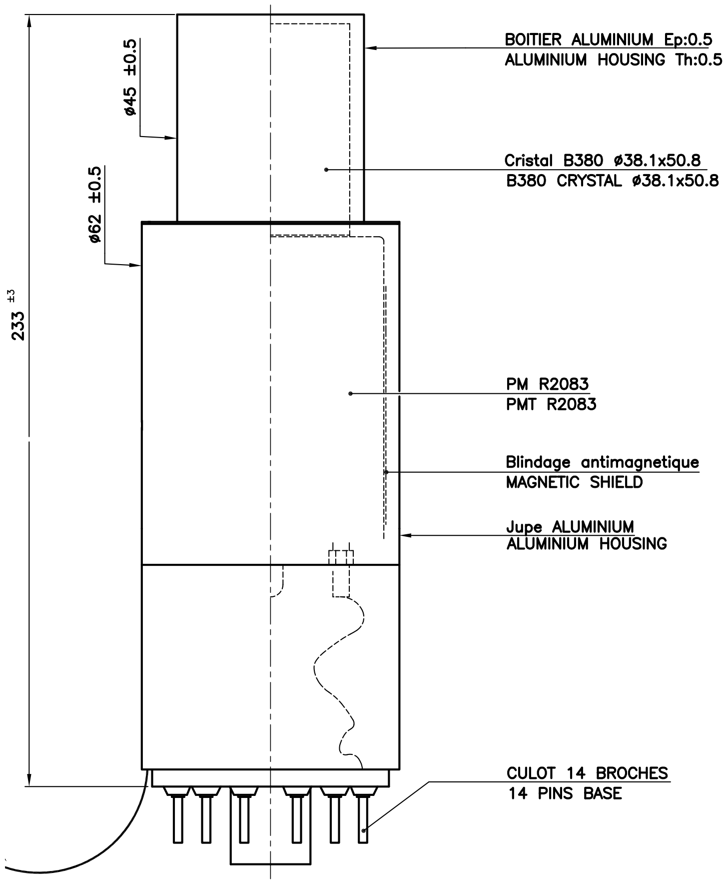

Figure 4.7: Schematic diagram of the configuration of the LaBr$_3$(Ce) detector and PMT utilised in this study. Figure taken from product manuals provided with the detector [59].

comparatively low average energy required to generate an electron-hole pair in semiconductors (2.96 eV at 77K for Ge [60]), roughly 10 times lower than in gases, results in a higher extent of ionisation per unit of energy, thereby providing enhanced energy resolution. Germanium detectors generally require cooling to low temperatures because their narrower band gap at ambient temperatures would result in high leakage currents, degrading performance. Recent improvements in semiconductor growth technology have enabled the production of extremely high purity germanium, with impurity levels below 10^{10} atoms/cm^3 [60]. This type of detector benefits from not requiring constant low temperatures; cooling is needed only when a high voltage is applied.

4.3.3 Compton suppressors

Compton scattering events in the γ-ray spectrum give rise to a significant background that can obscure weak γ-ray signals. This background can be mitigated by surrounding the primary detector with another detector that is used to detect γ-ray Compton scattering both within the same detector and from other primary detectors. Events in which coincident γ rays are detected in both the primary detector and the suppression shield are vetoed.

The Compton suppressors in the CAESAR array are made of Bismuth Germanate (BGO) and are designed so that the HPGe/LaBr$_3$ detectors enter from the side [61]. This configuration improves the peak-to-total ratio for the 662 keV γ ray from a ^{137}Cs source from about 32% to 66% [62]. The improvement is especially significant for $\gamma - \gamma$ coincidence measurements, as the proportion of useful peak-peak coincidence events scales with the square of this ratio, resulting in a more than four-fold increase in the effective coincidence data rate.

4.3.4 Digital DAQ

This study employed two XIA Digital Gamma Finder Pixie-16 boards [63], a 14-bit 100 MHz (10 ns) board for the HPGe detectors and a 12-bit 500 MHz (2 ns) board for the LaBr$_3$ detectors and suppressors. In the XIA system, signals were digitised using integrated digital processing to determine energies and event timings for each γ-ray detector and suppressor. Energies and times for all signals were extracted using the onboard FPGA (Field Programmable Gate Array). The trigger condition required a coincidence between any two detectors within a 1 μs time window. This included any combination of two HPGe detectors, two LaBr$_3$ detectors, or one HPGe and one LaBr$_3$ detector.

Energy measurement. A widely used algorithm to extract energies from a digital waveform is the trapezoid filter method [64], that provides superior energy resolution compared to other filtering methods when signal rise times vary because of charge trapping or differences in radiation interaction position within large volume detectors [65, 66]. Signals after pre-amplifiers typically feature a rapid rise time and a long exponential decay towards zero, as shown in Fig. 4.8, where the energy deposited in the detector is proportional to the area beneath this curve [67]. The filter algorithm is described in the product reference manual [63] as

$$\mathrm{F}_i = \sum_{j=i-(L-1)}^{i} \mathrm{V}_j - \sum_{j=i-(2L+G-1)}^{i-(L+G)} \mathrm{V}_j, \tag{4.1}$$

where the filter has user-defined parameters, a length of L and gap G (this is a triangular filter when G=0). V_j represents the input digitised signal at the j-th sample, and F_i is the filtered value at the i-th sample. Figure 4.8, taken from Ref. [63], shows the filtering result for $L = 1\,\mu s$ and G=$0.4\,\mu s$, with a rise time of L, a flat top of G and a basewidth of $2L + G$. The energy of the event is determined by measuring the height of the trapezoid above the baseline, a value that the Pixie-16 obtains from channel $L + G - 1$ following the event trigger. One important feature of this digital trapezoid filter is its sharp trailing edge [63], unlike analog filtered

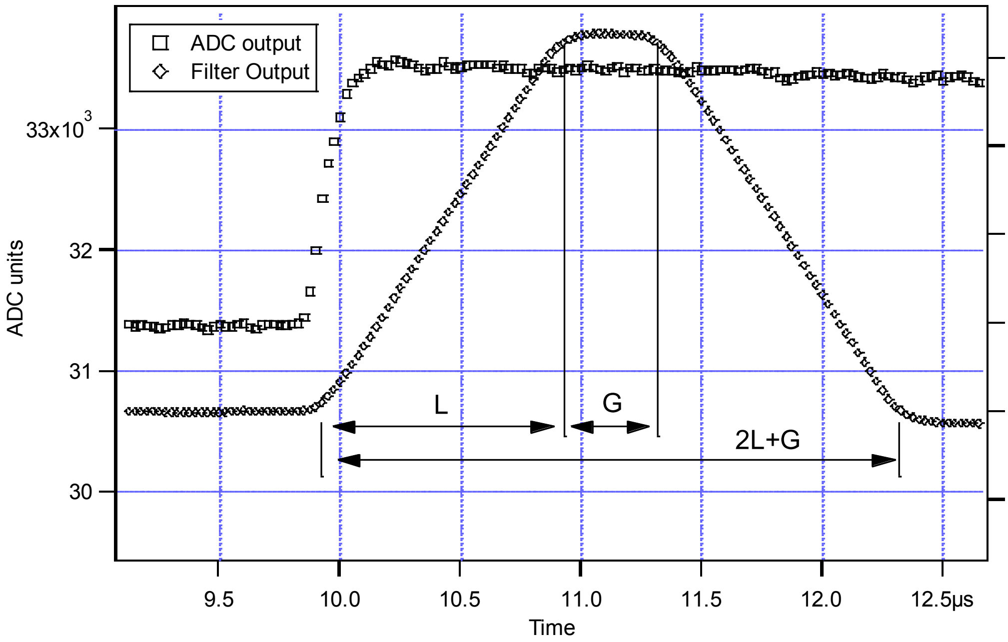

Figure 4.8: Trapezoidal filtering of a preamplifier output signal, focusing on the region near the step up in the signal, and using filter parameters $L = 1\,\mu s$ and $G = 0.4\,\mu s$. Figure taken from Ref. [63].

pulses which may have tails persisting for up to 40% of the rise time because of the limited bandwidth of the analog filter. This sharp edge provides digital filters with the advantage of being able to handle higher throughput without pileup.

Timing measurement. In addition to energy filtering, the Pixie-16 module employs a fast trapezoid filter to determine waveform timing. This fast shaping leads to a reduced rise time compared to the energy trapezoid, offering a more accurate timing value, but sacrificing energy resolution. Within the 100 MHz module, the filtering algorithm is [63]

$$\mathrm{FF}_i = \sum_{j=i-(FL-1)}^{i} \mathrm{Trace}_j - \sum_{j=i-(2FL+FG-1)}^{i-(FL+FG)} \mathrm{Trace}_j, \tag{4.2}$$

where FL denotes a fast length and FG is a fast gap to be set for the digital trapezoidal filter. Trace_j indicates the digitised waveform value at the j-th sample, while FF_i represents the fast filtered value at the i-th sample. To implement a CFD algorithm, the attenuated signal is subtracted from the delayed signal (see Sec. 3.1 for theoretical details) such that [63]

$$\mathrm{CFD}_{i+D} = \left(1 - \frac{S}{8}\right) \mathrm{FF}_{i+D} - \mathrm{FF}_i, \tag{4.3}$$

where D denotes the delay time, S is the attenuation scaling factor ($0 \leq S \leq 7$) and $\mathrm{FF}[i]$ is the fast-filtered trapezoid. The zero-crossing time is then interpolated from when $\mathrm{CFD}_i \geq 0$ and $\mathrm{CFD}_{i+1} \leq 0$. When the CFD is not applied, the time is captured when the fast filtered trapezoid signal crosses a user-defined threshold. If several fast triggers happen during the conversion of the energy in the slow trigger, these events are identified as pileup and may be filtered out.

The 500 MHz module implements a similar timing determination algorithm; for more detailed information, refer to Ref. [63].

Chapter 5

Data analysis and results

5.1 Detector calibration

5.1.1 Energy calibration

The energy calibrations of the $\mathrm{LaBr_3}$ and HPGe detectors were performed using the well-known γ-ray energies from a ^{152}Eu source. However, this ^{152}Eu measurement was conducted nearly one week after the initial Pt experiment. Furthermore, an energy shift was observed during the Pt measurements, as shown in Fig. 5.1.

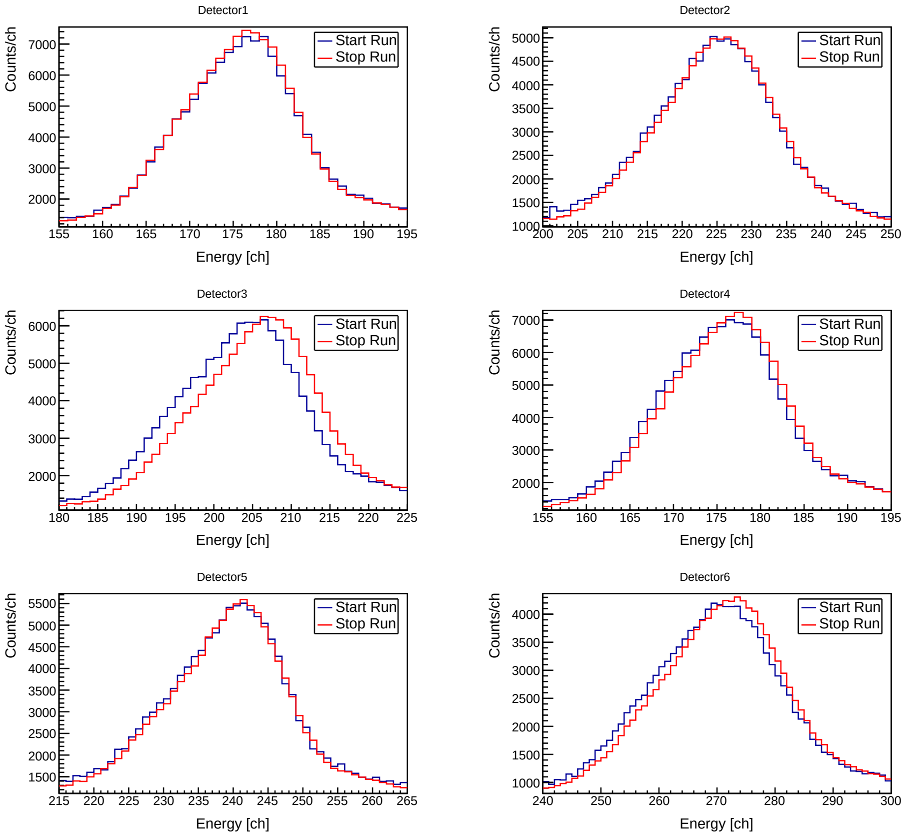

Figure 5.1: Gain shift in the $\mathrm{LaBr_3}$ detectors during the in-beam measurement of ^{182}Pt. The plot shows the $4_1^+ \rightarrow 2_1^+$ transition from the first and the last experimental run, which were separated by approximately two days.

Therefore, a final calibration was carried out using γ-ray transitions from the platinum datasets. The lower γ-ray energies of these platinum nuclei are well-documented [4–7], and the goal of the current experiments was to measure lifetimes, not conduct general spectroscopy, thus this calibration approach was not a limitation. Figures 5.2-5.5 show the final energy spectra for LaBr_3 and HPGe detectors.

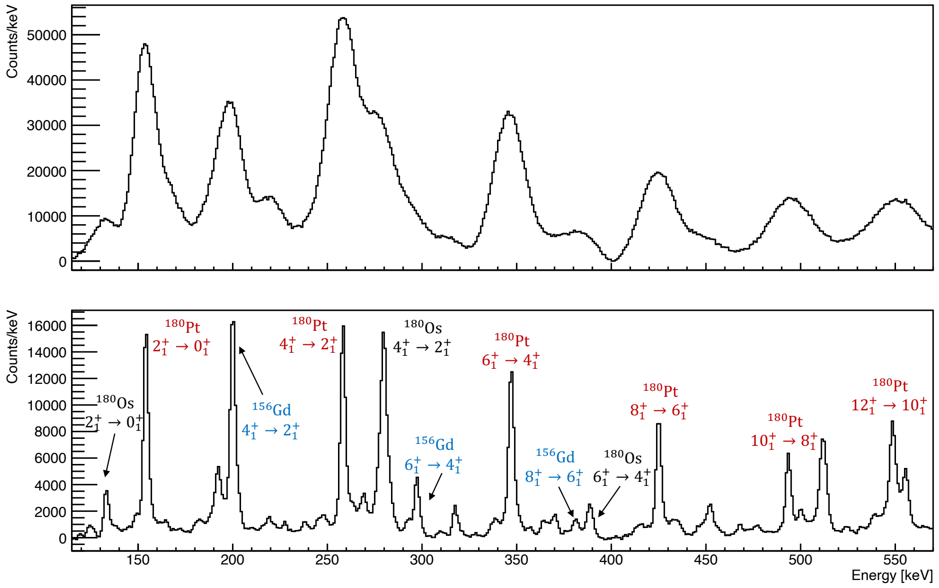

Figure 5.2: Energy spectrum for the sum of all six LaBr_3 detectors (top) and three HPGe detectors (bottom), projected from the full coincidence data set, for the ^{180}Pt measurement

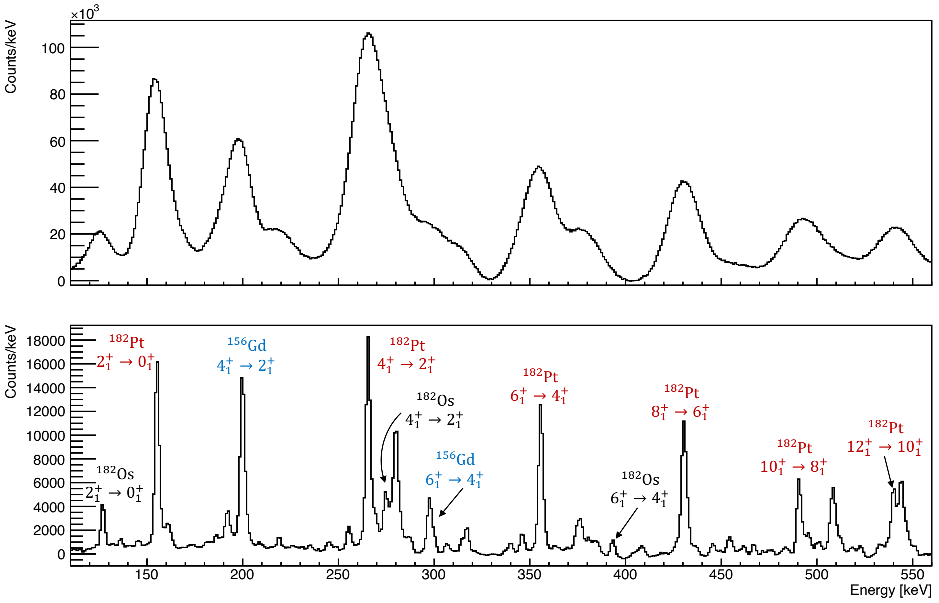

Figure 5.3: Energy spectrum for the sum of all six LaBr_3 detectors (top) and three HPGe detectors (bottom), projected from the full coincidence data set, for the ^{182}Pt measurement

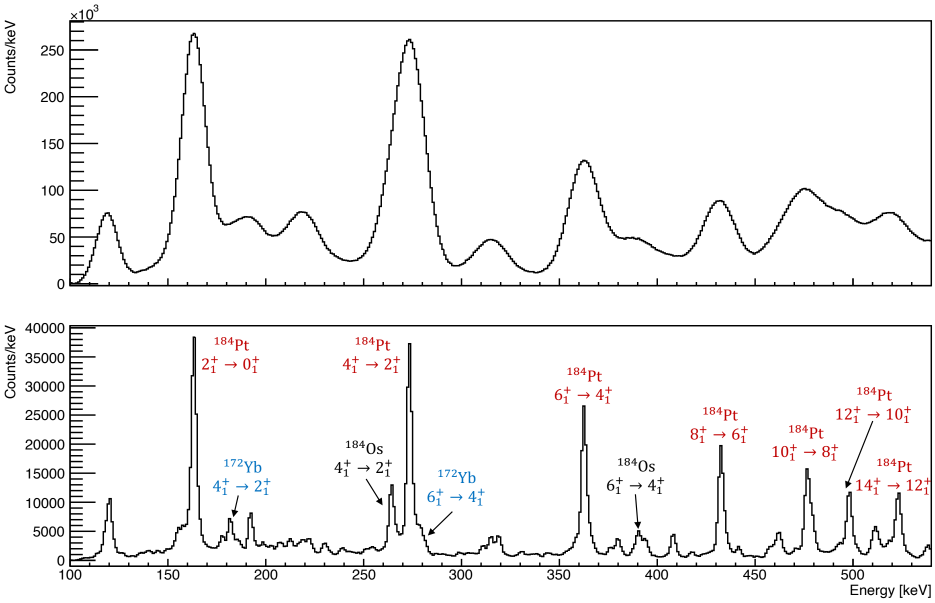

Figure 5.4: Energy spectrum for the sum of all six $\mathrm{LaBr_3}$ detectors (top) and three HPGe detectors (bottom), projected from the full coincidence data set, for the ^{184}Pt measurement

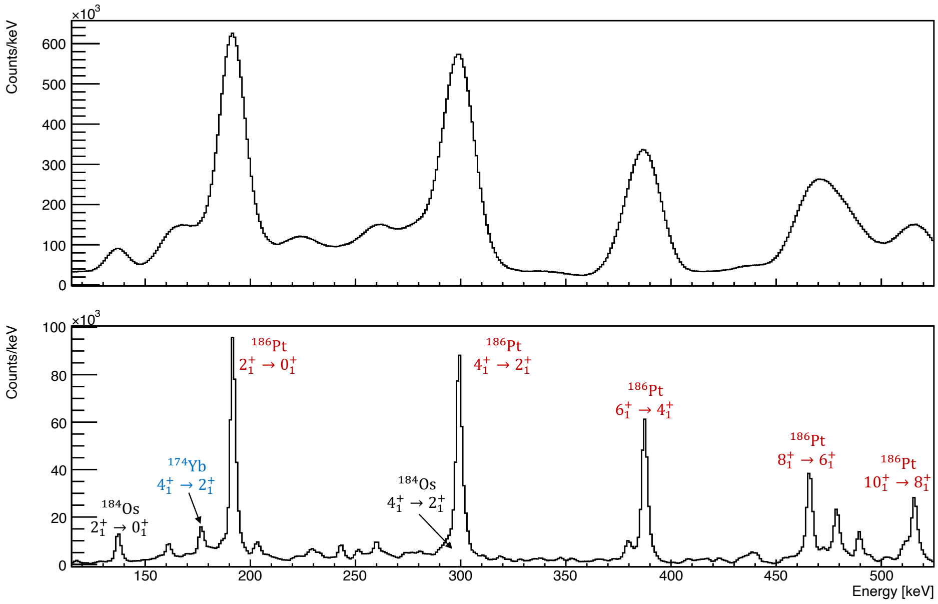

Figure 5.5: Energy spectrum for the sum of all six $\mathrm{LaBr_3}$ detectors (top) and three HPGe detectors (bottom), projected from the full coincidence data set, for the ^{186}Pt measurement

5.1.2 Time alignment

The time alignment is performed to correct for time variations between detector channels. These differences are caused by several physical and electronic factors, including location of γ-ray interaction in the detector crystal, time response of detector and signal wire lengths. For any pair of detectors, a prompt peak, corresponding to coincidences between simultaneously emitted γ rays, will produce a distinct peak in their relative time-difference spectrum. The time alignment procedure involves shifting the raw time of each detector so that these prompt-coincidence peaks are aligned at t=0 for all detector combinations, as shown in Fig. 5.6.

5.1.3 Comparison between LaBr$_3$ and HPGe detectors

As mentioned in Sec. 4.3, LaBr$_3$ and HPGe detectors possess complementary strengths. LaBr$_3$ detectors offer high time resolution but lower energy resolution, whereas HPGe detectors provide superior energy resolution but with lower time resolution. Figure 5.7, which shows a projection of the ^{186}Pt $\gamma-\gamma$ matrix in the region of the $4_1^+ \rightarrow 2_1^+$ and $2_1^+ \rightarrow 0_1^+$ transitions, and the "singles" γ-ray spectra

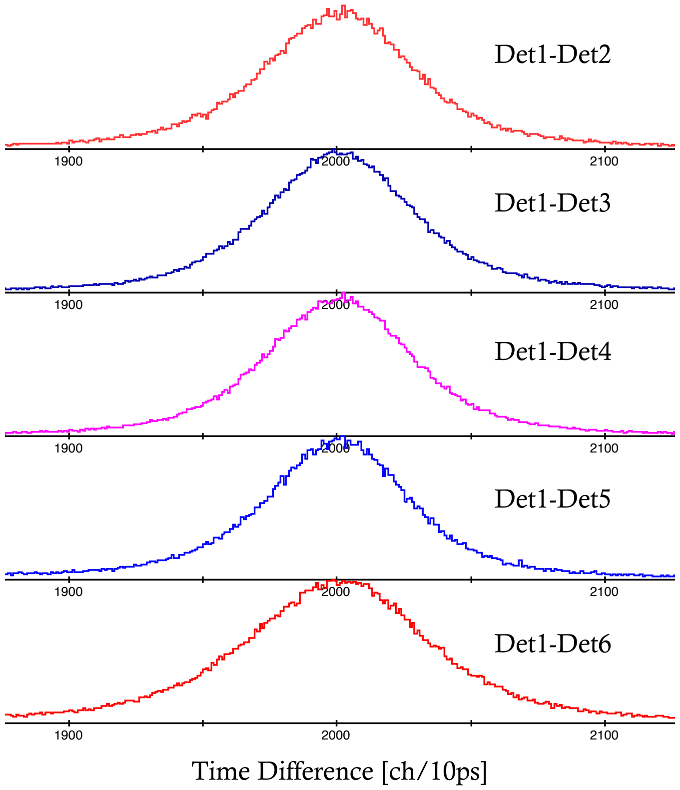

Figure 5.6: Aligned time-difference spectra between LaBr$_3$ detectors, using data from the ^{182}Pt measurement. The alignment aligns the prompt-coincidence peak to be centred at channel 2000, defining the t=0 position.

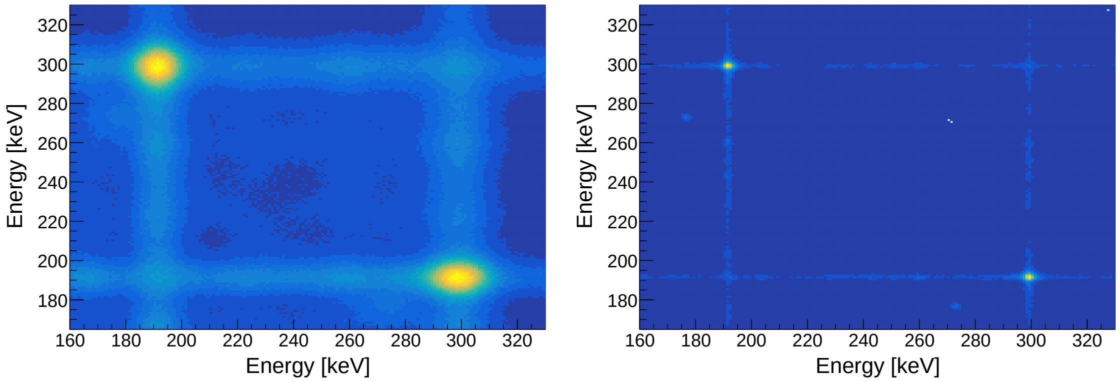

Figure 5.7: Comparison of $\gamma - \gamma$ coincidence matrices for ^{186}Pt measured with the $\mathrm{LaBr_3}$ array (left) and the HPGe array (right). The superior energy resolution of the HPGe detectors is evident.

shown on the left in Fig. 5.8, clearly demonstrate the superior energy resolution of the HPGe detectors. Figure 5.8 shows the $\mathrm{LaBr_3}$ and HPGe time-difference spectra in the right-hand panel. These data clearly illustrate the superior time resolution of $\mathrm{LaBr_3}$ detectors, noting that the unit for the $\mathrm{LaBr_3}$ spectrum is 10 ps per channel, while it is 1 ns per channel for the HPGe spectrum.

Some of our time-difference spectra displayed “wings” at lower count levels, as shown in Fig. 5.9. The comparative absence of these wings in radioactive source data suggests that these might be attributed to neutrons, beam hitting upstream or downstream of the target, or possibly other experimental setup such as cable issues. In the following analysis, the use of data in the region of these wings was avoided.

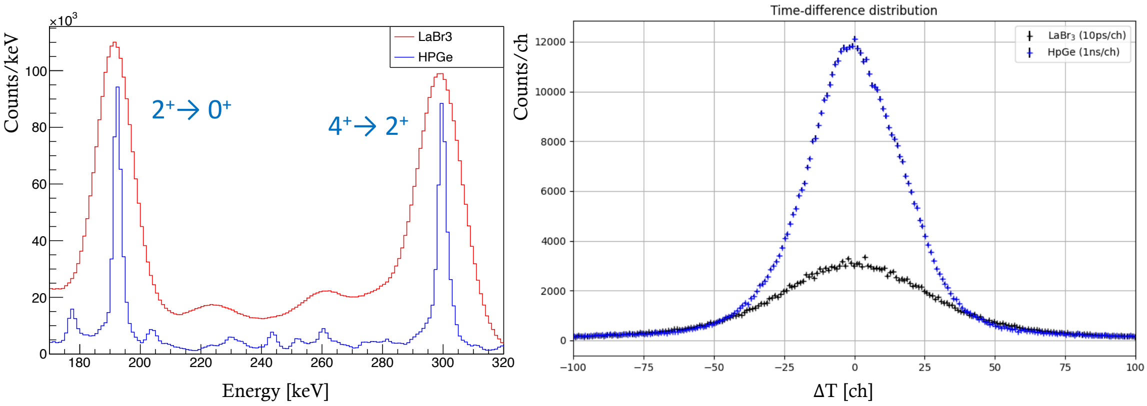

Figure 5.8: Comparison of the gamma-ray energy spectra for the $4_1^+ \rightarrow 2_1^+$ and $2_1^+ \rightarrow 0_1^+$ transitions in ^{186}Pt (left) and the time-difference spectra between $\mathrm{LaBr_3}$ detector pairs and HPGe detector pairs (right). Note that the unit for the $\mathrm{LaBr_3}$ time spectrum is 10 ps per channel, while it is 1 ns per channel for the HPGe time spectrum.

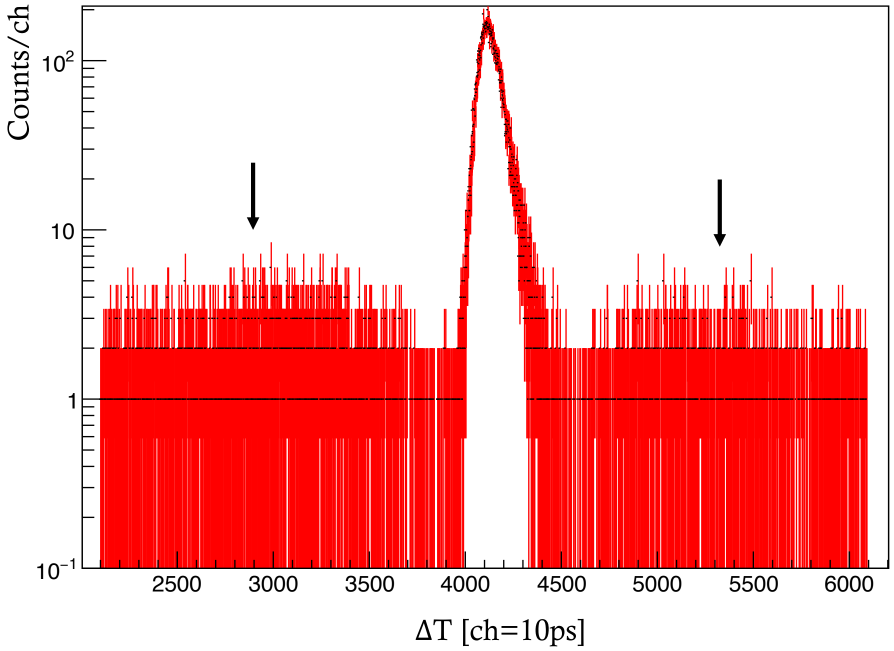

Figure 5.9: Raw peak-to-peak time-difference spectrum in ^{184}Pt, showing two wings on both sides indicated by arrows. These wings were avoided in the following analysis. $\Delta T = 0$ corresponds to 4096 ch.

5.2 Prompt Response Difference (PRD)

The PRD curve introduced in Sec. 3.3.3 was determined for the present setup using a ^{152}Eu source with precisely known transition energies and level lifetimes. Ten cascades, shown coloured in Fig. 5.10, together with two cascades initiated by the 40-keV K-X-ray of ^{152}Sm (emitted during β decay) feeding to the 1530-keV state and ending in the 1408- and 964-keV γ rays, were used as fit points for Eq. 3.13 to create the 3D PRD surface. All values used in this analysis are summarised in Tab. 5.1.

As outlined in Sec. 5.3, accurate lifetime extraction requires appropriate selection of the peak gate $p|p^m$ and background gates $p|bg^m$, $bg|p^m$ and $bg|bg^m$. Among these, the choice of the $p|p^m$ region is particularly critical; selecting a region that is too narrow results in poor statistics, while a region that is too wide may include background contamination from nearby transitions or Compton events. To optimise the $p|p^m$ selection, the other background regions were held fixed and the variation in resulting PRD values was examined by changing the $p|p^m$ window size. Figure 5.11 illustrates how the $p|p^m$ window size affects the PRD values in the 586 keV → 344 keV cascade, indicating that it is reasonable to select a window range where the PRD values exhibit relative stability; this range is highlighted in blue. Similar approaches were taken for all of the transition pairs.

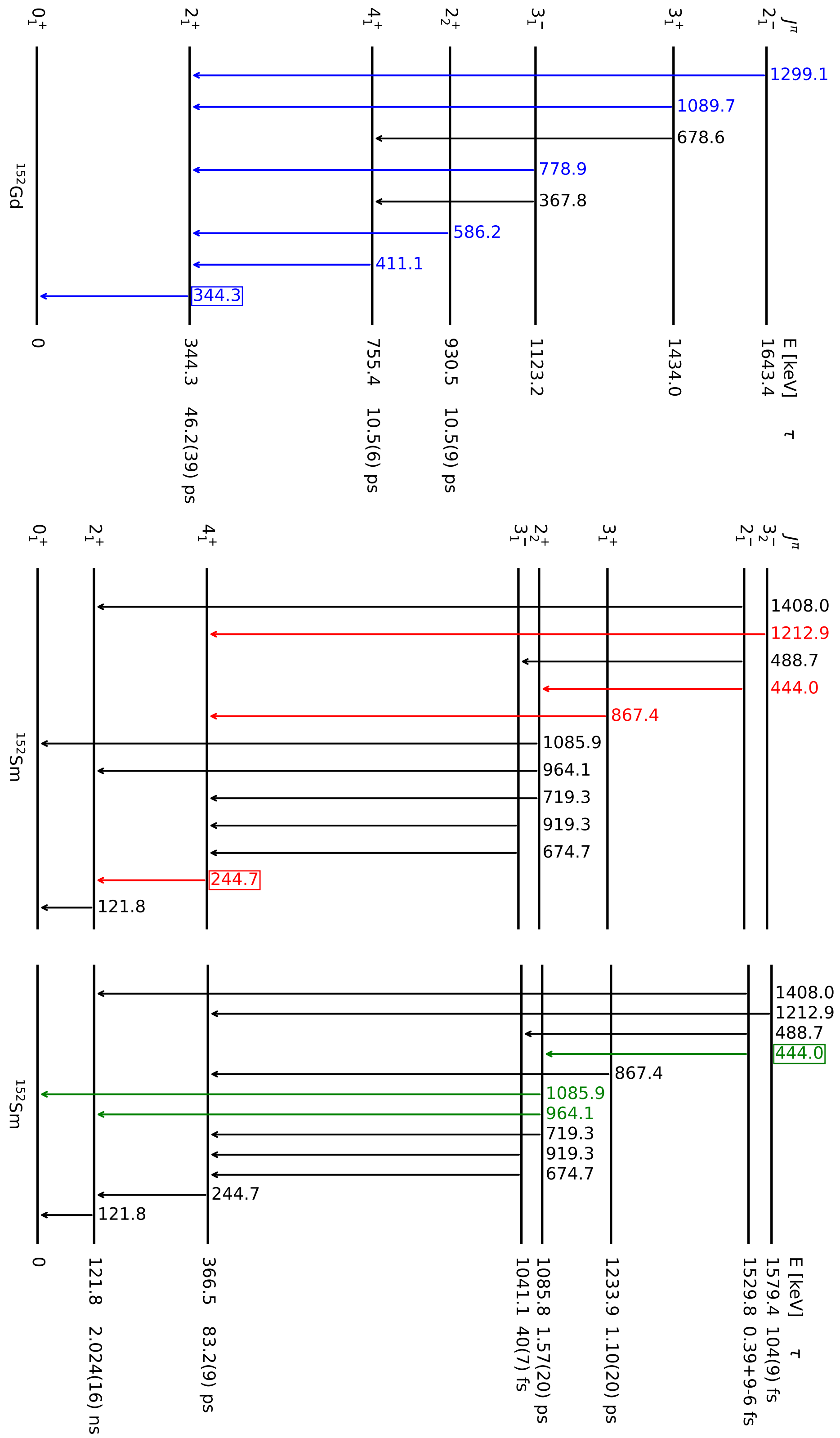

Figure 5.10: Energy level diagram for the ^{152}Eu source [68] with the γ-ray cascades used for the PRD calibration highlighted. The panels show cascades that: (top) feed into the 344.3-keV transition; (middle) feed into the 244.7-keV transition; and (bottom) are fed by the 444.0-keV transition. The 40-keV K-X-ray of ^{152}Sm (emitted during β decay) feeding to the 1530-keV state is not shown.

Table 5.1: Energies and lifetimes values used to construct the 3D PRD surface from ^{152}Eu cascades [68], including the PRD values obtained for each cascade. The 40-keV feeding energy corresponds to the ^{152}Sm K-X-ray serving as the start signal feeding the 1530-keV state.

Feed Energy [keV]	Decay Energy [keV]	Total Lifetime [ps]	PRD [ps]
1299.1	344.3	46.2(39)	43.0±9.5
1089.7	344.3	46.2(39)	16.7±17.9
778.9	344.3	46.2(39)	13.3±8.0
586.2	344.3	46.2(39)	9.81±11.97
411.1	344.3	46.2(39)	0.0833±8.5746
1212.9	244.7	83.2(9)	12.9±7.6
867.4	244.7	83.2(9)	-1.48±3.22
444.0	244.7	84.8(9)	-3.66±16.06
444.0	1085.9	1.57(20)	-29.2±8.8
444.0	964.1	1.57(20)	-19.3±11.4
40	1408.0	∼0	203±17
40	964.1	1.57(20)	215±19

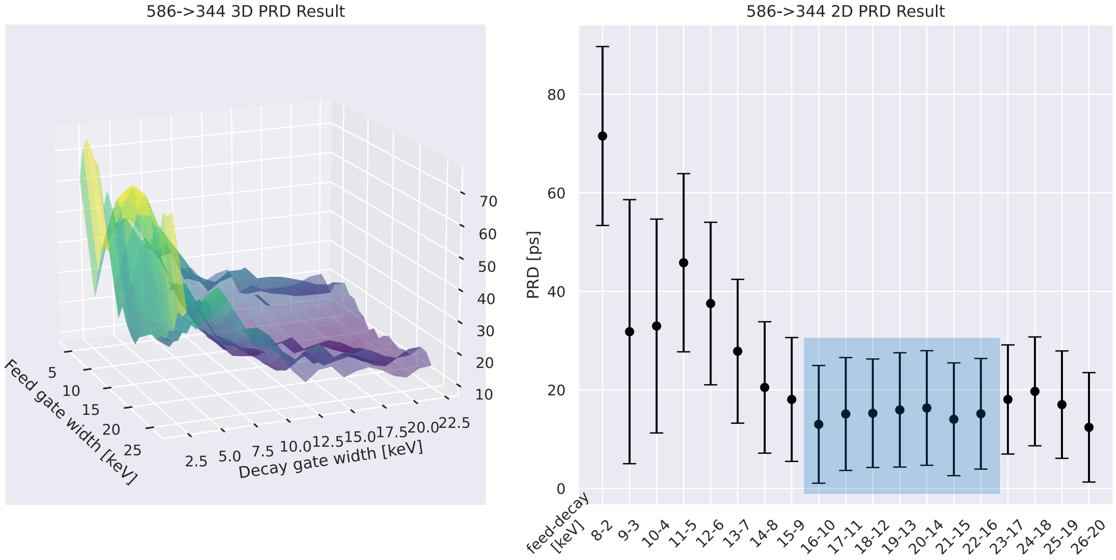

Figure 5.11: The extracted PRD values of the 586 keV → 344 keV cascade and its dependence on the $p|p^m$ gate width around the centre of the peak-to-peak gate, shown in 3D (left) and 2D (right) plots. Other background regions were held fixed. The optimal gate width for the final analysis is selected from the stable plateau region of this curve highlighted in blue.

After all of the cascades were evaluated, PRD values were determined for each and are listed in Tab. 5.1. The PRD 3D fitting was carried out to these PRD values, as illustrated in Fig. 5.12. The fitted parameters in Eq. 3.13 were found to be

$$\begin{cases} a = 1688.8 \\ b = -17.951 \\ c = 0.086256 \end{cases} \tag{5.1}$$

Uncertainties for the PRD values are assigned based on the residuals, not on uncertainty estimates of these fitted parameters. Figure 5.13 shows the PRD 2D projection line at $E_{ref} = 344$ keV and the thirteen experimental data points shifted using Eq. 3.10-3.12 and the fitted parameters from Eq. 5.1, demonstrating that our straightforward method well aligns with the data points. The root-mean-square deviation relative to the slice line was calculated to be 7.21 ps, as displayed in the bottom of Fig. 5.13, this was adopted as the PRD uncertainty.

5.3 Background subtraction and time-walk correction for $^{180-186}$Pt

Background subtraction was also carried out for the experimental datasets in $^{180-186}$Pt. As the LaBr$_3$-LaBr$_3$ gating was employed for measurements and these detectors have relatively poor energy resolutions, we have to carefully exclude con-

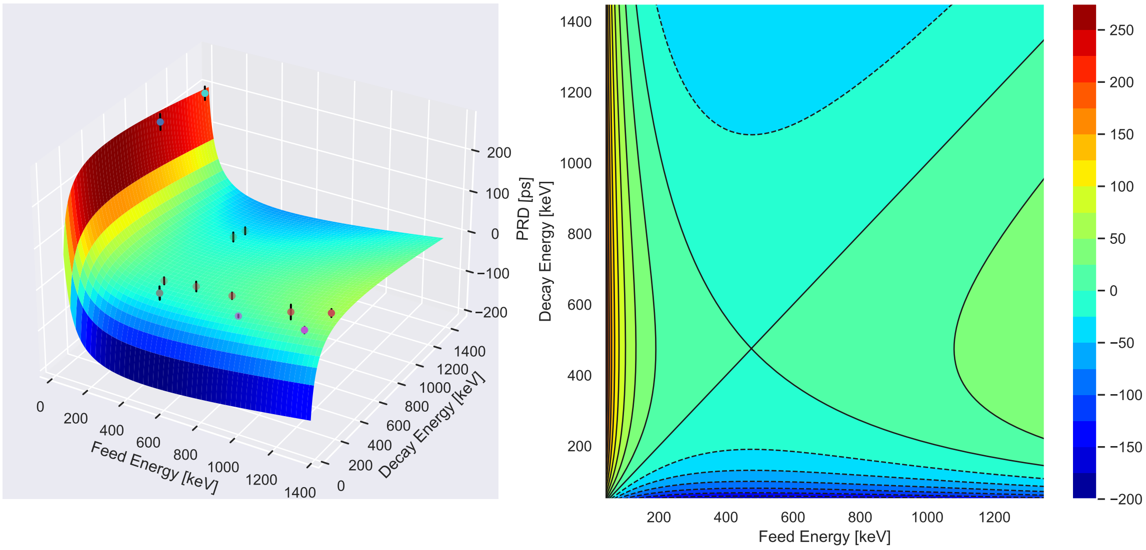

Figure 5.12: The fitted 3D PRD surface (left) with the calibration data points, and the corresponding contour plot for the fitter PRD surface (right).

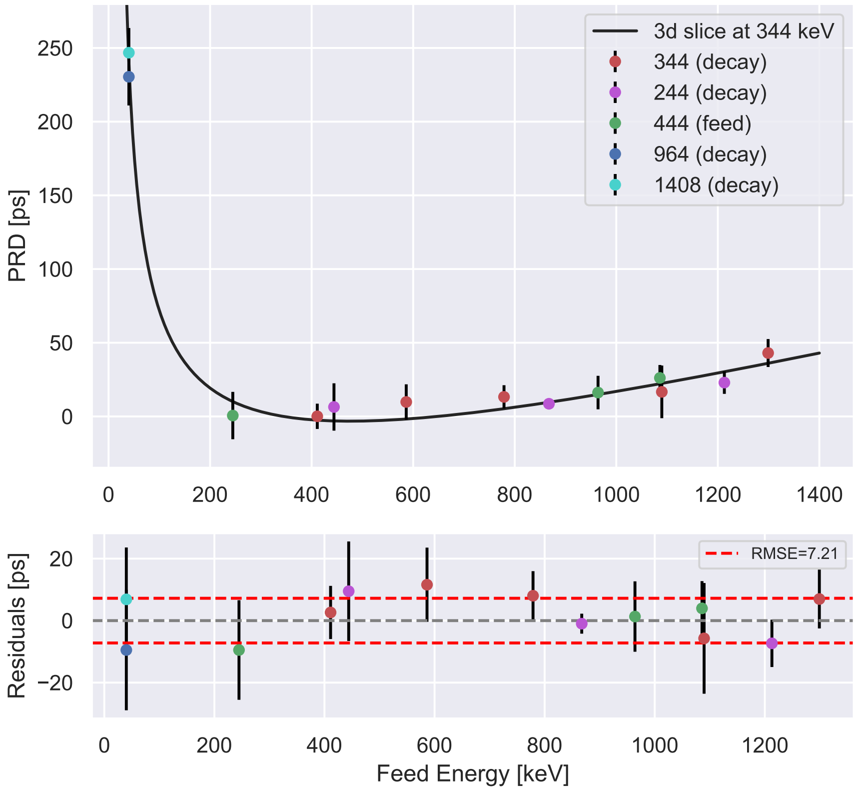

Figure 5.13: (Top) The 2D projection of the PRD surface at a reference energy of E_{decay} = 344 keV. Data points adjusted to this energy as described in the text are shown for comparison. (Bottom) The residuals of the data points relative to the projected PRD curve are shown along with red lines showing the RMSE deviations.

tamination from gate selection. Figure 5.14 presents a comparison between the full projection energy spectrum of the LaBr$_3$ detectors (black line) and the HPGe detectors (blue line) in the energy regions of the $4_1^+ \rightarrow 2_1^+$ and $2_1^+ \rightarrow 0_1^+$ transitions relevant to the present work, showing the prominent contamination. Note that the LaBr$_3$ lines have been scaled to correspond with the HPGe lines. Several peaks remain unidentified; however, their associated coincidence energies do not coincide with the cascade of interest and are, therefore, not considered in this analysis.

Figures 5.15-5.18 demonstrate the selection of peak/background gates for the $^{180-186}$Pt spectra; γ-γ coincidence matrices (top left); the decaying energy spectra gated by the feeding energy (top middle); the feeding energy spectra gated by the decaying energy (top right); the background-to-background gated spectra (bottom). The gates were carefully defined to exclude the regions associated with contamination, the precise energies of which were identified using Gaussian fits to the LaBr$_3$(Ce) spectra and being guided by the observation of potential contamination in the higher-energy-resolution HPGe spectra shown in Fig. 5.14. All peaks were avoided, including some unidentified peaks.

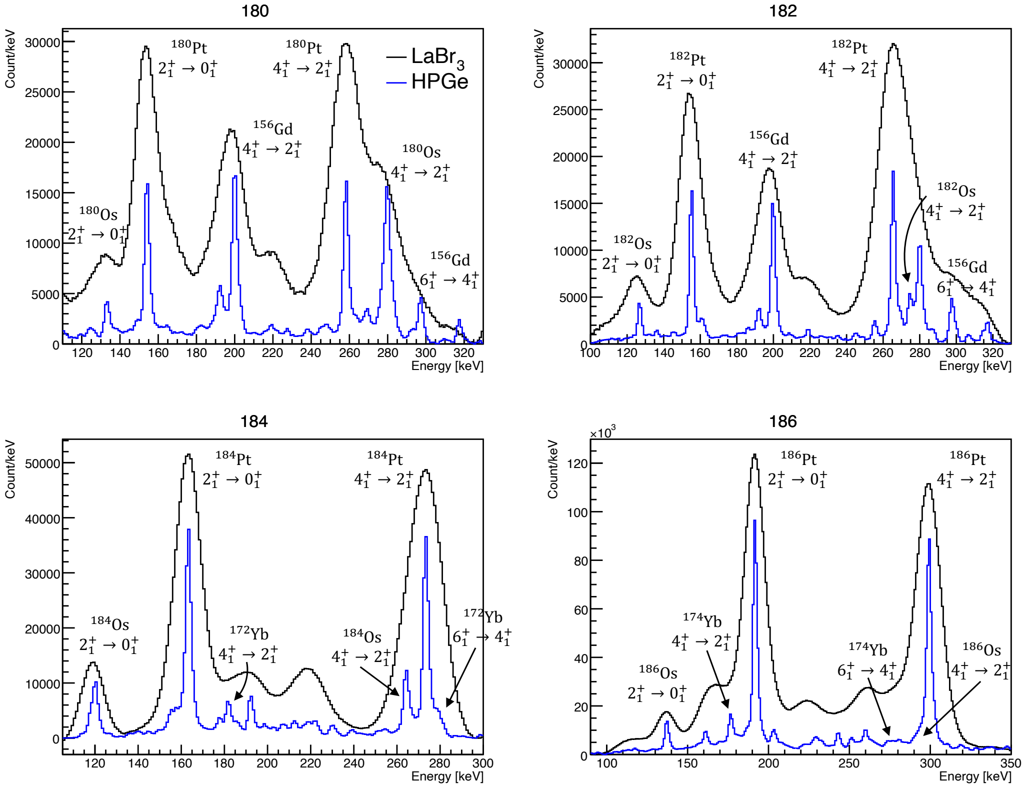

Figure 5.14: Full projection energy spectrum of the LaBr$_3$ detectors (black line) and the HPGe detectors (blue line), where the LaBr$_3$ lines have been scaled to correspond with the HPGe lines. Prominent energy peaks have been annotated with their respective origins. The spectra focus on the energy regions of the $4_1^+ \to 2_1^+$ and $2_1^+ \to 0_1^+$ transitions relevant to the present work.

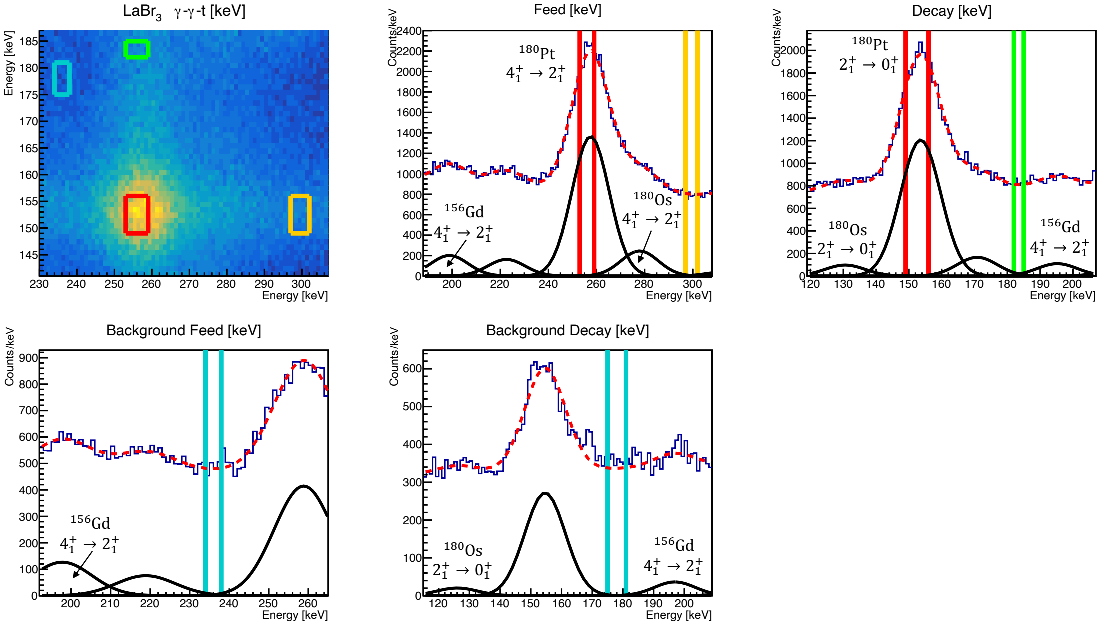

Figure 5.15: The peak/background gate selection for the ^{180}Pt gamma-ray energy spectra. The gates, indicated by the red $(p|p^m)$, orange $(p|bg^m)$, green $(bg|p^m)$ and blue $(bg|bg^m)$ regions, are positioned in areas free from prominent peaks.

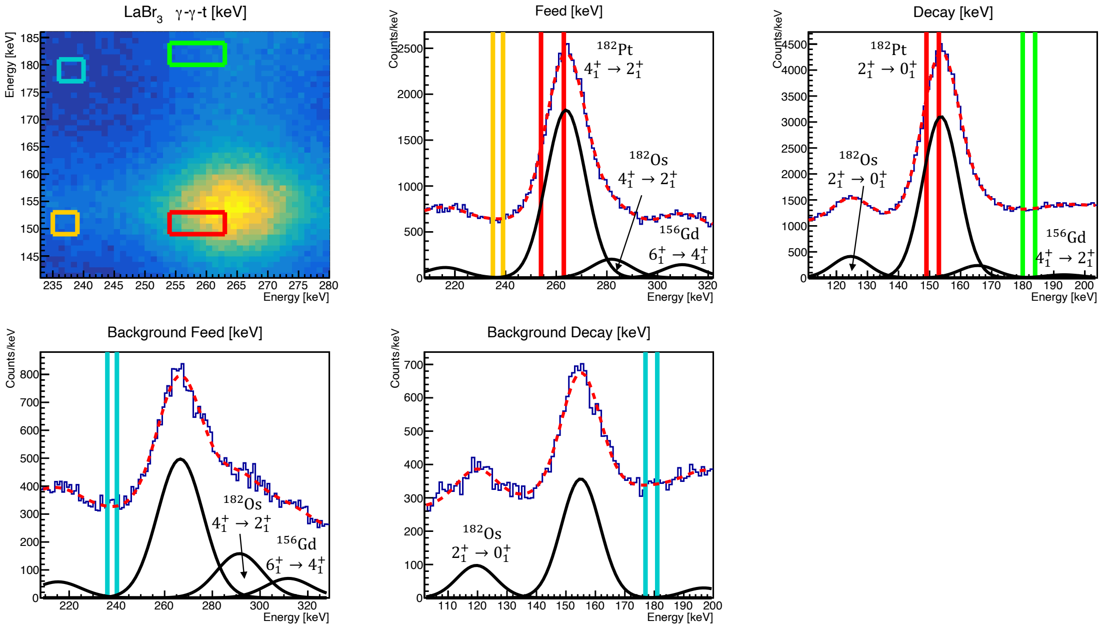

Figure 5.16: The peak/background gate selection for the ^{182}Pt gamma-ray energy spectra. The gates, indicated by the red $(p|p^m)$, orange $(p|bg^m)$, green $(bg|p^m)$ and blue $(bg|bg^m)$ regions, are positioned in areas free from prominent peaks.

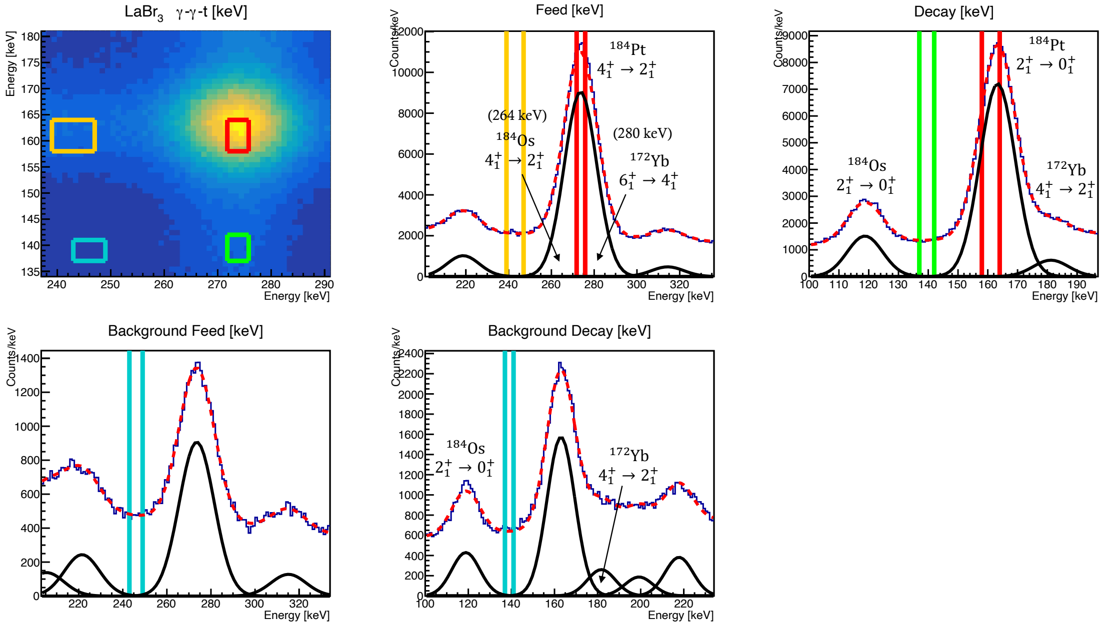

Figure 5.17: The peak/background gate selection for the ^{184}Pt gamma-ray energy spectra. The gates, indicated by the red $(p|p^m)$, orange $(p|bg^m)$, green $(bg|p^m)$ and blue $(bg|bg^m)$ regions, are positioned in areas free from prominent peaks.

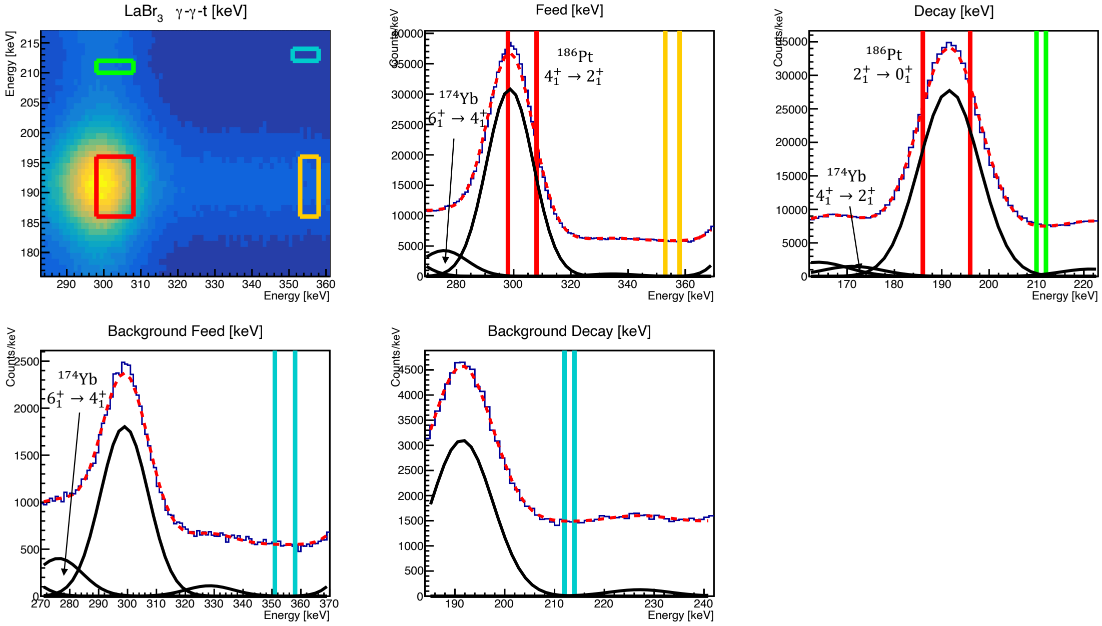

Figure 5.18: The peak/background gate selection for the ^{186}Pt gamma-ray energy spectra. The gates, indicated by the red $(p|p^m)$, orange $(p|bg^m)$, green $(bg|p^m)$ and blue $(bg|bg^m)$ regions, are positioned in areas free from prominent peaks.

Time-walk corrections were also applied to the Pt background spectra using values derived from the PRD and average energies of each gate region (see Secs. 3.1 and 3.2), as shown in Fig. 5.19. This is done since the background was sampled from various energy regions. Although the previous work [53] suggests that time-walk corrections should be applied using the Compton curve, not the PRD curve, the shifts are less than one channel, as shown in Fig. 5.19, and we assumed that they do not show substantial difference. The result of this procedure is illustrated in Fig. 5.19, which compares the time-difference spectra of each gate before and after correction.

5.4 Sum range for GCD method

In the GCD method, the sum range used to determine the spectral centroids should also be considered; the correlation between the measured lifetime and the sum range is examined here. A simulation is shown in the left panel of Fig. 5.20, using an exponential-convoluted Gaussian curve with a 350 [ps] lifetime and varying the sum range with the centre at $\Delta T = 0$ ps to determine the lifetime. The results in the right panel show the expected dependence of the measured lifetime on the range and demonstrate that the sum range should be selected within the stable plateau region of the curve.

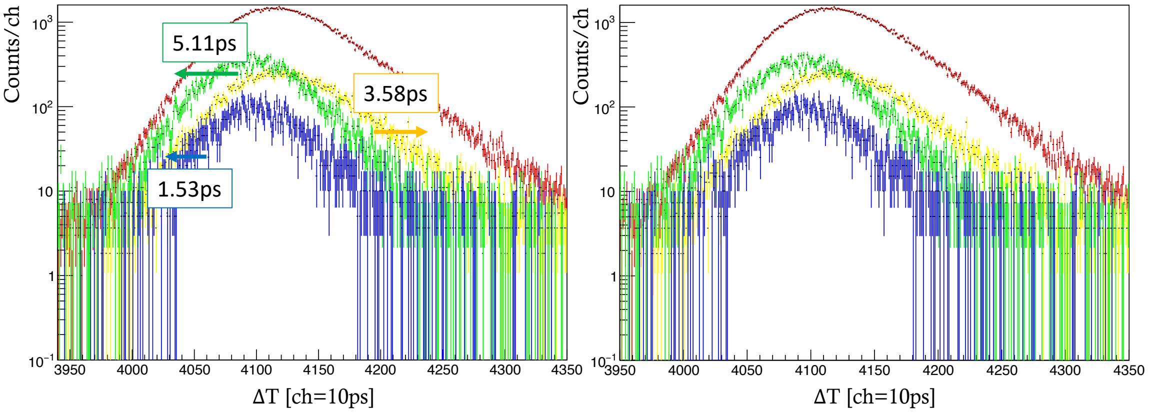

Figure 5.19: Time-difference spectra for ^{186}Pt before (left) and after (right) the application of the time-walk correction using the PRD curve, where each gate, $p|p^m$, $p|bg^m$, $bg|p^m$ and $bg|bg^m$, is coloured in red, orange, green and blue, respectively. $\Delta T = 0$ corresponds to 4096 ch. The shifts are less than one channel given the 10 ps/ch resolution.

Figure 5.21 shows the experimentally obtained lifetime values for the 2_1^+ states in $^{180-186}$Pt using the GCD method, depending on the sum range with the centre at $\Delta T = 0$ ps (4096 ch). It was observed that the lifetimes exhibit an increase as the sum range is extended, especially in ^{180,182}Pt. This is attributed to the effect of including the wings, with the extra counts increasing the centroid values away from $t = 0$. For ^{184}Pt and ^{186}Pt, a clear plateau is evident, which makes the selection of the summation range straightforward. In contrast, the curves for ^{180}Pt and ^{182}Pt exhibit more fluctuation due to low statistics.

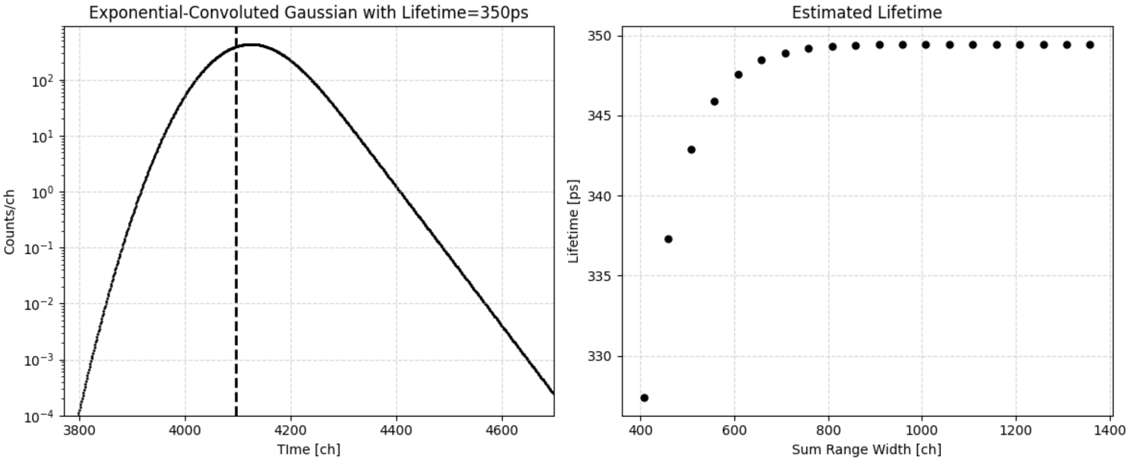

Figure 5.20: Theoretical investigation of how the sum range affects a lifetime measured with the GCD method using an exponential-convoluted Gaussian curve with a lifetime of 350 ps. The extracted lifetime is plotted depending on the sum range with the centre at $\Delta T = 0$ ps (4096 ch) in the right panel, showing that the correct lifetime is obtained in the plateau region.

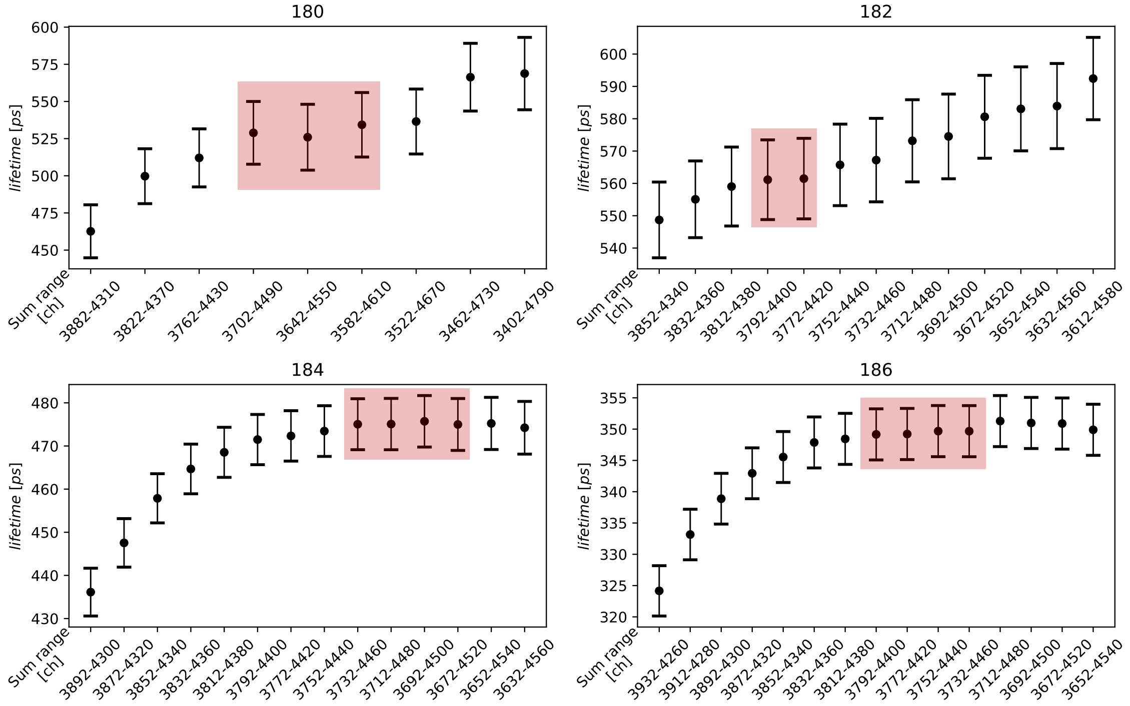

Figure 5.21: Experimental lifetime of the 2_1^+ states in $^{180-186}$Pt as a function of the GCD sum range with the centre at $\Delta T = 0$ ps (4096 ch). The final lifetime values were extracted using the channel range corresponding to the stable plateau regions highlighted in red.

5.5 Lifetime results

Finally, similar to that was done for the PRD analysis, the dependence of the measured lifetime on the selected $p|p^m$ window size was investigated as shown in Fig. 5.22. Lifetimes were determined using both the GCD method (black points) and the convolution method (red points). Regions with minimal lifetime variation and agreement between both methods, highlighted in red, were selected as the $p|p^m$ gates for final analysis.

Figure 5.23 illustrates the final energy gates for all isotopes investigated. As mentioned in the work by E.R. Gamba *et al.* [53], methods such as placing background gates immediately adjacent to the peaks or using interpolation with a Compton curve are plausible, however for the present Pt analysis, a similar procedure to that which was employed to evaluate the time-walk correction in Sec. 5.2 was used, as shown in Fig. 5.19. It should be noted that the choice of off-centre peak-to-peak gates, notably for ^{182}Pt in Fig. 5.23, is justified by the contamination analysis shown in Figs. 5.15-5.18.

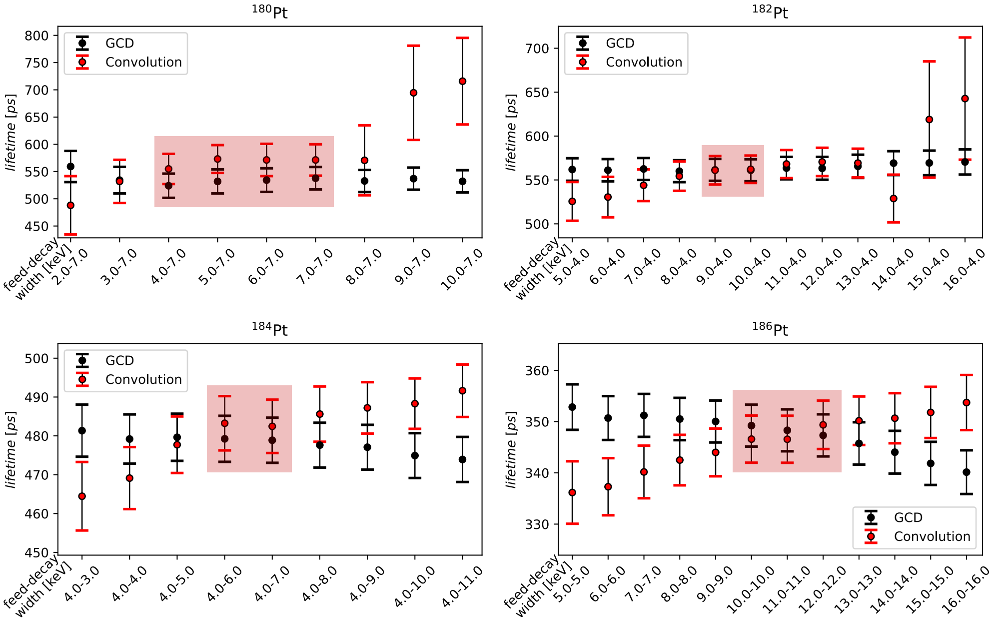

Figure 5.22: Measured lifetimes as a function of the $p|p^m$ window size, with the centre at the peak-to-peak gates, as shown in Figs. 5.15-5.18, determined using the GCD (black points) and convolution (red points) methods. The stable regions used for analysis are highlighted in red.

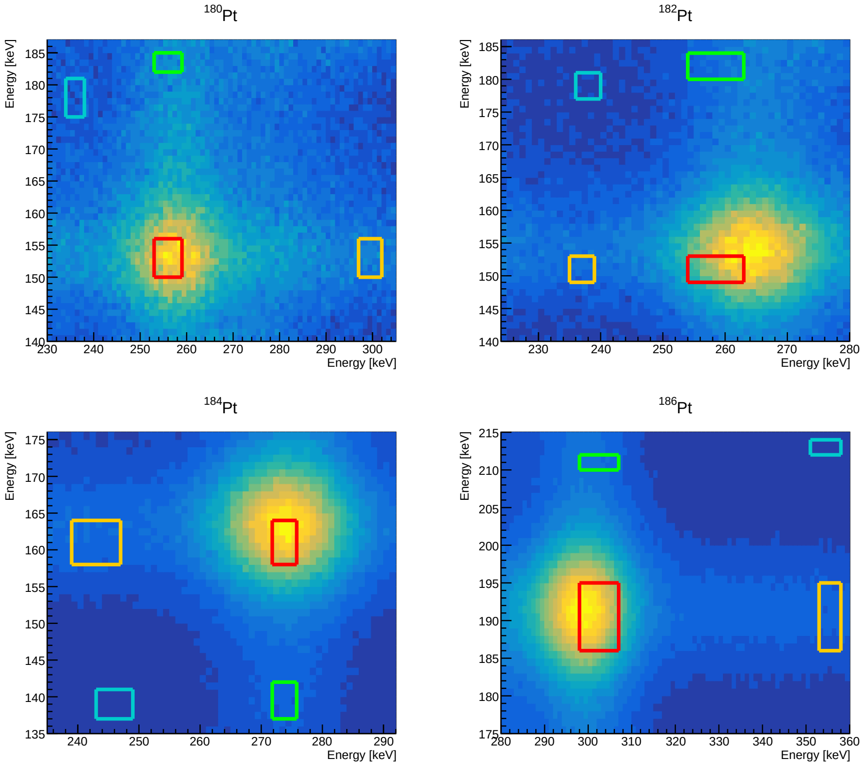

Figure 5.23: Final energy gates applied to the γ-γ-t matrices for $^{180-186}$Pt. The peak gate is indicated by the red region, and the background gates are shown as yellow, green and blue regions. Each gate, $p|p^m$, $p|bg^m$, $bg|p^m$ and $bg|bg^m$, is coloured in red, orange, green and blue, respectively.

As discussed in Sec. 3.3.3, two approaches within the GCD method were considered to determine the true peak-to-peak centroid positions $C^t_{p|p}$. The first approach is physical subtraction using Eq. 3.6, and the second approach is a mathematical calculation, which uses the measured centroid values C^m of each gate and the corresponding number of counts n^m, as listed in Tab. 5.2, to determine the true centroid using Eq. 3.15. Table 5.3 compares the final centroid values and the resulting centroid difference obtained from both methods, resulting in a clear agreement with each other as expected from the discussion in Sec. 3.3.3.

Table 5.2: Measured centroids C^m in picoseconds and the corresponding number of counts n^m for the peak/background regions of both forward and reversed spectra.

Fwd	$C^m_{p\|p}$	$C^m_{p\|bg}$	$C^m_{bg\|p}$	$C^m_{bg\|bg}$	$n^m_{p\|p}$	$n^m_{p\|bg}$	$n^m_{bg\|p}$	$n^m_{bg\|bg}$
180	366(10)	290(21)	101(21)	101(26)	6983	2335	3010	1811
182	428(7)	328(21)	113(13)	111(24)	9117	2540	2666	1452
184	416(4)	311(8)	221(12)	180(20)	24662	4739	4242	1509
186	296(1)	329(5)	14(6)	104(14)	162162	28228	34159	9035

Rev	$C^m_{p\|p}$	$C^m_{p\|bg}$	$C^m_{bg\|p}$	$C^m_{bg\|bg}$	$n^m_{p\|p}$	$n^m_{p\|bg}$	$n^m_{bg\|p}$	$n^m_{bg\|bg}$
180	-356(10)	-251(22)	-55(21)	-33(26)	6873	2438	2962	1779
182	-392(7)	-280(20)	-34(13)	-67(25)	8862	2716	2586	1398
184	-396(4)	-259(8)	-190(13)	-173(21)	24529	4798	3950	1545
186	-269(1)	-313(6)	1(6)	-77(12)	163218	28699	31948	8646

Table 5.3: Comparison of the final true centroid values C^t and the total centroid shift ΔC derived using physical background subtraction versus the mathematical calculation. The consistency between the two methods provides a robust cross-check on the analysis procedure.

	Method	$C^t_{p\|p}$ (fwd) [ps]	$C^t_{p\|p}$ (rev) [ps]	ΔC [ps]
180	Physically	510(29)	-531(31)	1041(43)
	Mathematically	510(34)	-531(36)	1041(50)
182	Physically	546(17)	-549(17)	1095(24)
	Mathematically	546(18)	-549(20)	1095(27)
184	Physically	472(7)	-460(6)	933(9)
	Mathematically	472(8)	-460(7)	933(11)
186	Physically	359(3)	-320(3)	680(4)
	Mathematically	359(3)	-320(3)	680(4)

Figure 5.24 illustrates the application of the GCD and convolution methods to the time-difference spectra for ^{186}Pt. The left panel shows the convolution method, where the spectrum is fitted with Eq. 3.8 (solid red line). Although the fit was done to the summed data, as described in Sec. 3.3.2, the fits shown here generally show only the forward spectrum alone. The right panel demonstrates the GCD method, indicating the centroids of the forward (solid black line) and reversed (solid red line) spectra. As discussed in Sec. 3.3.3 and also shown in Tab. 5.3, these centroid positions may be asymmetrically reflected about $\Delta T = 0$ (dotted black line).

Table 5.4 lists the final results for the lifetime values and their statistical errors, along with the corresponding B(E2) values and the Grodzins product. The GCD method shows consistent values with smaller uncertainties than the convolution method, as shown in Fig. 5.22, leading to the selection of the GCD results as our final values. All factors that can cause systematic errors, like summing and gating ranges, were carefully considered (see Figs. 5.21 and 5.22); thus, no systematic errors were found except for the convolution method in ^{182}Pt from the gating-range variation, yielding $\sigma_{sys} = 8.49\,\text{ps}$.

Table 5.5 compares the lifetime values from references and this work. The values determined for ^{180}Pt and ^{186}Pt are in good agreement with the values from ENSDF [4, 7]. The result for ^{182}Pt disagrees with the ENSDF value [5], but is consistent with the recent experimental value that was obtained with the GCD method [10]. However, a discrepancy is observed for ^{184}Pt, where the lifetime measured in this work is approximately 7% shorter than the ENSDF value [6].

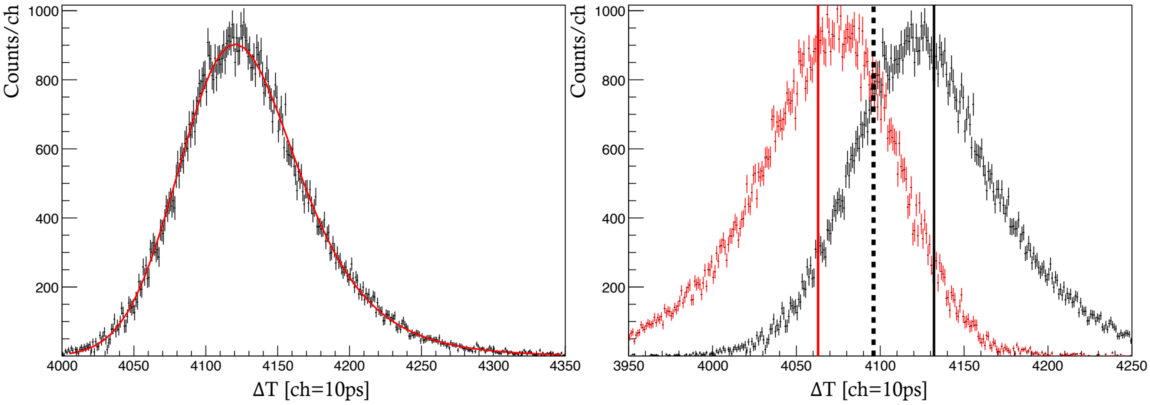

Figure 5.24: Time-difference spectra for ^{186}Pt used in the convolution (left) and GCD methods (right). The solid red line in the left panel represents the fitted curve, while the solid black and red lines in the right panel indicate the centroids of the forward and reversed spectra. $\Delta T = 0$ corresponds to 4096 ch.

Table 5.4: Lifetime results for the 2_1^+ states in $^{180-186}$Pt from our measurements, including derived values for the Grodzins product and reduced transition strengths.

Mass (A)	Method	Meanlife [ps]	Grodzins product [$e^2b^2\ keV$]	B(E2) [e^2b^2]	B(E2) [W.u.]
180	convolution	571(30)	0.704(36)	0.88(5)	145.2(75)
	GCD	534(22)	0.753(31)	0.94(4)	155.3(63)
182	convolution	561(16)	0.706(20)	0.86(2)	140.8(41)
	GCD	561(12)	0.705(16)	0.86(2)	140.7(31)
184	convolution	483(7)	0.735(10)	0.85(1)	136.4(20)
	GCD	479(6)	0.741(10)	0.86(1)	137.6(17)
186	convolution	347(5)	0.663(9)	0.65(1)	102.5(14)
	GCD	349(4)	0.658(8)	0.64(1)	101.8(12)

Table 5.5: Comparison of experimental lifetimes for the 2_1^+ states in $^{180-186}$Pt. Values from this work are presented alongside data from the literature [4–10].

Mass (A)	$4_1^+ \rightarrow 2_1^+$ [keV]	$2_1^+ \rightarrow 0_1^+$ [keV]	Meanlife [ps]
180	257.6	153.3	534(22)[a]
			480(10)[b]
			420(20)[c]
			540(50)[e]
182	264.7	154.9	561(12)[a]
			563(12)[d]
			691(43)[e]
184	272.2	162.4	479(6)[a]
			519(17)[e]
186	298.8	191.5	347(5)[a]
			346(29)[e]

[a] This work using the GCD method.

[b] L. Barver *et al.* using the RDM method [8].

[c] Müller-Gatermann *et al.* using the convolution method [9].

[d] Häfner, G *et al.* using the GCD method [10].

[e] ENSDF [4–7].

Figure 5.25 illustrates the Grodzins product (top) and B(E2) values (bottom), including the results from this work, showing that the values from this study show a generally smooth trend across mass numbers, although ^{184}Pt shows a slight deviation. To provide a broader context for this trend, the experimental B(E2) values are also compared with those deduced from laser spectroscopy measurements of ground-state charge radii and the derived deformation magnitude [69–71], using the equation below taken from Ref. [72]

$$B(E2\uparrow) = \left(\frac{3\langle\beta_2^2\rangle^{1/2} Z R_0^2}{4\pi}\right)^2, \tag{5.2}$$

where $\langle\beta_2^2\rangle^{1/2}$ is the model-dependent quadrupole deformation parameter, and the nuclear radius parameter R_0^2 is given by

$$R_0^2 = 0.0144A^{2/3}\,[b]. \tag{5.3}$$

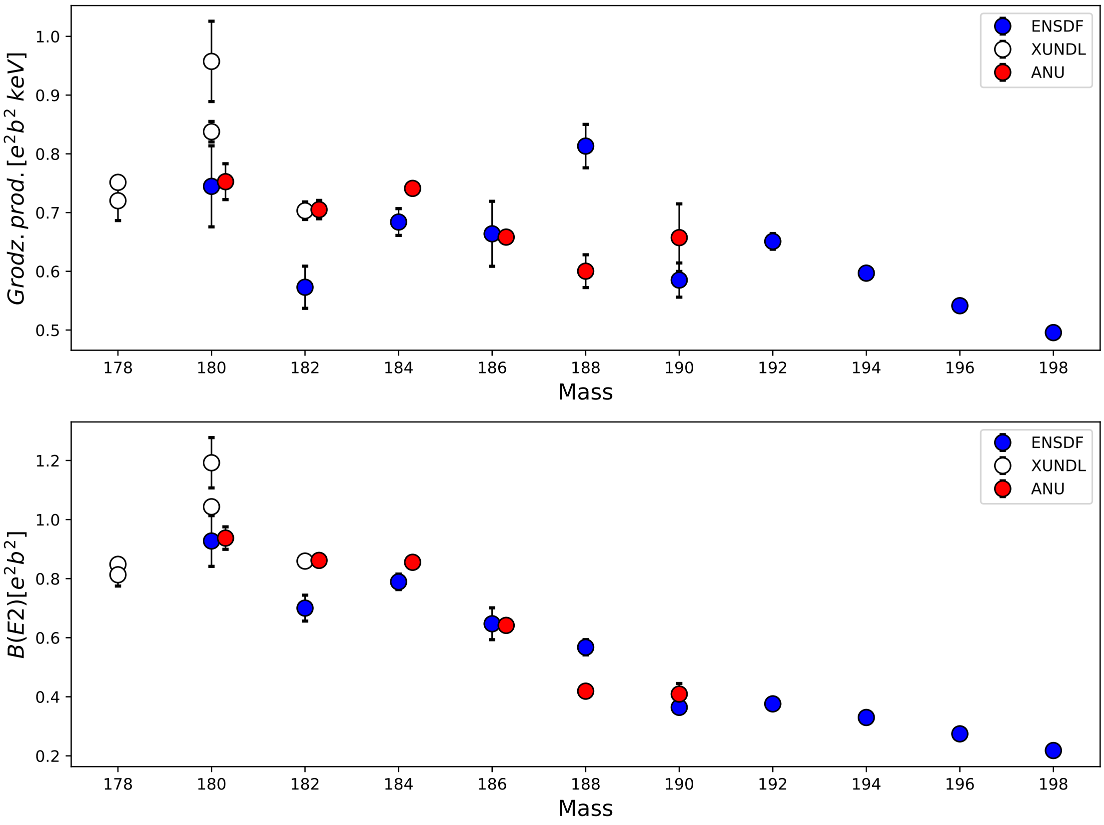

Figure 5.25: Grodzins product (top) and reduced transition strengths (bottom) for the even-even platinum nuclei derived using the lifetime measurements from literature [4–10, 13–19], this study in $^{180-186}$Pt (see Tab. 5.5) and previous ANU measurements in $^{188-190}$Pt [11, 12].

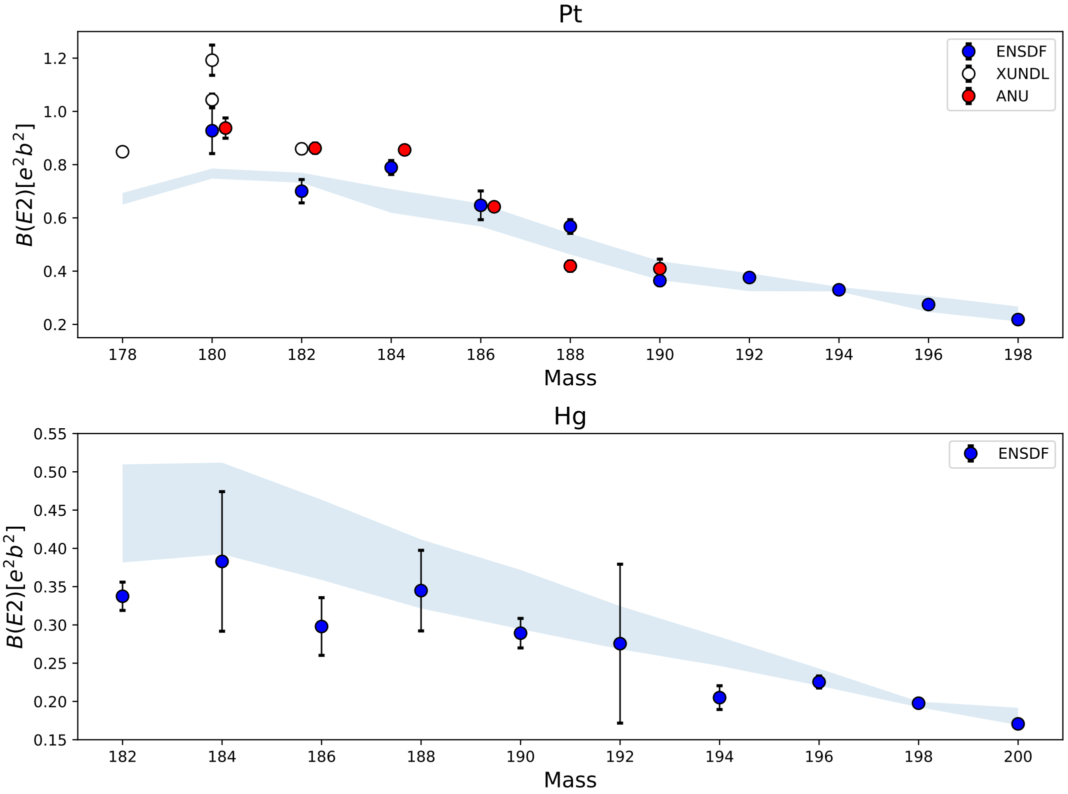

Figure 5.26: Reduced transition strengths of Pt (top) and Hg (bottom) [4–10, 13–19, 73], along with deduced values from laser spectroscopy measurements of the ground-state charge radii [33, 69].

These results are shown in Fig. 5.26 for neutron-deficient Pt and also Hg isotopes, with the deduced values from the ground-state charge radii measurements [69–71], highlighted in the blue bands.

While there is good agreement between the experimental data and the charge-radii-derived values for the heavier isotopes in both Pt and Hg, significant deviations emerge in the lighter mass region. This discrepancy may be seen as a confirmation of the shape coexistence and shape mixing that occurs in the mid-shell Pt and Hg isotopes. The deviation can be attributed to an assumption in the calculation (Eq. 5.3), which presupposes that the quadrupole deformations of the 0_1^+ ground state and the 2_1^+ state are identical. This approximation may not be valid, especially for the shape coexistence region in $^{180-186}$Pt. Furthermore, while the lighter Hg isotopes exhibit B(E2) values lower than the blue band, the lighter Pt isotopes show the opposite trend. This contrasting behaviour is likely a consequence of their different ground-state deformations, which are predominantly prolate for platinum and oblate for mercury. To investigate these trends further, the following chapter compares the experimental B(E2) values to those derived using the wavefunctions that result from three-band mixing calculations.

Chapter 6

Band-mixing model

This chapter interprets the 2_1^+ state lifetimes of $^{180-186}$Pt measured in the present work, along with data on ^{178}Pt, using the phenomenological band-mixing model that was described earlier in Sec. 2.6.

Initially, a two-band mixing calculation was performed for ^{178}Pt in Sec. 6.1. This represents a simplified case, and has validity due to the lack of clear evidence for a γ band (and hence three-band mixing) in the lower even-spin region. The calculation serves to confirm the signs of the quadrupole moments used to determine the B(E2) transition strengths (see Sec. 2.6.4). Subsequently in Sec. 6.2, two types of three-band mixing calculations with alternative ways to include the γ band, the common and fixed ways (see Sec. 2.6.4), were applied to $^{180-186}$Pt. Note that ^{186}Pt is located in a transitional region, as mentioned in Sec. 1, and the assumption of a well-defined three-band structure is less reliable. To constrain the model parameters in three-band mixing, the fitting procedure also incorporated experimental branching ratios in addition to the level energies.

6.1 Two-band mixing for ^{178}Pt

The fitted parameter results of the two-band mixing model, fitted only to the level energies of ^{178}Pt, are presented in Tab. 6.1. Also, level-scheme comparisons and resulting wavefunction amplitudes are presented in Fig. 6.1 and Tab. 6.2[1], respectively. The second excited 8^+ state at 2197 keV was excluded because its energy deviates significantly from the systematic trend of the other levels in the yrare band. This state may instead be a member of a third, unobserved band, or miss-assigned, underscoring the need for further measurements. In comparison with the earlier results derived from the three-band mixing model in ^{178}Pt [40], the band-head energies for both the g band and the d band, $\mathfrak{I}_0$ of the d band and V_{gd} demonstrate concurrence.

---

[1] The results indicate that the g-band, referring to a ground-state band as in Refs. [32,40], is no longer a ground-state band. We maintain this naming for easier comparison with the references.

Table 6.1: Parameters from the two-band mixing model fit for ^{178}Pt.

Parameters		^{178}Pt
g band	$\mathfrak{I}_0\,[\times 10^{-2}\,\mathrm{keV}^{-1}]$	0.02
	$C\,[\times 10^{6}\,\mathrm{keV}^{3}]$	2.81
	E_0 [keV]	231
d band	$\mathfrak{I}_0\,[\times 10^{-2}\,\mathrm{keV}^{-1}]$	2.95
	$C\,[\times 10^{6}\,\mathrm{keV}^{3}]$	1.15
	E_0 [keV]	187
	V_{gd} [keV]	209

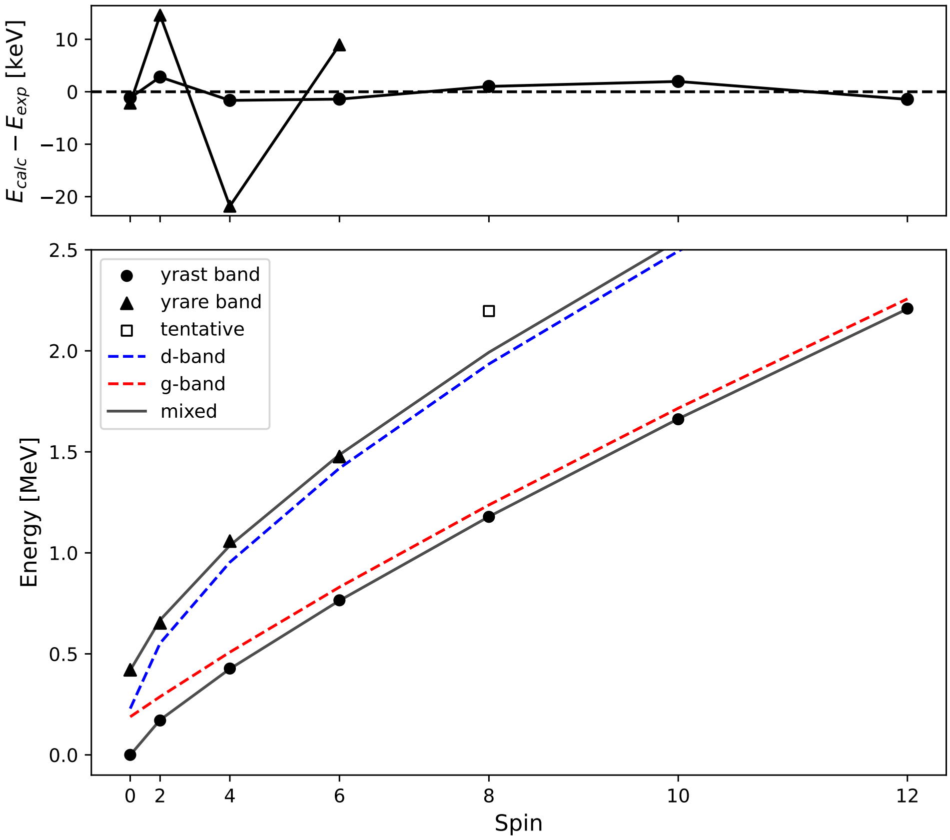

Figure 6.1: Comparison between experimental energies (points) for the yrast and yrare bands in ^{178}Pt up to spin 12 and the results of the two-band mixing model fit. The calculated mixed energies are shown as solid lines, while the unperturbed band energies are represented by dotted lines. The second excited I=8 state (open square) was excluded from the fit as the deviation from the systematic trend is sufficiently large that it suggests it may belong to another band or be mis-assigned.

However, $\mathfrak{I}_0$ for the g band and both C parameters appear reduced in the present study. This difference can be attributed to the exclusion of an additional band residing in a higher energy region, which can primarily influence the g band.

Table 6.2: Experimental level energies from ENSDF [13] are compared to calculated level energies in ^{178}Pt from the two-band mixing model. The wavefunction amplitudes, representing the mixing of the g band (A_g) and d band (A_d) , are also listed for each energy level.

State	Observed	Calculated	Wavefunction Amplitudes	
	Energy [keV]	Energy [keV]	A_g	A_d
0^+	0	-1	-0.672	0.741
	421	419	0.741	0.672
2^+	170	173	-0.482	0.876
	653	668	0.876	0.482
4^+	427	426	-0.368	0.930
	1058	1036	0.930	0.368
6^+	765	764	-0.304	0.953
	1477	1486	0.953	0.304
8^+	1178	1179	-0.267	0.964
		1993	0.964	0.267
10^+	1661	1663	-0.244	0.970
		2546	0.970	0.244
12^+	2209	2208	-0.231	0.973
		3138	0.973	0.231

The relative sign of the quadrupole moments of the g and d bands was then investigated by comparing the calculated branching ratios with experimental values, as illustrated in Fig. 6.2. Two cases were considered: one considers the g and d bands to have the same sign (top panel) and another where they have opposite signs (bottom panel). The root-mean-square error (RMSE) between the calculated and experimental data is 1.98 for the same-sign case and 4.49 for the opposite-sign case.

A similar comparison was made for the B(E2) transition strengths, know from Ref. [13], within the yrast state as shown in Fig. 6.3. Although the model that assumes same-sign quadrupole moments (left) successfully reproduces the experimental B(E2; $2_1^+ \rightarrow 0_1^+$) value, at higher spins, both the same-sign and opposite-sign cases tend to overestimate the experimental data. This discrepancy also can be at-

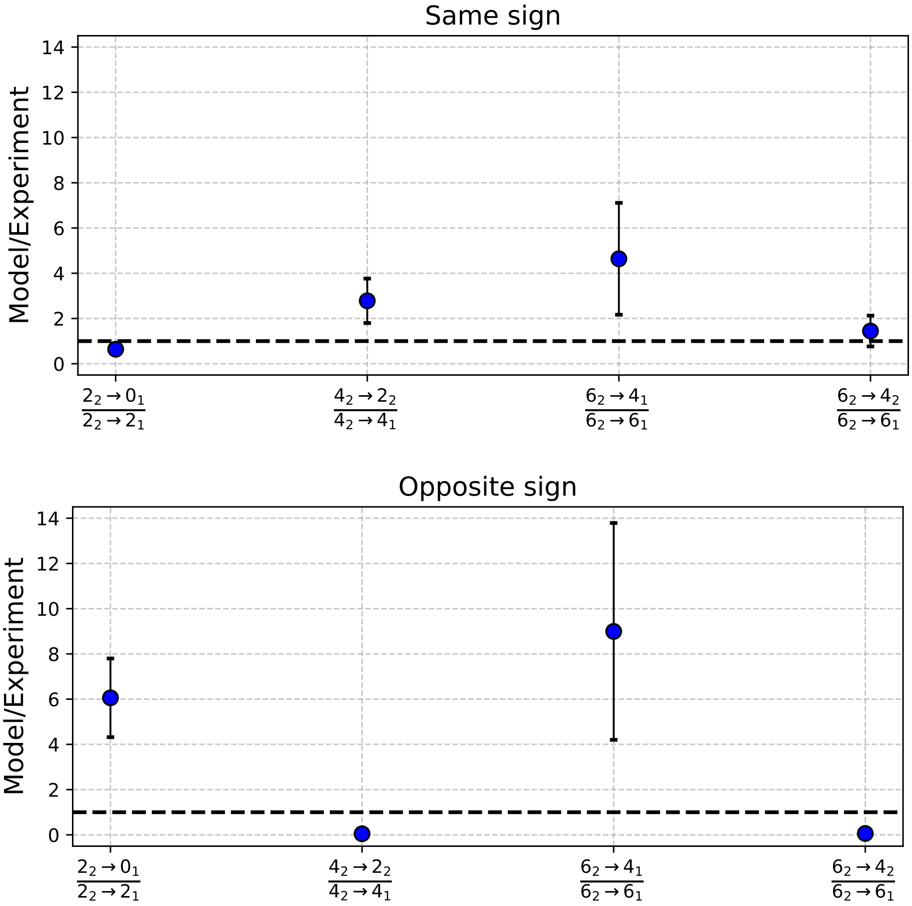

Figure 6.2: Ratio of calculated to experimental branching ratios in ^{178}Pt. The top panel assumes the same sign for quadrupole moments of the g and d bands, resulting in a RMSE of 1.98. The bottom panel assumes opposite signs, yielding an RMSE of 4.49. The better agreement shown in the top panel provides evidence for the same-sign assumption within the two-band-mixing model.

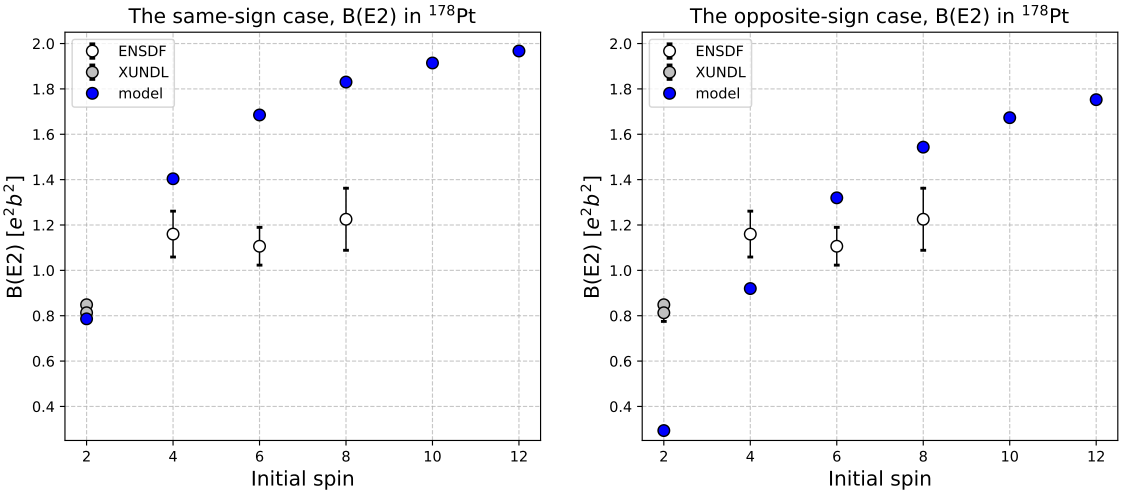

Figure 6.3: Experimental (white/grey) [13] and calculated (blue) B(E2; $I \rightarrow I-2$) transition strengths within the yrast state in ^{178}Pt. The comparison is shown for two cases: the same-sign case (left) and opposite-sign case (right).

tributed to the ignoring of additional bands in the analysis, which can have a more pronounced impact on the higher-spin region, thereby underscoring once again the necessity for further experimental data.

Based on the results presented, the same sign for the quadrupole moments is strongly required by the band-mixing model, but these results contradict the fact that the quadrupole moment should be positive for prolate, and negative for oblate shapes. We leave it open for further investigation including allowing the ground state to be triaxial or addressing any limitations of the B(E2) calculations in this model. In the present analysis, we adopt the same sign for all bands. Table 6.3 presents the calculated and experimental branching ratios, assuming the same-sign case.

Table 6.3: Experimental (from ENSDF [13]) and calculated branching ratios, assuming the same-sign case, in ^{178}Pt.

Initial state A	Final state B	γ-ray A → B	I_γ A → B	Final state C	γ-ray A → C	I_γ A → C	Expt. BR[a]	Calc. BR[b]
2_2^+	0_1^+	653	8.0(22)	2_1^+	483	14.6(12)	0.55(16)	0.35
4_2^+	2_2^+	405	3.6(9)	4_1^+	631	8.0(20)	0.45(16)	1.25
6_2^+	4_1^+	1049	3.4(16)	6_1^+	712	3.2(8)	1.06(57)	4.93
	4_2^+	418	2.5(10)				0.78(37)	1.13

[a] Experimental branching ratios $I_\gamma(A \rightarrow B)/I_\gamma(A \rightarrow C)$.

[b] Calculated branching ratios $B(E2; A \rightarrow B)E_\gamma^5(A \rightarrow B)/B(E2; A \rightarrow C)E_\gamma^5(A \rightarrow C)$.

6.2 Three-band mixing for $^{180-186}$Pt

6.2.1 Comparison between the *common* and *fixed* ways

Three-band mixing calculations were performed for the $^{180-186}$Pt isotopes, using two methods to constrain the inertia parameters of the γ band as was described in Sec. 2.6.4. The common way constrains the parameters of $\mathfrak{I}_0$ and C of the γ band to those of the d band, while the fixed way needs $\mathfrak{I}_0$ and C parameters for the γ band as a prerequisite. These two parameters were determined in the fixed way by fitting the energies of the odd-spin states in $^{180-184}$Pt to the VMI model simultaneously[2], as shown in Fig. 6.4. Although the band-head energies (E_0) were fitted to the odd-spin states when determining $\mathfrak{I}_0$ and C, they were not fixed in the subsequent full three-band calculations.

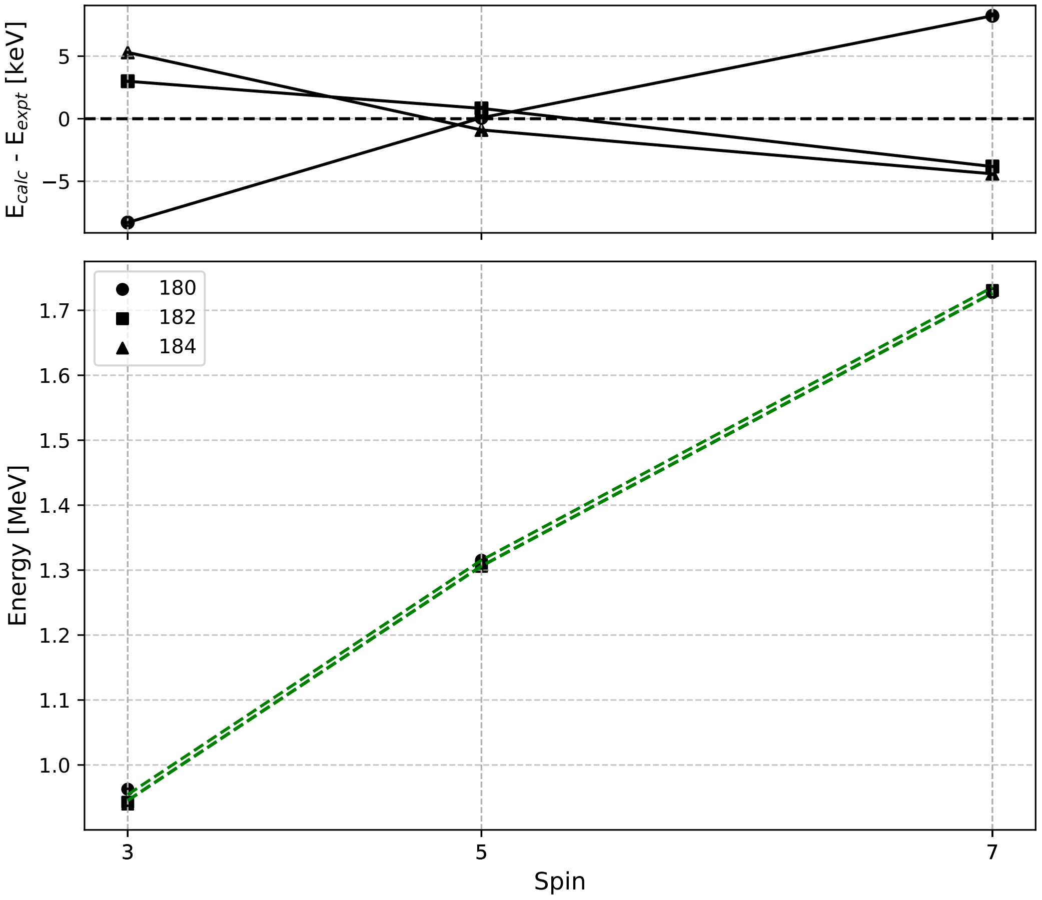

Figure 6.4: VMI model fit (green lines) to the odd-spin states of the γ bands in $^{180-184}$Pt, simultaneously. The fit was used to determine the moment of inertia at I=0 ($\mathfrak{I}_0$) and softness (C) parameters, which served as fixed inputs in the fixed-way calculations.

---

[2] Here, ^{186}Pt was excluded from this fit because it is located in a transitional region, where the assumption of a well-defined three-band structure is less reliable.

With using these fitted parameters, three-band mixing calculations with the fixed approach, along with the common approach, were carried out. Table 6.4 presents the RMSE between the calculations and experimental data for both level energies and branching ratios. The results indicate that the fixed way provides a better overall description, outperforming the common way in all cases except for the level energies in ^{186}Pt. The gradual increase in the energy RMSE approaching ^{186}Pt can suggest the limitation of calculations approaching the transitional region.

A further comparison between the common and fixed γ-band approaches is made by examining the trends of the fitted parameters versus mass number as illustrated in Figs. 6.5 and 6.6. The parameters shown, which include the band-head energies of the g and γ bands relative to the d band, $\mathfrak{I}_0$, C and inter-band interactions, are expected to follow certain physical behaviours. Generally, a smooth evolution with changing mass numbers is expected. Considering the experimental data within this mass region, the band-head energy of the g band relative to the d band is predicted to exhibit a parabolic trend that peaks at ^{182}Pt to reflect the experimental energy level trend in Pt isotopes as shown in Fig. 1.1. It is also expected that the d band will exhibit a larger moment of inertia $\mathfrak{I}_0$ compared to the g band.

A comparison of the two figures indicates that the parameters derived from the fixed way align with most of the physical expectations. Conversely, the common way produces multiple discrepancies. For instance, the g-band energy relative to the d-band energy maximises at ^{184}Pt and the γ-band energy is not smooth within mass. The g and d bands do not have clearly different moments of inertial and furthermore the interactions in the common way are counter-intuitive, characterised by a minimal g-d interaction (V_{gd}) and a surprisingly substantial interaction between the d and γ bands ($V_{d\gamma}$). Lastly, it should be noted that in both the common and fixed ways, the stiffness parameter C of the g band exhibits a jump between ^{182}Pt and ^{184}Pt, in contrast to all other parameters being relatively smooth for the fixed-way fits.

Table 6.4: Comparison of the RMSE between the two approaches to the γ band mixing calculations for experimental level energies and branching ratios in $^{180-186}$Pt.

Mass	RMSE in Common way		RMSE in Fixed way	
	Energy [keV]	Branching ratio	Energy [keV]	Branching ratio
180	41.9	2.63	19.0	1.73
182	37.7	3.78	22.5	3.68
184	15.3	4.68	9.50	4.40
186	52.0	8.77	78.1	2.52

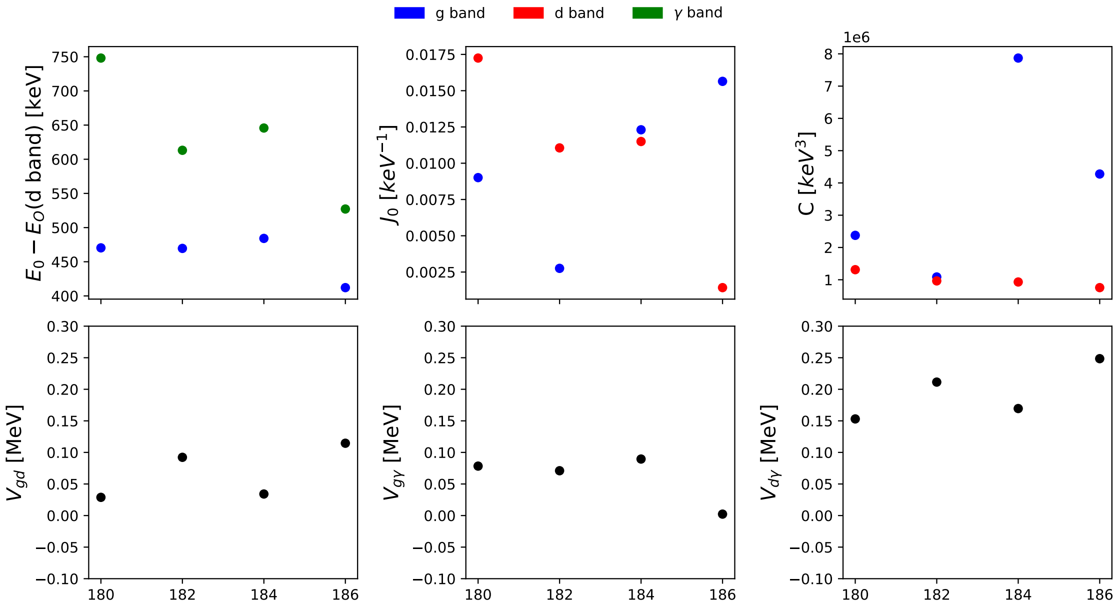

Figure 6.5: Trends of the fitted model parameters for $^{180-186}$Pt versus mass number from the band-mixing model within the γ-band VMI parameters constrained to be common to the d band (common way).

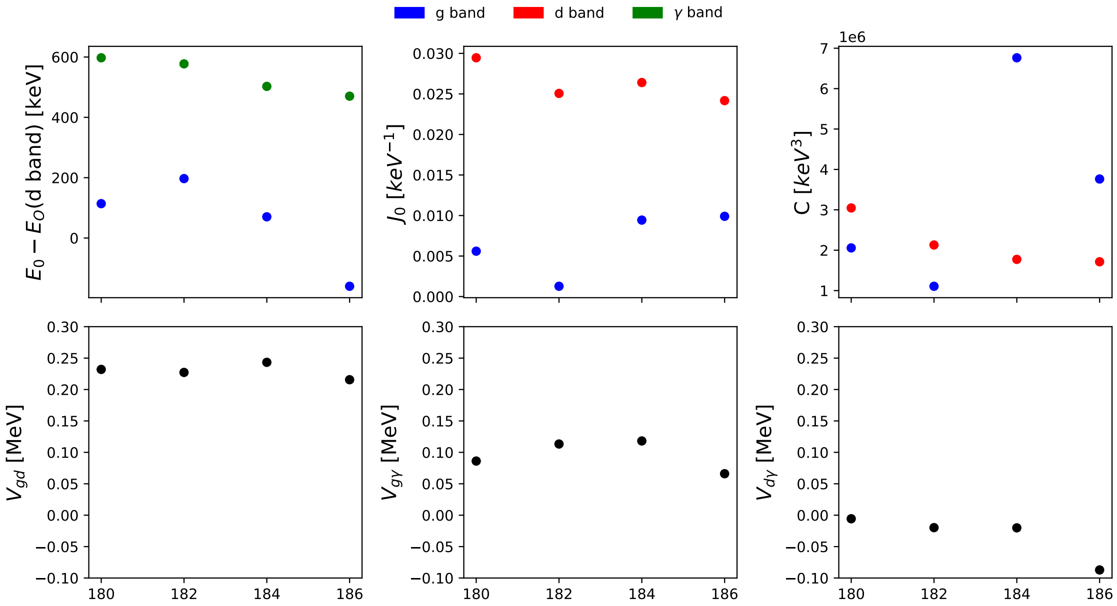

Figure 6.6: Trends of the fitted model parameters for $^{180-186}$Pt versus mass number from the band-mixing model within the γ-band VMI parameters constrained to be fixed determined from the odd-spin members of the γ band in $^{180-184}$Pt as shown in Fig. 6.4 (fixed way).

Finally, Fig. 6.7 compares the calculated B(E2) transition strengths (see Sec. 2.6.3) within the yrast state with experimental data, including the new values measured in this work. For this observable, the fixed way again provides a superior description of the experimental trends compared to the common way. In general, the common way greatly undershoots the experimental values.

Based on the superior performance demonstrated above, the fixed way was adopted for the three-band mixing analysis of the $^{180-186}$Pt. The fitted parameters, level-scheme comparisons and resulting wavefunction amplitudes are presented in the following figures and tables. In contrast to the previous study that performed the same three-band-mixing calculations for ^{180,182}Pt with fewer energy points [40],

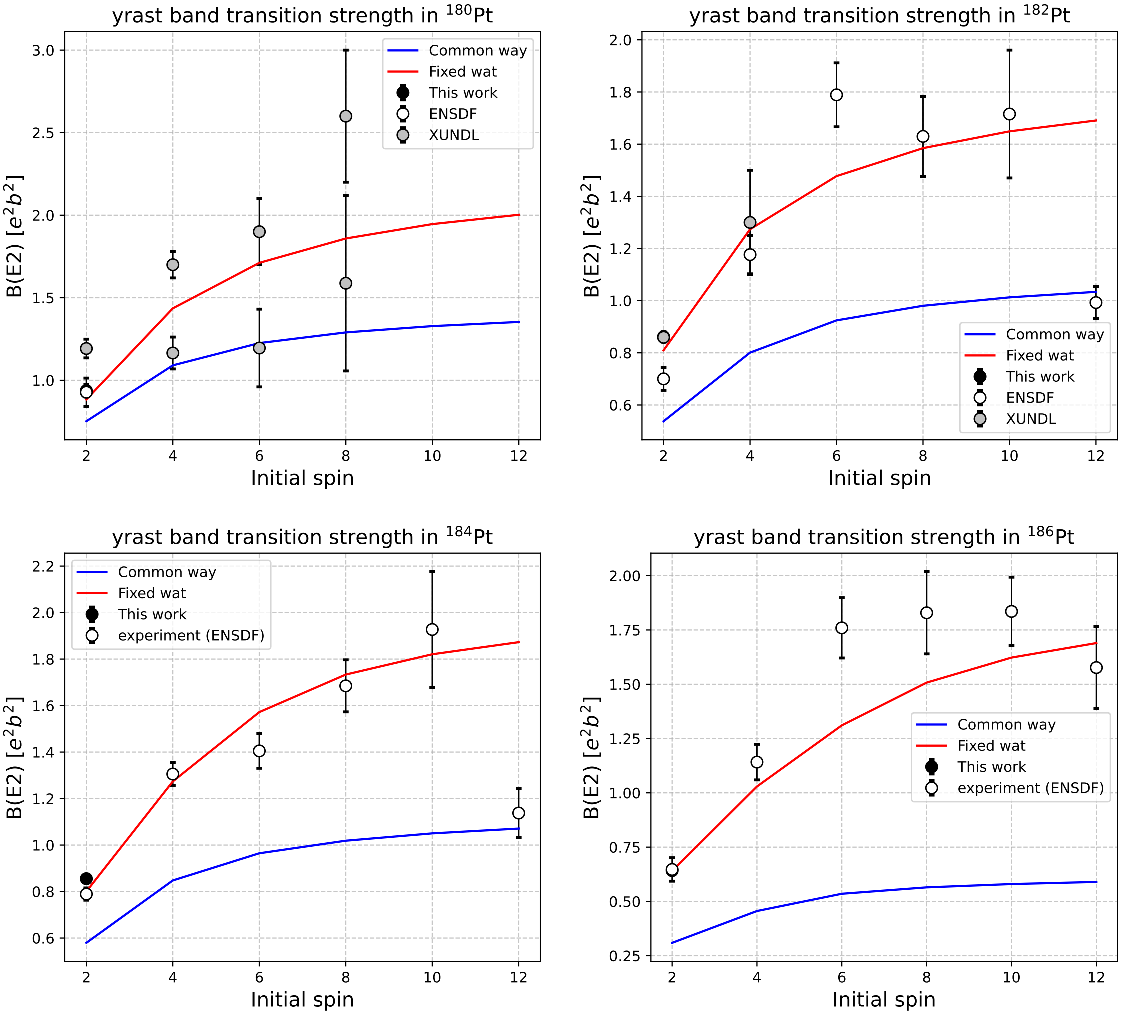

Figure 6.7: Experimental and calculated B(E2;I→I-2) values within the yrast states of $^{180-186}$Pt. Experimental data from previous studies (white/grey) [4–7, 9, 10, 74] and this work (black) are compared with calculations from the common way (blue line) and the fixed way (red line).

the present analysis shows relatively consistent results in the bandhead energies, $\mathfrak{I}_0$ and C of the d band and γ band, and inter-band interactions. Nevertheless, the values for $\mathfrak{I}_0$ and C of the g band appear reduced in this study. This is attributed to the updated energy measurements obtained subsequent to Ref. [40], which were lower than their calculated values, as discussed in Sec. 2.6.4.

Table 6.5: Fitted parameters for the fixed way three-band mixing model for $^{180-186}$Pt.

Parameters		^{180}Pt	^{182}Pt	^{184}Pt	^{186}Pt
g band	$\mathfrak{I}_0\,[\times 10^{-2}\,\mathrm{keV}^{-1}]$	0.56	0.13	0.94	0.99
	$C\,[\times 10^{6}\,\mathrm{keV}^{3}]$	2.06	1.11	6.76	3.76
	E_0 [keV]	296	347	281	150
d band	$\mathfrak{I}_0\,[\times 10^{-2}\,\mathrm{keV}^{-1}]$	2.95	2.51	2.64	2.42
	$C\,[\times 10^{6}\,\mathrm{keV}^{3}]$	3.05	2.13	1.77	1.71
	E_0 [keV]	182	150	210	310
γ band	$\mathfrak{I}_0\,[\times 10^{-2}\,\mathrm{keV}^{-1}]$	1.38^*	1.38^*	1.38^*	1.38^*
	$C\,[\times 10^{6}\,\mathrm{keV}^{3}]$	1.16^*	1.16^*	1.16^*	1.16^*
	E_0 [keV]	780	727	713	780
	V_{gd} [keV]	232	227	243	216
	$V_{g\gamma}$ [keV]	86	113	118	66
	$V_{d\gamma}$ [keV]	-5	-20	-20	-87

* Fixed at the values determined from the odd-spin members of the γ band in $^{180-184}$Pt as shown in Fig. 6.4.

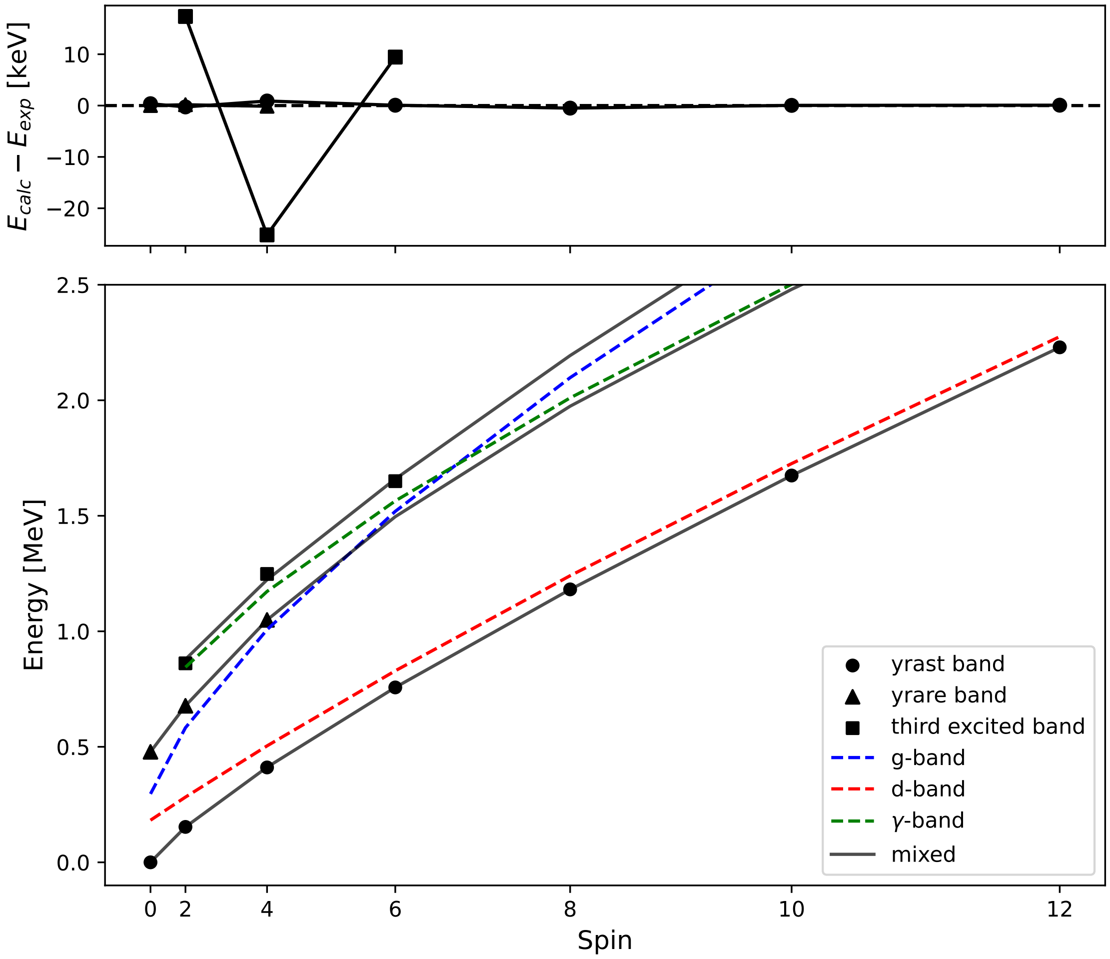

Figure 6.8: Comparison of experimental level energies (points) in ^{180}Pt with the results of the fixed way three-band-mixing model. The mixed band energies are shown as solid lines, while the unperturbed energies are represented by dashed lines.

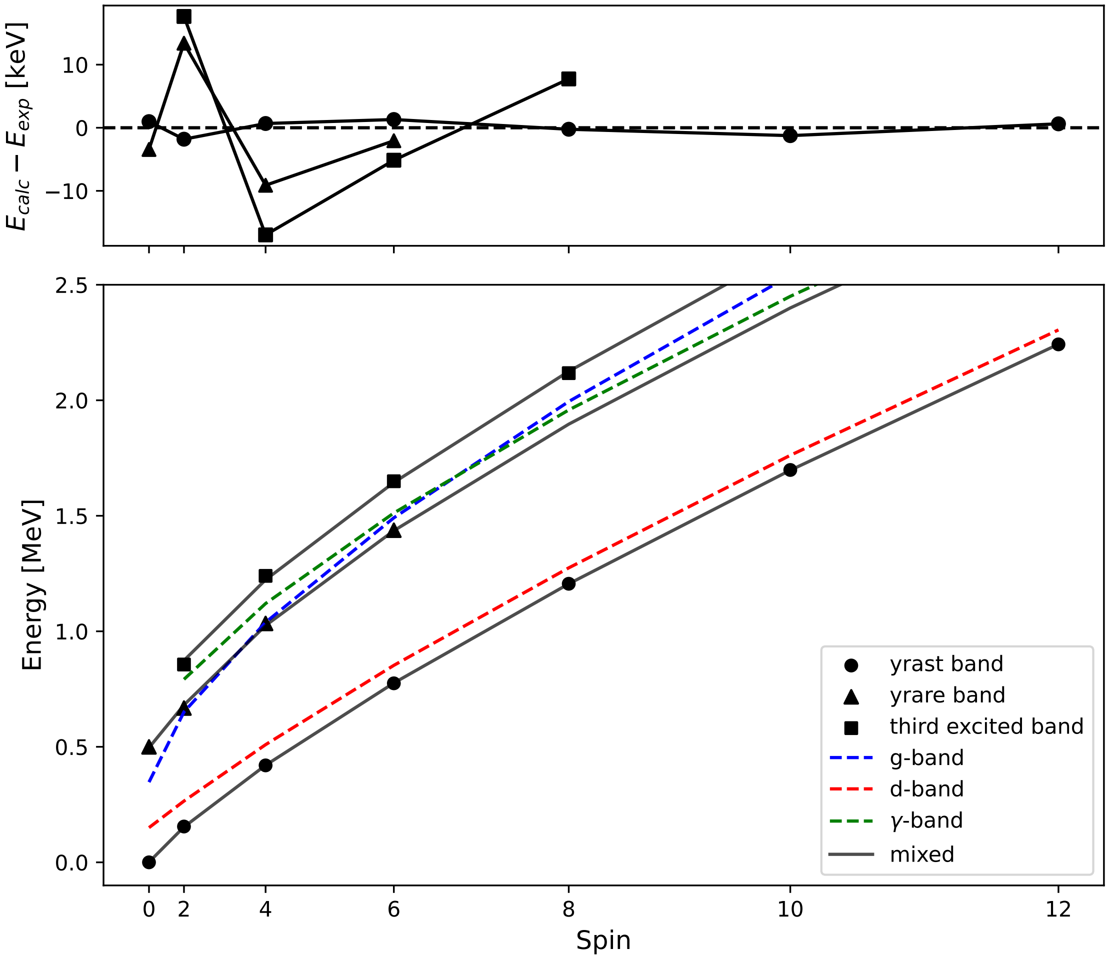

Figure 6.9: Comparison of experimental level energies (points) in ^{182}Pt with the results of the fixed way three-band mixing model. The mixed band energies are shown as solid lines, while the unperturbed energies are represented by dotted lines.

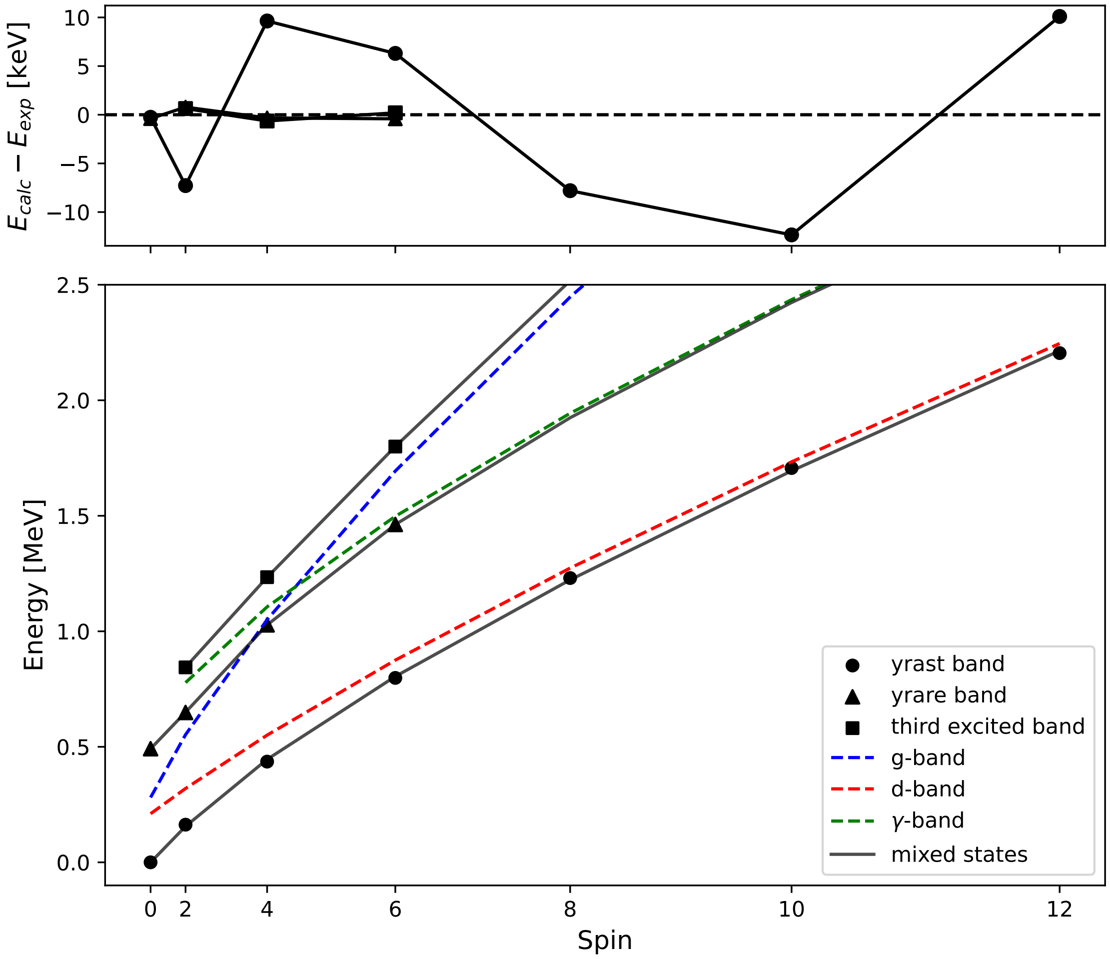

Figure 6.10: Comparison of experimental level energies (points) in ^{184}Pt with the results of the fixed way three-band mixing model. The mixed band energies are shown as solid lines, while the unperturbed energies are represented by dotted lines.

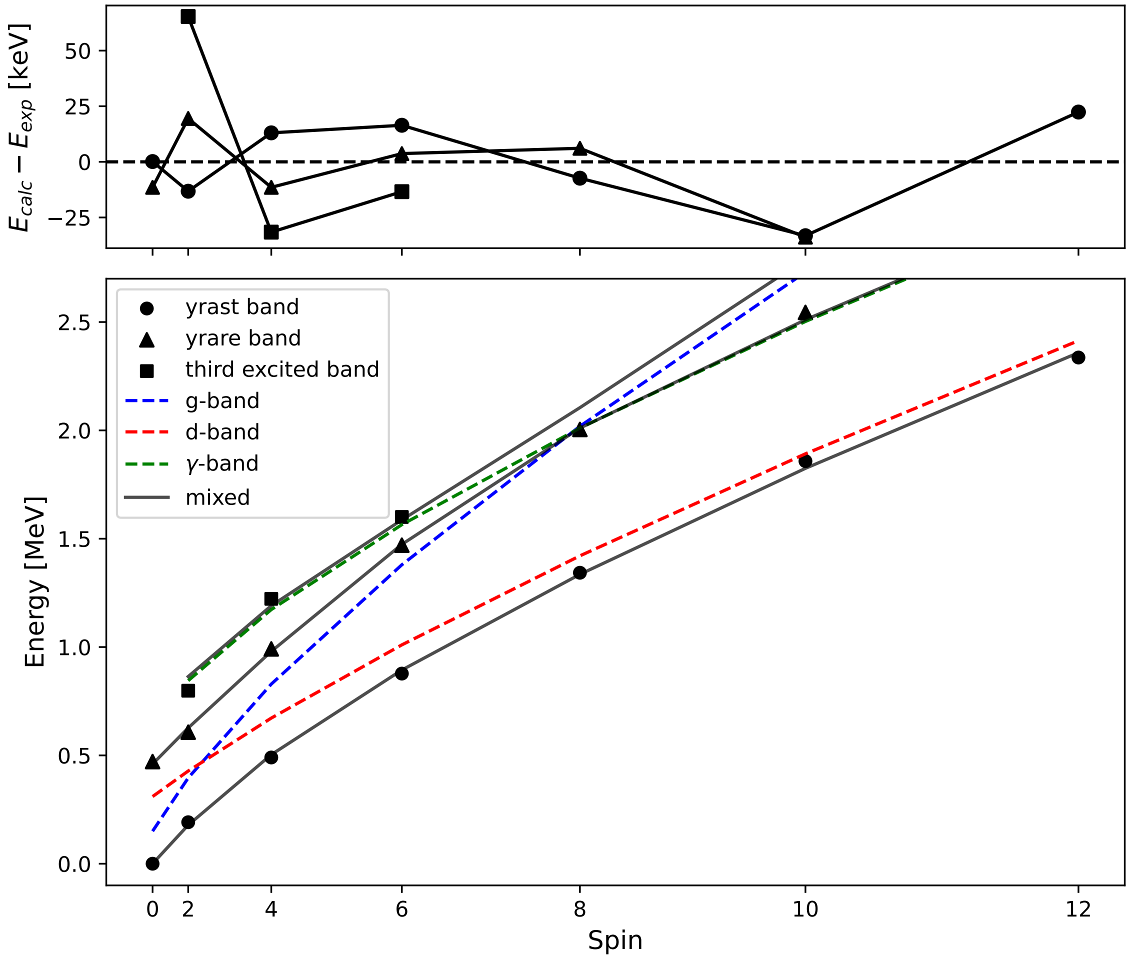

Figure 6.11: Comparison of experimental level energies (points) in ^{186}Pt with the results of the fixed way three-band mixing model. The mixed band energies are shown as solid lines, while the unperturbed energies are represented by dotted lines. Note that the y-axis range in the deviation plot (top panel) is significantly bigger than other isotopes.

Table 6.6: Results of the fixed way three-band mixing calculation for ^{180}Pt. Experimental energies are compared with the final calculated energies. The corresponding wavefunction amplitudes for the g band (A_g), d band (A_d), and γ band (A_γ) are also listed.

State	Observed Energy [keV]	Calculated Energy [keV]	Wavefunction Amplitudes A_g	A_d	A_{γ_d}
0^+	0	0	-0.617	0.787	0.000
	478	478	0.787	0.617	0.000
2^+	153	153	0.484	-0.872	-0.068
	677	678	-0.791	-0.470	0.392
	861	879	0.374	0.137	0.917
4^+	411	412	0.369	-0.928	-0.049
	1049	1049	-0.779	-0.337	0.528
	1248	1223	0.507	0.157	0.848
6^+	757	757	0.295	-0.955	-0.038
		1496	-0.615	-0.220	0.757
	1650	1659	-0.732	-0.200	-0.652
8^+	1181	1181	0.248	-0.968	-0.032
		1974	-0.390	-0.130	0.911
		2194	-0.887	-0.213	-0.410
10^+	1674	1674	0.217	-0.976	-0.029
		2480	-0.252	-0.085	0.964
		2805	-0.943	-0.201	-0.264
12^+	2229	2229	-0.194	0.981	0.028
		3019	-0.178	-0.063	0.982
		3474	0.965	0.186	0.186

Table 6.7: Results of the fixed way three-band mixing calculation for ^{182}Pt. Experimental energies are compared with the final calculated energies. The corresponding wavefunction amplitudes for the g band (A_g), d band (A_d), and γ band (A_γ) are also listed.

State	Observed Energy [keV]	Calculated Energy [keV]	Wavefunction Amplitudes A_g	A_d	A_{γ_d}
0^+	0	1	-0.549	0.836	0.000
	500	496	0.836	0.549	0.000
2^+	155	153	0.433	-0.896	-0.104
	668	681	-0.676	-0.399	0.619
	856	874	0.596	0.197	0.778
4^+	420	420	0.357	-0.930	-0.084
	1034	1025	-0.643	-0.310	0.700
	1240	1223	-0.677	-0.196	-0.709
6^+	775	776	0.313	-0.947	-0.074
	1438	1436	-0.572	-0.249	0.782
	1650	1644	-0.759	-0.202	-0.619
8^+	1206	1206	0.285	-0.956	-0.068
		1897	-0.494	-0.208	0.844
	2118	2125	-0.821	-0.207	-0.532
10^+	1698	1697	0.268	-0.961	-0.066
		2400	-0.425	-0.179	0.887
		2655	-0.864	-0.210	-0.457
12^+	2242	2243	0.257	-0.964	-0.065
		2940	-0.368	-0.160	0.916
		3226	-0.893	-0.212	-0.396

Table 6.8: Results of the fixed way three-band mixing calculation for ^{184}Pt. Experimental energies are compared with the final calculated energies. The corresponding wavefunction amplitudes for the g band (A_g), d band (A_d), and γ band (A_γ) are also listed.

State	Observed	Calculated	Wavefunction Amplitudes		
	Energy [keV]	Energy [keV]	A_g	A_d	A_{γ_d}
0^+	0	0	-0.654	0.756	0.000
	492	491	0.756	0.654	0.000
2^+	163	156	0.546	-0.828	-0.130
	649	650	-0.666	-0.523	0.532
	844	845	0.508	0.204	0.837
4^+	436	446	0.387	-0.917	-0.097
	1028	1028	-0.560	-0.317	0.765
	1234	1234	-0.732	-0.242	-0.637
6^+	798	805	0.272	-0.959	-0.074
	1463	1462	-0.309	-0.160	0.937
	1800	1800	-0.911	-0.232	-0.340
8^+	1231	1223	0.200	-0.978	-0.060
		1924	-0.177	-0.096	0.980
		2517	0.964	0.185	0.192
10^+	1707	1694	0.154	-0.987	-0.051
		2423	-0.116	-0.069	0.991
		3339	0.981	0.147	0.125
12^+	2204	2214	0.124	-0.991	-0.045
		2958	-0.083	-0.056	0.995
		4246	0.989	0.119	0.089

Table 6.9: Results of the fixed way three-band mixing calculation for ^{186}Pt. Experimental energies are compared with the final calculated energies. The corresponding wavefunction amplitudes for the g band (A_g), d band (A_d), and γ band (A_γ) are also listed.

State	Observed	Calculated	Wavefunction Amplitudes		
	Energy [keV]	Energy [keV]	A_g	A_d	A_{γ_d}
0^+	0	0	-0.821	0.571	0.000
	472	460	-0.571	-0.821	0.000
2^+	192	178	-0.719	0.677	0.160
	607	627	0.693	0.717	0.077
	798	864	0.062	-0.166	0.984
4^+	490	503	-0.567	0.808	0.161
	991	980	0.816	0.577	-0.019
	1222	1191	0.108	-0.121	0.987
6^+	878	894	-0.418	0.895	0.157
	1470	1474	0.872	0.444	-0.207
	1600	1587	0.255	-0.051	0.966
8^+	1343	1336	0.311	-0.938	-0.151
	2004	2010	-0.351	-0.261	0.899
		2105	-0.883	-0.226	-0.411
10^+	1858	1825	-0.239	0.960	0.147
	2545	2511	-0.118	-0.179	0.977
		2789	0.964	0.216	0.156
12^+	2336	2359	0.191	-0.971	-0.144
		3044	-0.067	-0.159	0.985
		3549	0.979	0.179	0.095

6.2.2 Calculated B(E2) transition strengths

This section compares B(E2) between experimental data and band-mixing calculations using the fixed approach for the γ band. Figure 6.12 and Tab. 6.10 present the B(E2; $2_1^+ \rightarrow 0_1^+$) transition strength, along with experimental values from Fig. 5.25. Overall, the calculations that considered both the prolate and oblate bands align well with the experimental trend, emphasising the existence of shape coexistence in this region.

The calculated absolute B(E2) amplitudes are proportional to the fitted parameter k^2, as detailed in Sec. 2.6.3. For this study, we adopted the value $k = 45$ [eb][keV$^{1/2}$] fitted from a previous study on W isotopes [39]. Once the lifetime value of ^{184}Pt is validated by future measurements, the parameter k can be fitted to the present results to enhance a comprehensive analysis of shape evolution in this platinum region. Therefore, this highlights that we should consider revisiting our result for ^{184}Pt.

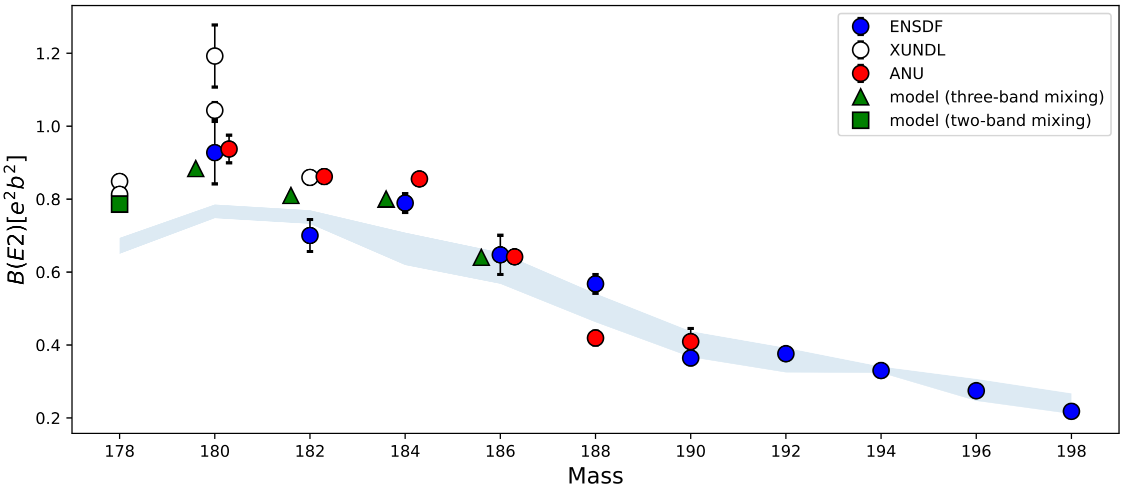

Figure 6.12: B(E2) transition strengths for the even-even platinum nuclei derived using the lifetime measurements from literature [4–10, 13–19], our previous measurements in $^{188-190}$Pt [11, 12], this study in $^{180-186}$Pt and the present fixed-way band-mixing calculations. The blue band shows deduced values from laser spectroscopy measurements of the ground-state charge radii [33, 69].

Table 6.10: Comparison of experimental B(E2; $2_1^+ \to 0_1^+$) transition strengths in $^{178-186}$Pt from this work and literature [4–10, 75, 76] with calculated values from the band-mixing models as described in the text.

Mass (A)	Calc. B(E2) gd [e^2b^2]	Calc. B(E2) Common [e^2b^2]	Calc. B(E2) Fixed [e^2b^2]	Expt. B(E2) [e^2b^2]
178	0.79			0.85(1)[a]
				0.81(4)[b]
180		0.75	0.88	0.94(4)[c]
				1.04(2)[d]
				1.19(6)[e]
				0.93(9)[g]
182		0.54	0.81	0.86(2)[c]
				0.86(2)[f]
				0.70(4)[g]
184		0.58	0.80	0.86(1)[c]
				0.79(3)[g]
186		0.31	0.64	0.64(1)[c]
				0.65(5)[g]

[a] C. B. Li *et al.* using the Convolution method [75].

[b] J. Heery *et al.* using the RDM method [76].

[c] This work using the GCD method.

[d] L. Barver *et al.* using the RDM method [8].

[e] Müller-Gatermann *et al.* using the Convolution method [9].

[f] Häfner, G *et al.* using the GCD method [10].

[g] ENSDF [4–7].

6.2.3 Calculated branching ratios

This section compares branching ratios between experimental data and band-mixing calculations using the fixed approach for the γ band. Tables 6.11-6.14 and Fig. 6.13 compare experimental and calculated branching ratios. Overall, the calculation can reproduce the experiments to certain levels, however, the experimental branching ratios were less accurately reproduced than B(E2; $2_1^+ \rightarrow 0_1^+$).

This discrepancy suggests two potential factors: either additional bands influence the higher spin states, or the B(E2) calculations are oversimplified due to the omission of off-diagonal elements (see Sec. 2.6.3). To enable a robust more-than-three-band-mixing calculation, these findings underscore the critical need for more extensive experimental data.

Furthermore, even though the RMSE for the ^{186}Pt branching ratios is relatively small, as shown in Tab. 6.4, the calculated values significantly underestimate the experimental data compared to the other isotopes in Fig. 6.13. As noted in the discussion of energy RMSE, this deviation is likely attributable to ^{186}Pt is located in the transitional region in the neutron-deficient even-mass platinum isotopes.

Table 6.11: Experimental branching ratios for ^{180}Pt from ENSDF [4] compared to the calculated values, assuming the same-sign case.

Initial state A	Final state B	γ-ray A → B	I_γ A → B	Final state C	γ-ray A → C	I_γ A → C	Expt. BR[a]	Calc. BR[b]
2_2^+	0_1^+	678	36(3)	2_1^+	524	100(2)	0.36(3)	0.49
	4_1^+	267	1.0(7)				0.01(7)	0.094
	0_2^+	199	1.7(14)				0.017(14)	0.051
2_3^+	0_1^+	861	100(7)	2_1^+	708	16(2)	6.25 (90)	1.29
	4_1^+	451	19.3(21)				1.21 (20)	1.21
	0_2^+	383	14(3)				0.88 (22)	2.71
	2_2^+	184	1.6(10)				0.10(6)	0.38
4_2^+	2_1^+	896	17(8)	4_1^+	639	100(13)	0.17(8)	1.20
	2_2^+	372	15(4)				0.15(5)	1.30
4_3^+	2_1^+	1095	100(21)	4_1^+	837	40(30)	2.5(19)	0.93
	2_3^+	387	90(40)				2.3(20)	2.04

[a] Expt. branching ratios $I_\gamma(A \rightarrow B)/I_\gamma(A \rightarrow C)$.

[b] Calc. branching ratios $B(E2; A \rightarrow B)E_\gamma^5(A \rightarrow B)/B(E2; A \rightarrow C)E_\gamma^5(A \rightarrow C)$.

Table 6.12: Experimental branching ratios for ^{182}Pt from ENSDF [5] compared to the calculated values, assuming the same-sign case

Initial state A	Final state B	γ-ray A → B	I_γ A → B	Final state C	γ-ray A → C	I_γ A → C	Expt. BR[a]	Calc. BR[b]
2^+_2	0^+_1	668	34(4)	2^+_1	513	100(11)	0.34(6)	0.73
2^+_3	0^+_1	856	100(3)	2^+_1	701	8.7(20)	11.5(3)	0.51
	4^+_1	437	22.7(20)				2.61(23)	2.24
	0^+_2	357	17(5)				1.95(58)	4.70
4^+_2	2^+_1	879	10(4)	4^+_1	615	100(6)	0.10(4)	2.50
	2^+_2	366	50(25)				0.50(25)	1.31
4^+_3	2^+_1	1085	100(7)	4^+_1	821	34(5)	2.94(48)	2.56
	2^+_2	573	41(12)				1.21(40)	0.49
	6^+_1	465	24(7)				0.71(23)	0.24
	2^+_3	383	66(12)				1.94(45)	1.50

[a] Expt. branching ratios $I_\gamma(A \to B)/I_\gamma(A \to C)$.

[b] Calc. branching ratios $B(E2; A \to B)E^5_\gamma(A \to B)/B(E2; A \to C)E^5_\gamma(A \to C)$.

Table 6.13: Experimental branching ratios for ^{184}Pt from ENSDF [6] compared to the calculated values, assuming the same-sign case

Initial state A	Final state B	γ-ray A → B	I_γ A → B	Final state C	γ-ray A → C	I_γ A → C	Expt. BR[a]	Calc. BR[b]
2_2^+	0_1^+	649	50(8)	2_1^+	486	100(10)	0.50(9)	0.67
	0_2^+	157	0.42(13)	2_1^+			0.004(1)	0.016
2_3^+	0_1^+	844	100(15)	2_1^+	681	13.1(20)	7.63(163)	0.82
	4_1^+	408	12.7(19)				0.97(21)	0.28
	0_2^+	352	12.0(18)				0.92(20)	0.10
	2_2^+	195	2.6(8)				0.20(7)	0.18
4_2^+	2_1^+	865	48(7)	4_1^+	592	100(14)	0.48(10)	0.21
	2_2^+	379	39(6)				0.39(8)	2.41
4_3^+	2_1^+	1071	100(14)	4_1^+	798	74(12)	1.35(29)	0.17
	2_2^+	586	18(6)				0.24(9)	4.53
	2_3^+	390	51(7)				0.69(15)	2.38
6_2^+	4_1^+	1027	69(10)	6_1^+	664	100(14)	0.69(14)	0.42
	4_2^+	435	90(14)				0.90(19)	14.2

[a] Expt. branching ratios $I_\gamma(A \rightarrow B)/I_\gamma(A \rightarrow C)$.

[b] Calc. branching ratios $B(E2; A \rightarrow B)E_\gamma^5(A \rightarrow B)/B(E2; A \rightarrow C)E_\gamma^5(A \rightarrow C)$.

Table 6.14: Experimental branching ratios for ^{186}Pt from ENSDF [7] compared to the calculated values, assuming the same-sign case

Initial state A	Final state B	γ-ray A → B	I_γ A → B	Final state C	γ-ray A → C	I_γ A → C	Expt. BR[a]	Calc. BR[b]
2_2^+	0_1^+	607	62(15)	2_1^+	416	100(8)	0.62(16)	0.10
2_3^+	0_1^+	799	8.6(10)	2_1^+	607	8.5(20)	1.01(27)	0.66
	4_1^+	308	0.66(5)				0.078(19)	0.005
	0_2^+	327	1.3(1)				0.153(38)	0.006
4_2^+	2_1^+	799	79(16)	4_1^+	501	100(16)	0.79(20)	0.09
	2_2^+	384	63(11)				0.63(15)	8.57
4_3^+	2_1^+	1031	100(5)	4_1^+	732	82(6)	1.22(11)	2.35
	4_2^+	732	82(6)				1.00(10)	0.028
	2_2^+	616	23(3)				0.28(4)	0.0004
	2_3^+	424	45(5)				0.55(7)	2.30
6_2^+	4_1^+	979	87(35)	6_1^+	592	100(47)	0.87(54)	0.004

[a] Expt. branching ratios $I_\gamma(A \to B)/I_\gamma(A \to C)$.

[b] Calc. branching ratios $B(E2; A \to B)E_\gamma^5(A \to B)/B(E2; A \to C)E_\gamma^5(A \to C)$.

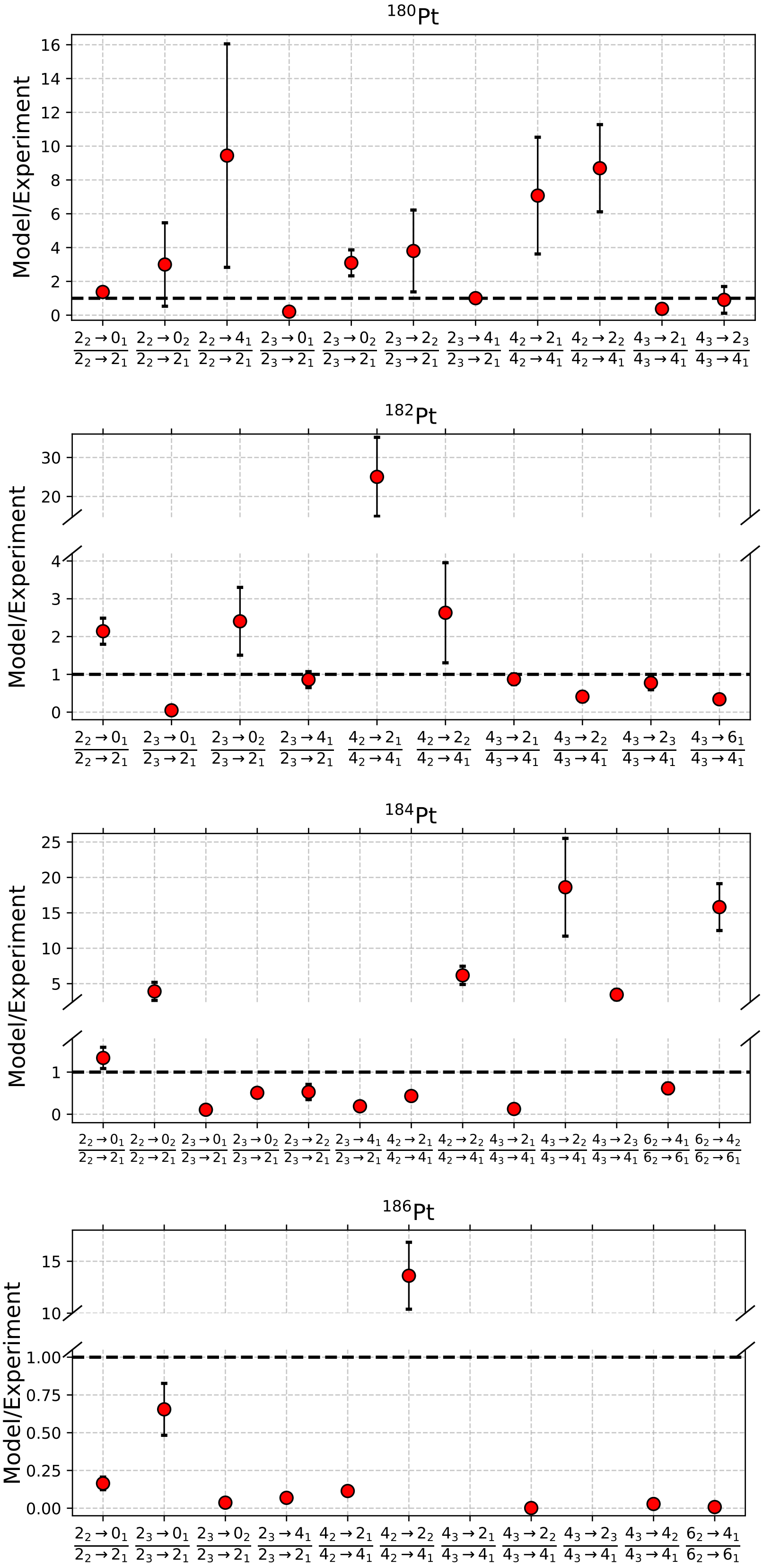

Figure 6.13: Ratios of calculated to experimental branching ratios in $^{180-186}$Pt, with the values taken from Tabs. 6.11-6.14.

Chapter 7

Passive shield design

To enhance our experimental setup for lifetime measurements, we have designed a new passive shielding system for the $\mathrm{LaBr_3}$ detectors. In the current setup, due to existing spatial constraints as depicted in Fig. 4.6, HPGe and $\mathrm{LaBr_3}$ detectors have to be swapped to be used with the Compton suppressors, depending on the purpose of the experiments. Preliminary work by an ANU undergraduate Summer Scholar student indicated that passive shielding can sufficiently suppress Compton scattering between $\mathrm{LaBr_3}$ detectors. Consequently, a well-designed passive absorber, considering the spatial limitations, can potentially enhance data quality significantly without the need for additional expensive active shields. This would enable nine HPGe detectors to be used with Compton suppressors, providing the opportunity to use HPGe-$\mathrm{LaBr_3}$-$\mathrm{LaBr_3}$ coincidences to obtain very clean, fast timing spectra. Moreover, the inclusion of more than six $\mathrm{LaBr_3}$ detectors may be considered to enhance the overall detection efficiency, and the six already available can be moved close to enhance their efficiency. The design of the passive shield and its feasibility were assessed using Geant4, a toolkit for simulating the passage of particles through matter.

7.1 Collimator investigation

A collimator on the $\mathrm{LaBr_3}$ detector is essential to prevent particles from striking the edges of the crystal, which would result in a distorted energy spectrum and increased Compton scattering. The impact of the collimator was initially examined using Geant4 under the simple condition shown in Fig. 7.1, whereby the incidence of a 1173-keV gamma ray near the edge of the $\mathrm{LaBr_3}$ crystal is analysed by altering the distance to the edge.

Figure 7.2 shows the normalised energy deposition spectrum within the $\mathrm{LaBr_3}$ crystal depending on the distance to the edge, demonstrating that as the distance increases, the events near zero become less pronounced and the full energy peak compared to the Compton scattered events improves. It is therefore suggested that a collimator coverage of not less than 3.5 mm, ideally 5.5 mm, be maintained. However, this recommendation should be balanced with considerations of efficiency and spatial constraints.

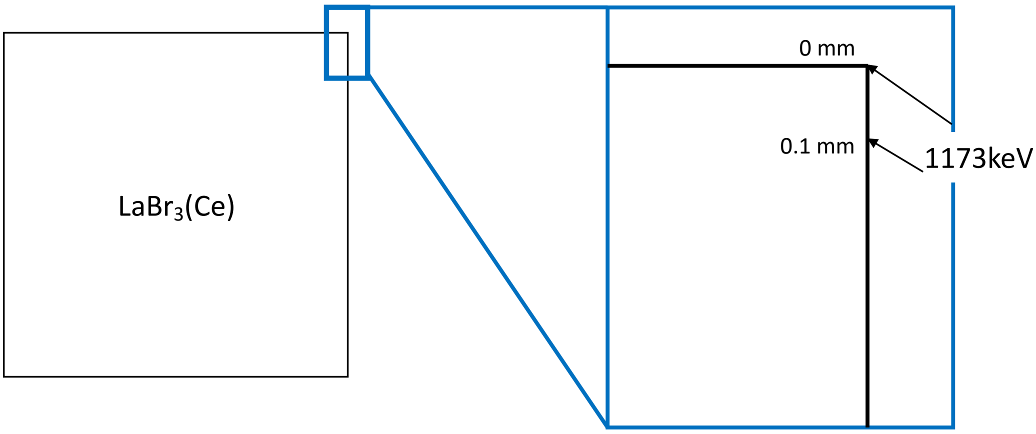

Figure 7.1: Conceptual diagram for a Geant4 simulation investigating the effect of a collimator on the energy spectrum. The figure shows an 1173-keV γ ray incident from the right-hand side near the edge of a LaBr$_3$ crystal, and the simulation was carried out by varying the distance from the edge.

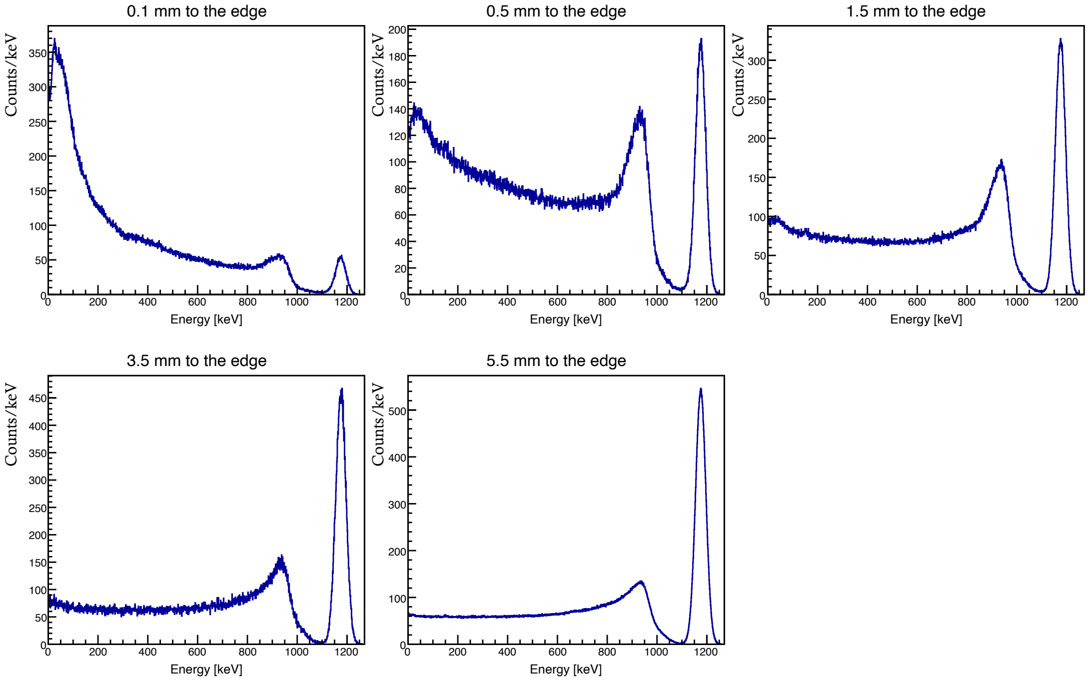

Figure 7.2: Normalised energy deposition spectra for an 1173-keV γ ray incident on a LaBr$_3$ crystal, depending on the distance from the crystal's edge.

7.2 Material determination

To determine whether lead or heavimet would be more suitable for the shielding, a Geant4 simulation was carried out with a ^{60}Co source under the simple conditions as depicted in Fig. 7.3 where two LaBr$_3$ detectors were placed within collimated shields to observe the effects of Compton scattering.

Figure 7.4 compares the resulting $\gamma-\gamma$ matrix projections after 500 million decay of a ^{60}Co source: no shield (left), Pb shield (middle) and heavimet shield (right). As expected, both shielded detectors effectively blocked Compton scattering events, which are apparent as two diagonal lines in the histogram with no shielding.

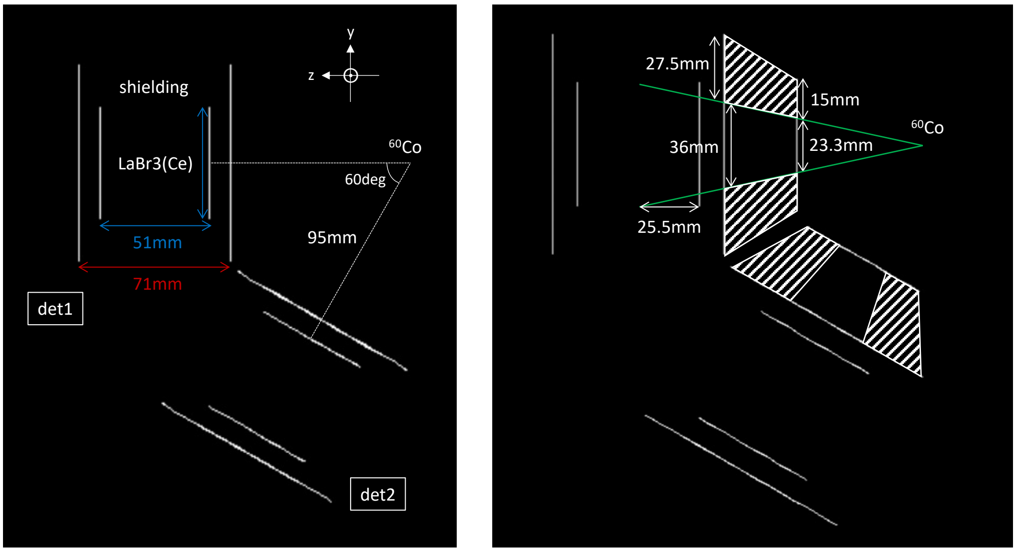

Figure 7.3: Geant4 simulation initial setup to determine the material to use. Two LaBr$_3$ detectors were placed within collimated shields. The Geant4 screenshot in the figure does not faithfully capture the true geometry, but the general arrangement is evident.

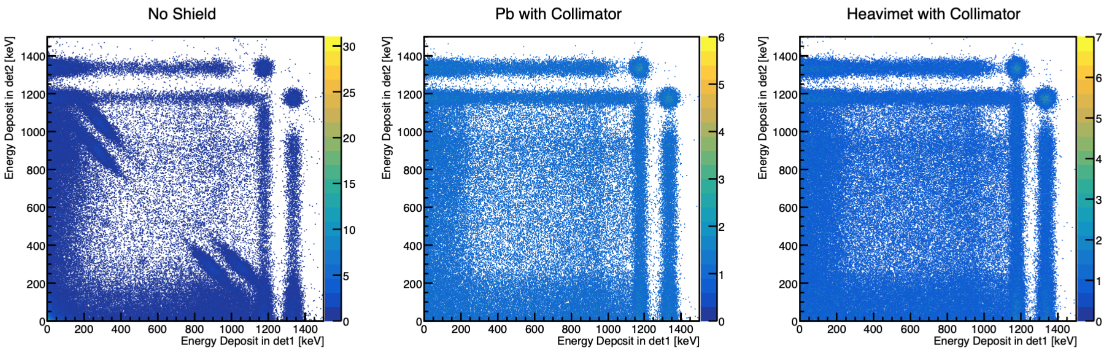

Figure 7.4: The figure illustrates the $\gamma-\gamma$ matrix projections after 500 million decay of a ^{60}Co source without shielding (left), with lead shielding (middle) and heavimet (right). Both shielded detectors effectively blocked Compton scattering, which are shown as two diagonal lines in the spectrum with no shielding.

Figure 7.5 compares peak-to-background ratios of the 1173-keV γ ray in spectra gated at 1332 keV within both lead and heavimet shielding. The peak-to-background ratios are calculated by the sum of counts in the blue regions divided by the red region. The values obtained were 0.37 and 0.39 for lead and heavimet, respectively. Although the performance of the heavimet shield slightly exceeded that of the lead shield due to its higher density of 18.5 g/cm^3 compared to 11.35 g/cm^3 for lead, the improvement between the two was minimal. Taking into account the cost limitations, lead was selected over heavimet.

7.3 Design overview

Following the material determination, the shields were designed by our technical staff member Thomas Tunningley, as illustrated in Fig. 7.8. At present, we have six $LaBr_3$ detectors, but the design aims to accommodate nine, anticipating future expansion.

7.3.1 Solid angle improvement

As depicted in Fig. 4.6 and conceptualised in Fig. 7.7, the solid angle per detector in the present configuration, where the $LaBr_3$ detectors are inserted laterally into

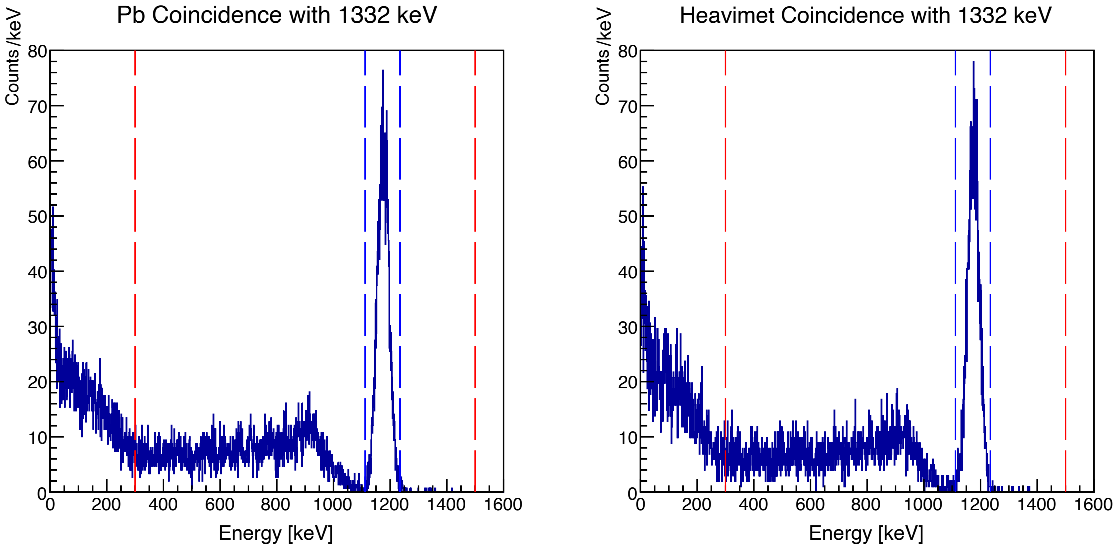

Figure 7.5: Comparison of the peak-to-background ratio for simulated gamma-ray spectra within lead and heavimet shielding, obtained by gating the coincidence matrix at 1332 keV. The calculated peak-to-background ratios for the coincident 1173 keV observed in the other detectors are calculated from the red peak region divided by the blue region, giving 0.37 for lead and 0.39 for heavimet.

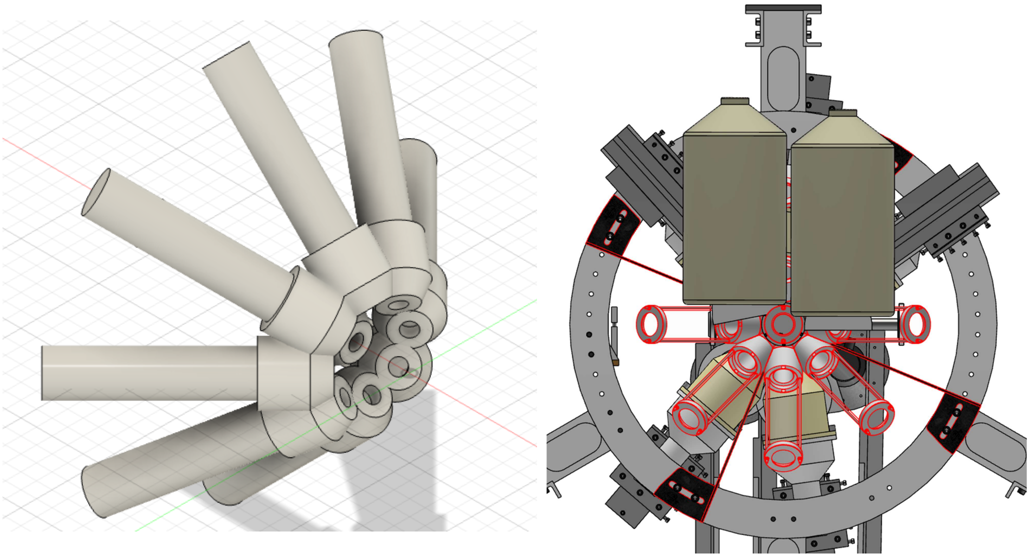

Figure 7.6: CAD view of the proposed shielding design as part of the CAESAR array, with basic parameters guided by the initial Geant4 simulation. It allows for nine detector positions, leaving three available for future development.

the Compton suppressors, can be calculated as follows:

$$
\begin{aligned}
\Omega &= \int_0^{2\pi} d\phi \int_0^{14.45/2 \text{ deg}} \sin\theta \, d\theta \\
&= 2\pi(1 - \cos 7.225 \text{ deg}) \sim 0.0158\pi \, [sr]
\end{aligned}
\tag{7.1}
$$

In contrast, Fig. 7.8 provides a detailed depiction of the concentric configuration of the proposed setup, and the solid angle can be calculated as follows:

$$
\begin{aligned}
\Omega &= \int_0^{2\pi} d\phi \int_0^{15.5/2 \text{ deg}} \sin\theta \, d\theta \\
&= 2\pi(1 - \cos 7.75 \text{ deg}) \sim 0.0183\pi \, [sr]
\end{aligned}
\tag{7.2}
$$

The solid angle is enhanced by about 1.16 times compared to the current configura-

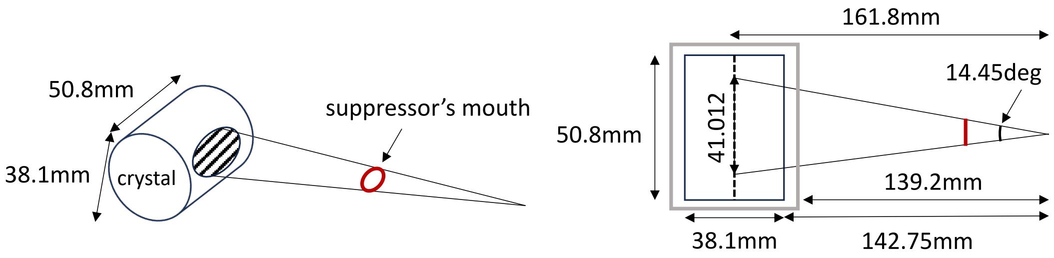

Figure 7.7: Conceptual diagram of the current CAESAR array's detector setup where the $LaBr_3$ detectors are positioned laterally within the suppressors.

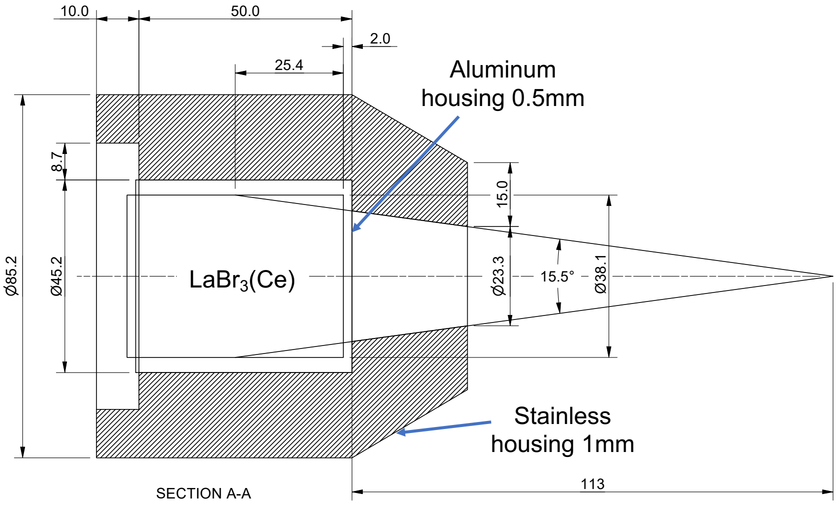

Figure 7.8: Detailed diagram of the proposed $\mathrm{LaBr_3}$ detector shielding configuration in the CAESAR array. Dimensions are in mm.

tion, while simultaneously meeting the requirements of the collimator illuminating a distance of at least ∼3.5 mm from the edge of the crystal, as discussed in Sec. 7.1.

7.3.2 Simulation results

A Geant4 simulation of the full proposed design was carried out using a ^{152}Eu source. In this simulation, the aluminium PMT tube was also modelled, considering its interior as a vacuum, as shown in Fig. 7.9. Figure 7.10 compares the $\gamma - \gamma$ matrix projection without a shield (left panel) and with a Pb shield (right panel). As expected, the shielded detectors significantly reduced Compton scattering, visible as multiple diagonal lines in the unshielded spectrum.

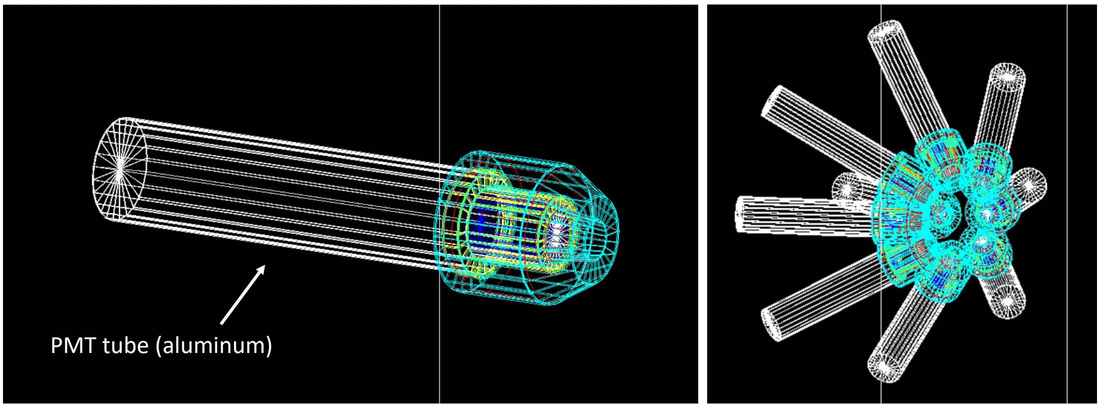

Figure 7.9: Geant4 simulation of the proposed shielding design. This figure shows the modelled setup, including the aluminium PMT tube with its inside treated as a vacuum.

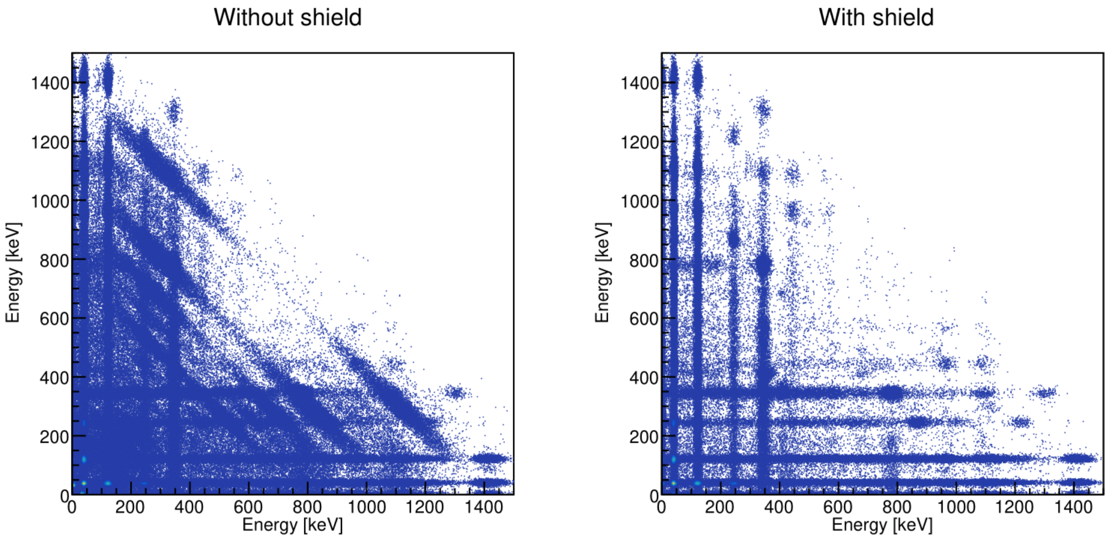

Figure 7.10: The plot on the left shows the simulated unshielded $\gamma - \gamma$ matrix for a ^{152}Eu source, while the plot on the right shows the matrix with the proposed Pb shield collimator design. These matrices are shown qualitatively to demonstrate the suppression of Compton-scattering anti-diagonal lines; therefore, no Z-scale is displayed. The reduction in Compton scattering is evident in the shielded spectrum, which has significantly fewer diagonal lines compared to the unshielded one.

Reducing x rays incident on the detectors is sometimes necessary. The proximity of a large mass of Pb near the crystal suggests that we should investigate whether 80-keV x rays from the Pb will impact the data. Reduction of x rays is usually achieved with a graded-Z absorber composed of materials with decreasing atomic numbers, such as lead-cadmium-copper, to absorb and re-emit lower energy x rays which are more easily shielded. The current design already incorporates aluminium and stainless steel housings for the LaBr$_3$ crystal and lead shielding, respectively, which may function as a graded-Z absorber, but this should be modelled, along with the potential requirement for additional shielding, such as copper.

Figure 7.11 presents the energy spectra simulated with the ^{152}Eu source across five conditions: without shielding (comprising only the crystal and its aluminium detector housing), with the inclusion of lead shielding both with and without stainless steel housing of the lead, and with an additional inner copper shielding of 1 mm and 3 mm thickness, respectively. Comparison of panels (A) and (B) in Fig. 7.11 shows a distinct presence of lead K x rays at ∼80 keV. These are subsequently attenuated by the stainless steel, as depicted in panel (C). While the addition of copper shielding further attenuates them, we have concluded that stainless steel is equally effective, thereby opting not to include an additional copper shield.

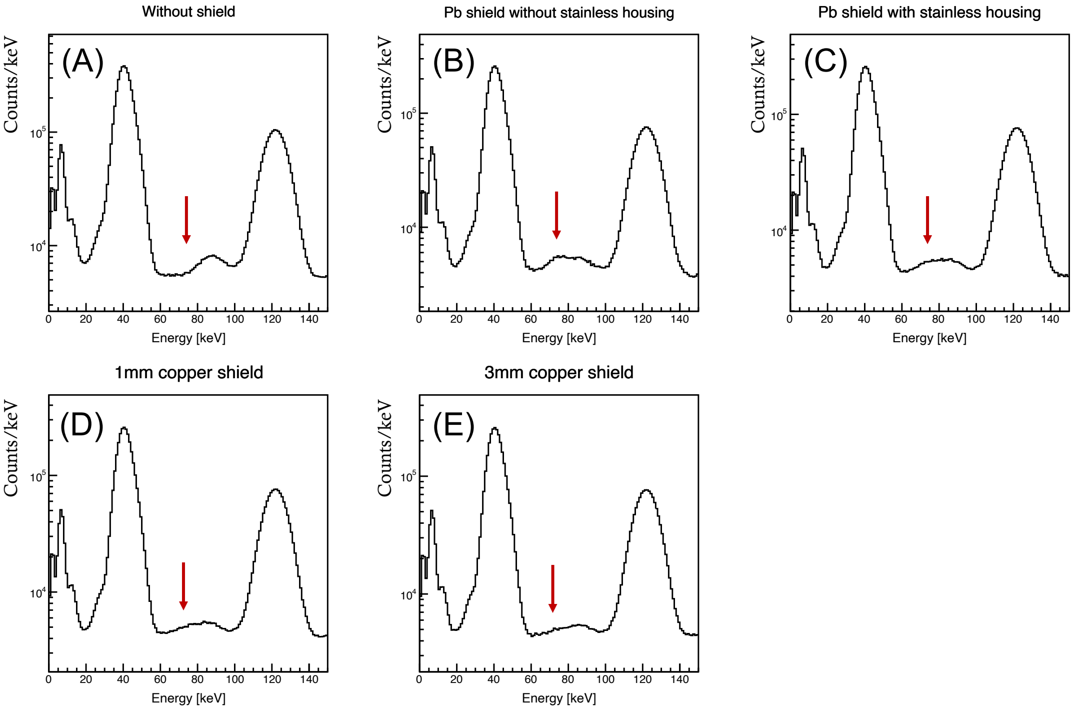

Figure 7.11: Single simulated energy spectra of different shielding configurations around the 122-keV γ rays from a ^{152}Eu source. The figure compares five conditions: (A) No shielding (crystal and its aluminium detector housing only); (B) With lead shielding and no stainless steel housing; (C) With lead and stainless steel housing of the lead; (D) With lead, stainless steel, and 1 mm copper shielding; (E) With lead, stainless steel, and 3 mm copper shielding.

7.4 Test experiment

The six $LaBr_3$ passive shields shown in Fig. 7.12 were tested in October 2025 along with six HPGe detectors using a ^{152}Eu source. Although the design allowed for eight Compton-suppressed HPGe detectors with the shielded $LaBr_3$ detectors, only six were used due to availability issues. This setup achieved ∼1.5 times better efficiency than the previous setup with the suppressors, which is ∼2.25 times higher coincidence efficiency. These results surpass the anticipated outcomes as calculated in Eqs. 7.1 and 7.2. This can be attributed to the geometry of the gamma-ray incidence on the $LaBr_3$ detectors. In the previous setup, the γ rays were incident on the side of the crystal cylinder due to the side-entry design of the Compton suppressors, whereas the new shielding design allows for face-on co-axial incidence, with an increase in effective detector efficiency.

Figure 7.13 presents the resulting gamma-gamma energy matrix of a ^{152}Eu source, and it is evident that Compton scattering between detectors is effectively eliminated. Additionally, the implementation of HPGe-$LaBr_3$-$LaBr_3$ gating was successfully achieved with this experimental setup, thereby enhancing the precision of

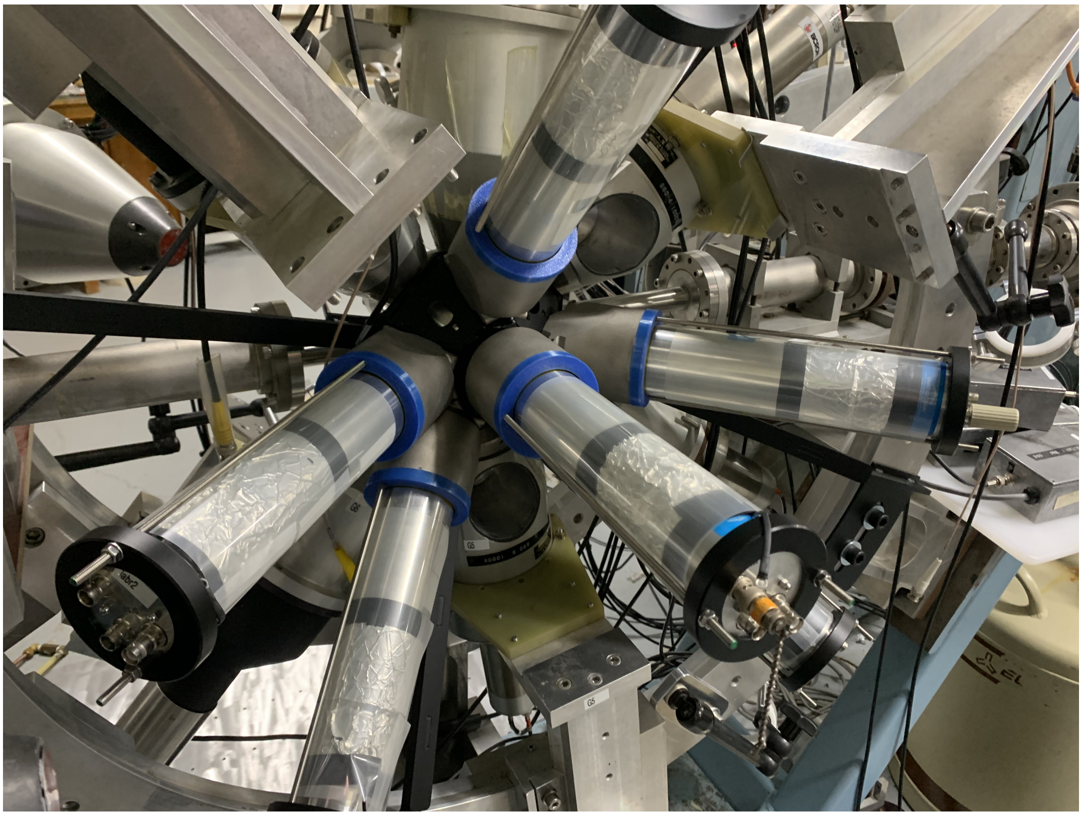

Figure 7.12: Six $LaBr_3$ detectors with the new passive shields in the CAESAR array.

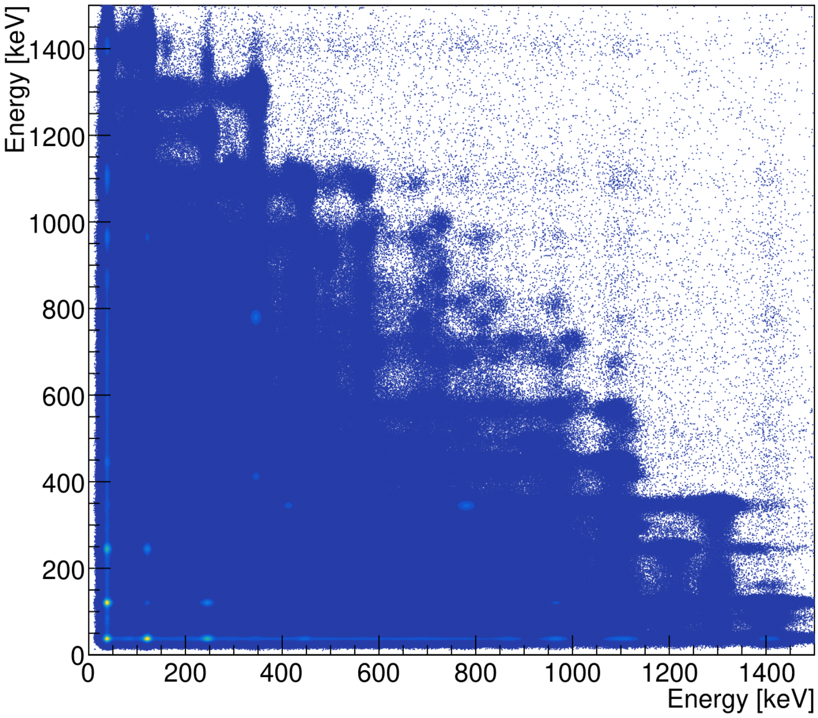

Figure 7.13: Gamma-gamma energy matrix of a ^{152}Eu source with the new $LaBr_3$ shields to be compared to the simulation in Fig. 7.3.2. The matrix is shown qualitatively to demonstrate the suppression of Compton-scattering anti-diagonal lines; therefore, no Z-scale is displayed. Diagonal lines that represent Compton scattering between detectors are eliminated.

lifetime measurements. In future work, we plan to measure the Pt lifetime values using this experimental setup to validate the present results.

Using this new setup, we also performed the same lifetime measurement for ^{184}Pt using the reaction described in Sec. 4. This result will be compared into the present result to confirm its lifetime. In addition, the 2_1^+ lifetime in ^{190}Pt was measured with this new setup, populated via the decay from ^{190}Au. This finding, along with the ^{188}Pt lifetime measured in October 2024 using the previous setup (populated via decay from ^{188}Au), will be compared against previous ANU measurements for ^{188,190}Pt [11, 12]. Future plans include the comprehensive analysis and comparison of all present results to significantly enhance the existing understanding of neutron-deficient, even-mass platinum isotopes.

Chapter 8

Conclusions

The lifetimes of the 2_1^+ states in the neutron-deficient even-even isotopes $^{180-186}$Pt have been measured using the γ-γ fast-timing technique with an array of LaBr$_3$(Ce) detectors in August and September 2023. The final lifetime values obtained via the GCD method were 533(26) ps, 561(14) ps, 479(6) ps and 350(4) ps for $^{180-186}$Pt, respectively. The new measurements for ^{180}Pt and ^{186}Pt were found to be consistent with the values reported in ENSDF [4, 7], and the ^{182}Pt result aligned with a more recent experimental measurement [10]. However, a discrepancy was observed for ^{184}Pt compared to the ENSDF data [6], suggesting the need for reinvestigation of this isotope.

To interpret the experimental lifetimes, empirical multi-band-mixing calculations were performed. The calculation of $B(E2)$ transition strengths includes a fitted parameter k that affects the absolute scale, for which the value obtained in a previous study on the W isotopes [39] was adopted. The calculations that incorporate shape coexistence of prolate and oblate shapes successfully reproduce the experimental $B(E2)$ systematics in $^{178–186}$Pt. This agreement decisively emphasised the presence of shape coexistence in this mid-shell region of platinum isotopes. A more comprehensive analysis of shape evolution would benefit from fitting the parameter k directly to the present experimental data, which first requires confirmation of the 2_1^+ lifetime in ^{184}Pt. However, the current calculations assume the same sign of the quadrupole moments for all bands to achieve satisfactory agreement. That contradicts the fact that the quadrupole moment should be positive for prolate and negative for oblate, and leaves open future investigations, including the possibility of triaxial shapes or addressing limitations of the simplified B(E2) calculations, such as ignoring the off-diagonal elements.

In addition to the lifetime investigations, a new passive shielding was successfully designed and tested for the LaBr$_3$ detectors in October 2025. This new setup effectively eliminates Compton scattering between detectors, and demonstrated an increase in coincidence efficiency by a factor of approximately 2.3 compared to the original setup. This advance will permit cleaner, higher-precision measurements, including the use of HPGe-$\mathrm{LaBr_3}$-$\mathrm{LaBr_3}$ coincidences to further validate the present results and explore new physics. A lifetime measurement of the ^{184}Pt 2_1^+ state has already been performed using this enhanced setup, and its detailed analysis will be a focus of future work.

Bibliography

[1] L. M. Robledo, R. Rodríguez-Guzmán, and P. Sarriguren. Role of triaxiality in the ground-state shape of neutron-rich Yb, Hf, W, Os and Pt isotopes. *Journal of Physics G: Nuclear and Particle Physics*, 36(11):115104, sep 2009.

[2] K. Heyde and J.L. Wood. Shape coexistence in atomic nuclei. *Rev. Mod. Phys.*, 83:1467–1521, Nov 2011.

[3] J.E. García-Ramos, V. Hellemans, and K. Heyde. Platinum nuclei: Concealed configuration mixing and shape coexistence. *Phys. Rev. C*, 84:014331, Jul 2011.

[4] E.A. McCutchan. Nuclear Data Sheets for A=180. *Nuclear Data Sheets*, 126:151–372, 2015.

[5] B. Singh. Nuclear Data Sheets for A=182. *Nuclear Data Sheets*, 130:21–126, 2015.

[6] M.J. Martin and P.H. Stelson. Nuclear Data Sheets for A=184. *Nuclear Data Sheets*, 21(1):1–89, 1977.

[7] J.C. Batchelder, A.M. Hurst, and M.S. Basunia. Nuclear Data Sheets for A=186. *Nuclear Data Sheets*, 183:1–346, 2022.

[8] L. Barber et al. A charge plunger device to measure the lifetimes of excited nuclear states where transitions are dominated by internal conversion. *Nuclear Instruments and Methods in Physics Research Section A: Accelerators, Spectrometers, Detectors and Associated Equipment*, 979:164454, 2020.

[9] C. Müller-Gatermann et al. Low-lying electromagnetic transition strengths in ^{180}Pt. *Phys. Rev. C*, 97:024336, Feb 2018.

[10] G. Häfner et al. Lifetime measurements in ^{182}Pt using γ–γ fast-timing. *The European Physical Journal A*, 57, 05 2021.

[11] H. A. Alshammari. *Fast timing measurements as a probe of nuclear shapes in ^{188}Pt and ^{190}Pt.* PhD thesis, The Australian National University, Nov 2024.

[12] H. A. Alshammari *et al.* Lifetimes of the first 2^+ states in ^{188}Pt and ^{190}Pt and the shape transition in theplatinum isotopes. Phys. Rev. C (submitted, 2024), 2024.

[13] E. Achterberg, O.A. Capurro, and G.V. Marti. Nuclear Data Sheets for A=178. *Nuclear Data Sheets*, 110(7):1473–1688, 2009.

[14] F.G. Kondev, S. Juutinen, and D.J. Hartley. Nuclear Data Sheets for A=188. *Nuclear Data Sheets*, 150:1–364, 2018.

[15] B. Singh and J. Chen. Nuclear Data Sheets for A=190. *Nuclear Data Sheets*, 169:1–390, 2020.

[16] C.M. Baglin. Nuclear Data Sheets for A = 192. *Nuclear Data Sheets*, 113(8):1871–2111, 2012.

[17] J. Chen and B. Singh. Nuclear Data Sheets for A=194. *Nuclear Data Sheets*, 177:1–508, 2021.

[18] H. Xiaolong. Nuclear Data Sheets for A = 196. *Nuclear Data Sheets*, 108(6):1093–1286, 2007.

[19] X. Huang and M. Kang. Nuclear Data Sheets for A = 198. *Nuclear Data Sheets*, 133:221–416, 2016.

[20] L. Grodzins. The uniform behaviour of electric quadrupole transition probabilities from first 2^+ states in even-even nuclei. *Physics Letters*, 2(2):88–91, 1962.

[21] R.V. Jolos and E.A. Kolganova. Derivation of the Grodzins relation in collective nuclear model. *Physics Letters B*, 820:136581, 2021.

[22] S. Raman, C.W. Nestor, and K.H. Bhatt. Systematics of B(E2; $0_1^+ \rightarrow 2_1^+$) values for even-even nuclei. *Phys. Rev. C*, 37:805–822, Feb 1988.

[23] K.S. Krane. *Introductory Nuclear Physic.* Wiley, New York, oct 1987.

[24] J. Suhonen. *From Nucleons to Nucleus.* Springer Berlin, Heidelberg, apr 2007.

[25] S. Raman, C.H. Malarkey, W.T. Milner, C.W. Nestor, and P.H. Stelson. Transition probability, B(E2)↑, from the ground to the first-excited 2^+ state of even-even nuclides. *Atomic Data and Nuclear Data Tables*, 36(1):1–96, 1987.

[26] A.N. Bohr and B.R. Mottelson. Collective and individual-particle aspects of nuclear structure. Technical Report 16, 1953. This document exists only as a journal publication: it is not in the CERN Official Collection bound volume.

[27] R.F. Casten. *Nuclear Structure from a Simple Perspective.* Oxford Studies in Nuclear Physics. Oxford University Press, London, England, mar 2001.

[28] H. Morinaga. Interpretation of Some of the Excited States of $4n$ Self-Conjugate Nuclei. *Phys. Rev.*, 101:254–258, Jan 1956.

[29] L.P. Gaffney et al. Shape coexistence in neutron-deficient Hg isotopes studied via lifetime measurements in ^{184,186}Hg and two-state mixing calculations. *Phys. Rev. C*, 89:024307, Feb 2014.

[30] K. Heyde. A shell-model description of intruder states and shape. *Nucl. Phys. A*, 507:149c–154, 1990.

[31] P. Koldewijn. *Mixing between gamma-, and beta- and groundstate bands in even deformed nuclei; a phenomenological approach.* Ph.D. thesis, Amsterdam University, 1977.

[32] P.M Davidson. *Non-yrast states and shape coexistence in light Os and Pt isotopes.* PhD thesis, The Australian National University, 1994.

[33] M.A.J. Mariscotti, G. Scharff-Goldhaber, and B. Buck. Phenomenological analysis of ground-state bands in even-even nuclei. *Phys. Rev.*, 178:1864–1886, Feb 1969.

[34] G.D. Dracoulis, A.E. Stuchbery, A.P. Byrne, A.R. Poletti, S.J. Poletti, J. Gerl, and R.A. Bark. Shape coexistence in very neutron-deficient Pt isotopes. *Journal of Physics G: Nuclear Physics*, 12(3):L97, mar 1986.

[35] G.D. Dracoulis. Properties of intruder bands in the $\mathrm{Os}-\mathrm{Pt}-\mathrm{Hg}-\mathrm{Pb}$ region. *Phys. Rev. C*, 49:3324–3327, Jun 1994.

[36] S. Anderssen. *Magnetic moment measurements in unstable platinum nuclei.* PhD thesis, The Australian National University, 1995.

[37] M.P. Robinson. *Perturbed $\gamma-\gamma$ correlations from oriented nuclei and moment measurements in neutron-deficient platinum nuclei.* PhD thesis, The Australian National University, 2001.

[38] N. Bree et al. Shape coexistence in the neutron-deficient even-even $^{182-188}$Hg isotopes studied via coulomb excitation. *Phys. Rev. Lett.*, 112:162701, Apr 2014.

[39] G.D. Dracoulis, R.A. Bark, A.E. Stuchbery, A.P. Byrne, A.M. Baxter, and F. Riess. Band crossings in ^{170}Os. *Nuclear Physics A*, 486(2):414–428, 1988.

[40] P.M Davidson, G.D Dracoulis, T Kibédi, A.P Byrne, S.S Anderssen, A.M Baxter, B Fabricius, G.J Lane, and A.E Stuchbery. Non-yrast states and shape co-existence in light Pt isotopes. *Nuclear Physics A*, 657(3):219–250, 1999.

[41] G.J. Lane. *Coexistence and Structure of Deformed Shapes Near the Z=82 Closed Shell.* PhD thesis, The Australian National University, 1995.

[42] M. Guttormsen. B(E2) ratios in the shape coexistent ^{184,186,188}Hg isotopes. *Physics Letters B*, 105(2):99–102, 1981.

[43] F.G. Kondev et al. High-spin collective structures in ^{178}Pt. *Phys. Rev. C*, 61:044323, Mar 2000.

[44] M.J.A. De Voigt, R. Kaczarowski, H.J. Riezebos, R.F. Noorman, J.C. Bacelar, M.A. Deleplanque, R.M. Diamond, F.S. Stephens, J. Sauvage, and B. Roussière. Collective and quasiparticle excitations in ^{180}Pt. *Nuclear Physics A*, 507(2):472–496, 1990.

[45] D. G. Popescu et al. High-spin states and band structures in ^{182}Pt. *Phys. Rev. C*, 55:1175–1191, Mar 1997.

[46] M.P. Carpenter et al. Alignment processes and shape variations in ^{184}Pt. *Nuclear Physics A*, 513(1):125–173, 1990.

[47] G. Hebbinghaus, T. Kutsarova, W. Cast, A. Krämer-Flecken, R.M. Lieder, and W. Urban. Study of band structures in the γ-unstable nucleus ^{186}Pt. *Nuclear Physics A*, 514(2):225–251, 1990.

[48] R. Krücken. Precision lifetime measurements using the recoil distance method. *J Res Natl Inst Stand Technol*, 105(1):53–61, February 2000.

[49] A. Dewald, O. Möller, and P. Petkov. Developing the Recoil Distance Doppler-Shift technique towards a versatile tool for lifetime measurements of excited nuclear states. *Progress in Particle and Nuclear Physics*, 67(3):786–839, 2012.

[50] J.M. Régis, L.M. Fraile, and M. Rudigier. γ–γ fast timing with high-performance $LaBr_3$(Ce) scintillators. *Progress in Particle and Nuclear Physics*, 141:104152, 2025.

[51] J.M. Régis, M. Rudigier, J. Jolie, A. Blazhev, C. Fransen, G. Pascovici, and N. Warr. The time-walk of analog constant fraction discriminators using very fast scintillator detectors with linear and non-linear energy response. *Nuclear Instruments and Methods in Physics Research Section A: Accelerators, Spectrometers, Detectors and Associated Equipment*, 684:36–45, 2012.

[52] J.M. Régis. *Fast timing with $LaBr_3$(Ce) scintillators and the mirror symmetric centroid difference method.* PhD thesis, University of Cologne, Jun 2011.

[53] E.R. Gamba, A.M. Bruce, and M. Rudigier. Treatment of background in $\gamma - \gamma$ fast-timing measurements. *Nuclear Instruments and Methods in Physics Research Section A: Accelerators, Spectrometers, Detectors and Associated Equipment*, 928:93–103, 2019.

[54] N. Peter. ANU undergraduate research report (unpublished), 2021.

[55] J. Newton. *Nuclear spectroscopy and reactions, Part C.* Academic Press, 1974.

[56] D. Pelte and D. Schwalm. *Heavy ion collision*, volume 3. North-Holland Publishing Company, 1982.

[57] A. Gavron. Statistical model calculations in heavy ion reactions. *Phys. Rev. C*, 21:230–236, Jan 1980.

[58] W.M. Higgins, A. Churilov, E. van Loef, J. Glodo, M. Squillante, and K. Shah. Crystal growth of large diameter $LaBr_3$:Ce and $CeBr_3$. *Journal of Crystal Growth*, 310(7):2085–2089, 2008. the Proceedings of the 15th International Conference on Crystal Growth (ICCG-15) in conjunction with the International Conference on Vapor Growth and Epitaxy and the US Biennial Workshop on Organometallic Vapor Phase Epitaxy.

[59] Saint-Gobain Crystals. *Technical drawing of SCINTIBLOC 38 S 51/2/B380 $LaBr_3$(Ce) detector*, 2013. Drawing No. 2-4-7933.

[60] W.R. Leo. *Techniques for Nuclear and Particle Physics Experiments: A How-to Approach.* Springer, 1994.

[61] A.P. Byrne and G.D. Dracoulis. Monte Carlo calculations for asymmetric NaI(Tl) and BGO compton suppression shields. *Nuclear Instruments and Methods in Physics Research Section A: Accelerators, Spectrometers, Detectors and Associated Equipment*, 234(2):281–287, 1985.

[62] L. Hildingsson, C.W. Beausang, D.B. Fossan, W.F. Piel, A.P. Byrne, and G.D. Dracoulis. Transverse BGO Compton suppression shield. *Nuclear Instruments and Methods in Physics Research Section A: Accelerators, Spectrometers, Detectors and Associated Equipment*, 252(1):91–94, 1986.

[63] Xia LLC. *Pixie-16 User Manual*, Sep 2019.

[64] V.T. Jordanov, G.F. Knoll, A.C. Huber, and J.A. Pantazis. Digital techniques for real-time pulse shaping in radiation measurements. *Nuclear Instruments and Methods in Physics Research Section A: Accelerators, Spectrometers, Detectors and Associated Equipment*, 353(1):261–264, 1994.

[65] V. Radeka. Trapezoidal filtering of signals from large germanium detectors at high rates. *Nuclear Instruments and Methods*, 99(3):525–539, 1972.

[66] H. Tan, M. Momayezi, A. Fallu-Labruyere, Y. Chu, and W.K. Warburton. A fast digital filter algorithm for gamma-ray spectroscopy of double-exponential decaying scintillators. In *2003 IEEE Nuclear Science Symposium. Conference Record (IEEE Cat. No.03CH37515)*, volume 2, pages 784–788 Vol.2, 2003.

[67] M. Gerathy. *Investigating nuclear structure through gamma-ray and electron spectroscopy with Solenogam*. PhD thesis, The Australian National University, 2020.

[68] M.J. Martin. Nuclear Data Sheets for A = 152. *Nuclear Data Sheets*, 114(11):1497–1847, 2013.

[69] Th. Hilberath, St. Becker, G. Bollen, H.-J. Kluge, U. Krönert, G. Passler, J. Rikovska, R. Wyss, and the ISOLDE Collaboration. Ground-state properties of neutron-deficient platinum isotopes. *Zeitschrift für Physik A Hadrons and Nuclei*, 342(1):1–15, Mar 1992.

[70] F. Le Blanc et al. Large odd-even radius staggering in the very light platinum isotopes from laser spectroscopy. *Phys. Rev. C*, 60:054310, Oct 1999.

[71] G. Ulm, S. K. Bhattacherjee, P. Dabkiewicz, G. Huber, H.-J. Kluge, T. Kühl, H. Lochmann, E.-W. Otten, K. Wendt, S. A. Ahmad, W. Klempt, R. Neugart, and ISOLDE Collaboration. Isotope shift of ^{182}Hg and an update of nuclear

moments and charge radii in the isotope range ^{181}Hg-^{206}Hg. *Zeitschrift für Physik A Atomic Nuclei*, 325(3):247–259, Sep 1986.

[72] S. Raman, C.W. Nestor, and P. Tikkanen. Transition Probability From the Ground to the First-excited 2^+ State of Even–even Nuclide. *Atomic Data and Nuclear Data Tables*, 78(1):1–128, 2001.

[73] F.G. Kondev and S. Lalkovski. Nuclear Data Sheets for A = 200. *Nuclear Data Sheets*, 108(7):1471–1582, 2007.

[74] Q. M. Chen et al. Lifetime measurements in ^{180}Pt. *Phys. Rev. C*, 93:044310, Apr 2016.

[75] C.B. Li et al. Lifetime measurement of the first 2^+ state in ^{178}Pt. *Phys. Rev. C*, 90:047302, Oct 2014.

[76] J. Heery et al. Lifetime measurements of yrast states in ^{178}Pt using the charge plunger method with a recoil separator. *The European Physical Journal A*, 57(4):132, Apr 2021.